박 사 학 위 논 문

Ph.D. Dissertation

부유식 평판 구조물에 대한 유탄소성 해석

Hydro-elastoplastic analysis of floating plate structures

2017

윤 주 성 (尹 柱 盛 Yoon, Joo-Seong)

한 국 과 학 기 술 원

Korea Advanced Institute of Science and Technology

박 사 학 위 논 문

부유식 평판 구조물에 대한 유탄소성 해석

2017

윤 주 성

한 국 과 학 기 술 원

기계항공공학부/기계공학과

부유식 평판 구조물에 대한 유탄소성 해석

윤 주 성

위 논문은 한국과학기술원 박사학위논문으로
학위논문 심사위원회의 심사를 통과하였음

2016년 11월 14일

심사위원장 이 필 승 (인)

심 사 위 원 김 진 환 (인)

심 사 위 원 정 형 조 (인)

심 사 위 원 김 병 완 (인)

심 사 위 원 김 대 겸 (인)

Hydro-elastoplastic analysis of floating structures

Joo-Seong Yoon

Advisor: Phill-Seung Lee

A dissertation submitted to the faculty of
Korea Advanced Institute of Science and Technology in
partial fulfillment of the requirements for the degree of
Doctor of Philosophy in Mechanical Engineering

Daejeon, Korea
November 14, 2016

Approved by

Phill-Seung Lee
Professor of Mechanical Engineering

The study was conducted in accordance with Code of Research Ethics[1].

1) Declaration of Ethical Conduct in Research: I, as a graduate student of Korea Advanced Institute of Science and Technology, hereby declare that I have not committed any act that may damage the credibility of my research. This includes, but is not limited to, falsification, thesis written by someone else, distortion of research findings, and plagiarism. I confirm that my dissertation contains honest conclusions based on my own careful research under the guidance of my advisor.

DME 20117038

윤주성. 부유식 평판 구조물에 대한 유탄소성 해석. 기계공학. 2017년. 137+viii 쪽. 지도교수: 이필승. (영문 논문)
Yoon, Joo-Seong. Hydro-elastoplastic analysis of floating plate structures. Department of Mechanical Engineering. 2017. 137+viii pp. Advisor: Lee, Phill-Seung. (Text in English)

초록
해상 항공, 폰툰 타입의 해양 플랜트나 교량 등과 같은 부유식 구조물 설계 시 해양 파랑과 구조체의 상호 작용을 반드시 고려해야 한다. 본 논문에서는 파랑 및 충격 하중에 의한 평판형 부유식 구조물의 탄소성 거동과 구조물 주변 유체 유동의 상호 작용에 관해 연구 하였다. 구조물의 비선형 동적 거동 묘사를 위한 증분 평형 방정식과 선형 표면 중력파에 의한 유체력 산정을 위한 임펄스 응답 함수와 중첩 적분을 연성시킨 유탄소성 해석 기법을 고안하였다. 부유식 평판 구조물의 선형 및 비선형 문제들에 대해 기존의 수치 및 실험 결과와 비교함으로써 제안한 유탄소성 해석 기법의 유효성과 성능을 검증하였다.

핵 심 낱 말 유탄소성 해석, 부유식 평판 구조물. 초대형 부유식 구조물, 임펄스 응답 함수, 비선형 구조 해석, 유한요소법, 경계요소법, 직접연성법.

Abstract
Hydro-elastoplastic analysis of floating plate structures subjected to time-dependent external loads is presented, in which elastoplastic material behaviors are coupled with linear surface gravity waves. Time-domain incremental coupled equations for the analysis are derived as formulating incremental equilibrium equations of floating plate structure and impulse responses functions associated with hydrodynamic pressures in the time domain. The present formulation can describe the interactions between fluids and structures with material nonlinearity. Also, a time-domain incremental nonlinear solution procedure is proposed. In the solution procedure, an implicit return mapping algorithm to simulate plastic behaviors of floating plate structures and a direct coupling method to construct frequency-wave inddependent metrics, which can be converted to IRFs by Fourier transformation, are employed. Through numerical examples of plate structures floating on the free surface of water, the capability and the performance of the proposed solution procedure are demonstrated.

Keywords Hydro-elastoplastic analysis, Floating plate structures, Very large floating structure(VLFS), Impulse response function, Nonlinear structural analysis, Finite element method, Boundary element method, Direct coupling method.

Table of Contents

List of Tables

List of Figures

Chapter 1. Introduction

1.1 Research Background

For a long time, hydrodynamic analysis of floating structures, like ships and offshore structure, has been conducted in order to investigate the structures' safe and economic design [1-9]. One of the most important issues in hydrodynamic analysis is how to deal with complicated interactions between floating structures and any surrounding fluid. The interactions are associated with the motions of structures responding to wave-induced forces and simultaneously the water waves generated due to the motions of the wetted surface of the structures. The problems of coupled fluid and structural dynamics need to be solved. As a result, analytical, experimental and numerical methods have been continuously developed and improved.

Most previous analysis methods are based on the assumption of rigid body motions and have been applied successfully in the design of floating structures where these motions are dominant. However, as flexible motions of floating structures are weighted more heavily in the hydrodynamic responses, this assumption becomes less valid and hydroelasticity that is concerned with coupling effects between elastic deformation of structures and fluid motion for the hydrodynamic analysis of the floating structures can be more crucial. The fundamental theory of hydroelastic analysis was established for ship design in the1980s by Bishop and Price [5].

Recently, very large floating structures (VLFSs) have attracted people's attentions for use as floating airports, storage facilities for oil and natural gas, floating bridges, floating islands, and so on [9-55]. The types of VLFSs may be divided into pontoon-type (e.g. Meg-floats in Japan) and semi-submersible-type (e.g. Mobile offshore Base (MOB) in USA) with regard to their geometry [10]. In the design of VLFSs, due to their hydrodynamic features as huge horizontal size compared to the wavelengths and relatively small bending rigidity, hydroelastic analysis should be performed to accurately predict their responses in waves.

Many methods of hydroelastic analysis of pontoon-type VLFSs, which are mostly modeled as plate structure, in the frequency domain or in the time domain have been proposed. Commonly adopted approach for the hydroelastic analysis of floating plate structures in the frequency domain separates hydrodynamic analysis based on the potential flow theory and dynamic response analysis of floating plate structures in terms of structural modes [5, 10, 22, 30]. On the other hand, several researchers have developed a direct coupling method, in which the structural and fluid equations are directly coupled with each other, and the coupled equations are solved simultaneously [39-44]. Compared to the commonly adopted approach, the coupling method has simpler solution procedure [42].

The hydroelastic analysis of floating plate structures in the time domain has been less well-studied than that in the frequency domain. However, several investigators have used the connection between the time-domain and frequency-domain solution for time-dependent hydroelastic problems. Two approaches have been mainly applied for the time-domain analysis. One is based on a direct time integration, which is solving time-dependent structure and fluid equations by a direct integration [56-59], and the other is based on a memory effect kernel and is known as the Cummins method [60]. Cummins derives time-dependent equations of rigid body motions for floating bodies, which involve so-called “impulse response functions (IRF),” such as memory functions and added mass at infinite frequency. The Cummins method is by far the more popular because there are some disadvantages in the direct time integration approaches, such as necessity of discretizing the entire structure and fluid domain and the relative high computational cost and time.

In large-scale bending structures with long spans like bridges, hinge connections have been very effectively used to reduce the bending moment of cross-sections. To obtain economically more effective structural designs, the same principle for VLFSs can be adopted. The hydroelastic analysis of floating plate structures with hinge connections or interconnected floating structures with hinges or rotational springs have been studied [44-55]. Previous studies usually focused on both numerical procedures to model the hinge connections and the hydroelastic responses of the floating plate structures with hinge connections. In addition, although the maximum responses are very important in the design of VLFSs, the effect of the number of hinge connections used on the maximum responses has not been studied well. It has also not been well known that the hydroelastic responses could increase due to the use of hinge connections.

When severe external loads are applied, nonlinear behaviors of floating structures (e.g. yielding, buckling, and fracturing) can occur. For safer and more economically effective designs, it is essential to accurately predict hydrodynamic responses beyond elastic limit for considering such nonlinear behaviors. Despite this, little related research for hydro-elastoplastic analysis, which is concerned with the interactions between elastoplastic behaviors with water waves, has been conducted [12, 14, 61-66].

In order to evaluate plastic behaviors of floating plate structure in waves, commonly used approach is to perform two step analysis: firstly, hydroelastic analysis is carried out for calculating wave loads, and then plastic analysis using quasi-static methods is performed, in which waves loads are statically applied in a structural model. That is, plastic behaviors of VLFS are obtained in quasi-static manner as applying the time history of pressure distribution and inertia force previously calculated from hydroelastic analysis [12]. In this approach, plastic behaviors are not considered when calculating wave loads. Hydro-elastoplasticity methods of a ship have been proposed. In these methods, an approach is that hydroelastic analysis is combined with quasi-static methods. ship’s responses and wave loads are calculated by hydroelastic analysis and bending stiffness is determined by the quasi-static method and then modified in the hydroelastic equation [65]. Another approach is that ship is modeled by two rigid body with a nonlinear rotation spring and hydrodynamic forces are evaluated taking account of plastic deformations of the spring by a nonlinear strip theory [63, 64]. However, for more accurate and effective nonlinear structural analysis of floating plate structures, it is necessary to develop directly interactive approaches between elastoplastic responses and hydrodynamic forces in the time domain.

1.2 Research Purpose

The main objective of this thesis is to present hydro-elastoplastic analysis of floating plate structures subjected to time-dependent external loads, in which elastoplastic material behaviors are coupled with linear surface gravity waves. In order to calculate linear hydrodynamic forces induced by the waves interacting with the surface of floating plate structures, Cummins method is employed as constructing IRFs from the corresponding forces in the frequency domain by Fourier transformation. Thus, it is important to accurately and effectively calculate hydrodynamic responses of floating plate structures subjected to incident regular waves.

For this purpose, a numerical procedure for hydroelastic analysis of floating plate structures based on a direct coupling method is firstly proposed. The finite element method (FEM) and boundary element method (BEM) are employed to discretize floating plates and surrounding fluids, respectively. The numerical results are in good agreement with the previous experimental results by Yago and Endo [15], thereby confirming the validity of the proposed hydroelastic analysis of floating plate structures

Furthermore, in order to solve the hydroelastic problems of floating plate structures with multiple hinge connections, a complete condensation method is derived for modeling hinge connections, in which the rotational degrees of freedom (DOFs) of the plate finite elements are released. The proposed formulation is mathematically complete because structural mass and stiffness matrices and fluid-structure interaction matrix are consistently condensed. The numerical analyses show the effect of the number of hinge connections used on the maximum bending moment and deflection of the floating plate structures according to the aspect ratio, bending stiffness and incident wavelength.

For hydro-elastoplastic analysis, time-domain incremental coupled equations are formulated. The present formulation can describe the interactions between fluids and structures with material nonlinearity. Also, a time-domain incremental nonlinear solution procedure is proposed, in which the floating plate structure is discretized using the finite element method, and the surrounding fluid is modeled using the boundary element method. The plastic behaviors of the floating plate structures are simulated using an implicit return mapping algorithm based on von Mises plasticity model with isotropic hardening. For hydroelastic and hydro-elastoplastic problems, the solutions of proposed procedure agree well with numerical results obtained with commercial software, LS-DYNA.

Finally, to investigate the performance of the numerical method for hydro-elastoplastic analysis, hydrodynamic problems of floating plate structures subjected to external forces in two or three dimensions are solved. For two dimensional problems, a series of benchmark calculations for the time-dependent motion of a floating elastic plate structure released from rest is considered and hydroelastic and hydro-elastoplastic responses are studied. Also, hydrodynamic problems of the experimental model used by Endo and Yago [16] are solved. For three dimensional problems, a floating double plate structure subjected to two load cases (i.e. impact load or dead weight and an incident wave-induced loads) are considered.

The proposed approach for hydro-elastoplastic analysis is applicable to hydroelastic as well as hydro-elastoplastic problems for floating beam or plate structures subjected to external loads such as impact, incident regular and irregular waves, and so on. Compared to LS-DYNA, it provides reasonable numerical solutions with relatively low computational cost. In addition, it is expected to easily extend the proposed method for hydro-elastoplastic analysis of three dimensional floating structures with other material nonlinearity model.

1.3 Dissertation Organization

This thesis consists of total 6 chapters as follows:

In Chapter 2, the mathematical formulations for hydroelastic analysis of floating plate structures interacting with incident gravity waves are presented. Equations of motion for floating plate structures and fluid are derived from principle of virtual work and the boundary integral equations, respectively. And then the directly coupled equations of motion for the hydroelastic analysis are discretized by the boundary element method for fluid and the finite element method for plate structures. Comparing to the previous experimental results, validation of the proposed numerical method is demonstrated.

In Chapter 3, hydroelastic problems of floating plate structures with multiple hinge connections in incident regular waves are considered. For modeling hinge connections, a complete condensation method is derived, in which the rotational DOFs of the plate finite elements are released. The most important feature of the proposed hinge model is its modeling capability, which is shown in numerical examples: floating plate problems with 1- and 2-directional multiple hinge connections. Thus, it is able to easily deal with the hydroelastic responses of floating plate structures with arbitrarily positioned multiple hinge connections. Through various numerical analyses, effects of the number of hinge connections used on the maximum bending moment and deflection of the floating plate structures are studied as considering aspect ratio, bending stiffness and incident wavelength.

In Chapter 4, the time-domain incremental coupled equations for hydro-elastoplastic analysis of floating plate structures subjected to external loads are presented. Incremental equilibrium equations of floating plate structure considering the three dimensional von Mises plasticity model with isotropic hardening are derived. Hydrodynamic pressures in the time domain are obtained by employing IRFs in Cummins method. And then a time-domain incremental nonlinear solution procedure is proposed. Through comparisons with the numerical results of LS-DYNA, the capability of the proposed numerical procedure is investigated.

In Chapter 5, the performance and capability of the numerical method for hydro-elastoplastic analysis are demonstrated. Hydrodynamic problems for floating plate structures in two and three dimensions are solved. The impact, dead weight, and incident wave-induced loads are considered as external loads acting on floating plate structures.

Chapter 6 present the conclusions of this thesis.

Chapter 2. Hydroelastic Analysis of Floating Plate Structures Based on a Direct Coupling Method

In this chapter, a formulation for hydroelastic analysis of floating plate structures in regular waves by employing a direct coupling method is presented. The finite element method is used to model floating plate structures. On the other hand, the boundary element method is employed to model surrounding fluid. The modeling capability of the proposed formulation is demonstrated through numerical examples.

2.1 Mathematical Formulations

The problem of a floating plate structure subjected to incident regular waves is considered, as shown in **Figure 2.1**. The floating plate structure is assumed to have homogeneous, isotropic and linear elastic material and the fluid flow is incompressible, inviscid, and irrotational. The motions of the floating plate structure and the amplitudes of incident regular waves are small enough to use the linear theory. In addition, the surface tension effect is ignored and for simplicity, the atmospheric pressure is assumed to be zero.

The plate structure ($L \times B \times H$) is floating on the free surface of calm water with draft d. A fixed Cartesian coordinate system (x_1, x_2, x_3) is placed on the free surface and the flat bottom seabed is at $x_3 = -h$. The volume of the plate structure is V_S and of fluid is V_F. The fluid domain consists of the free surface S_F, the wet surface of the floating plate structure S_B, the surface S_∞, which is a circular cylinder with a sufficiently large radius R, and the seabed surface S_G. An incident regular wave with small amplitude a and angular frequency ω comes continuously from the positive x_1 axis with an angle θ.

To express the components of tensors and adopt the Einstein summation convention, subscripts i and j are introduced, which vary from 1 to 3. For simplicity, the draft is assumed to be zero. Thus, the condition for the static equilibrium at time $t = 0$ is automatically satisfied, which are described below in detail. Then, the components of the displacement vector $\mathbf{u}$ at time t are defined by

$$u_i(\mathbf{x};t) = x_i(t) - x_i(0), \tag{2.1}$$

where x_i are the components of the material point vector $\mathbf{x}$.

The total pressure fields in the fluid are

$$p(\mathbf{x};t) = -\rho_w g x_3(t) \quad \text{at} \quad t = 0, \tag{2.2a}$$

$$p(\mathbf{x};t) = -\rho_w g x_3(t) + p_d(\mathbf{x};t), \tag{2.2b}$$

where ρ_w is the density of the fluid, g is the acceleration of gravity, and p_d is the hydrodynamic pressure.

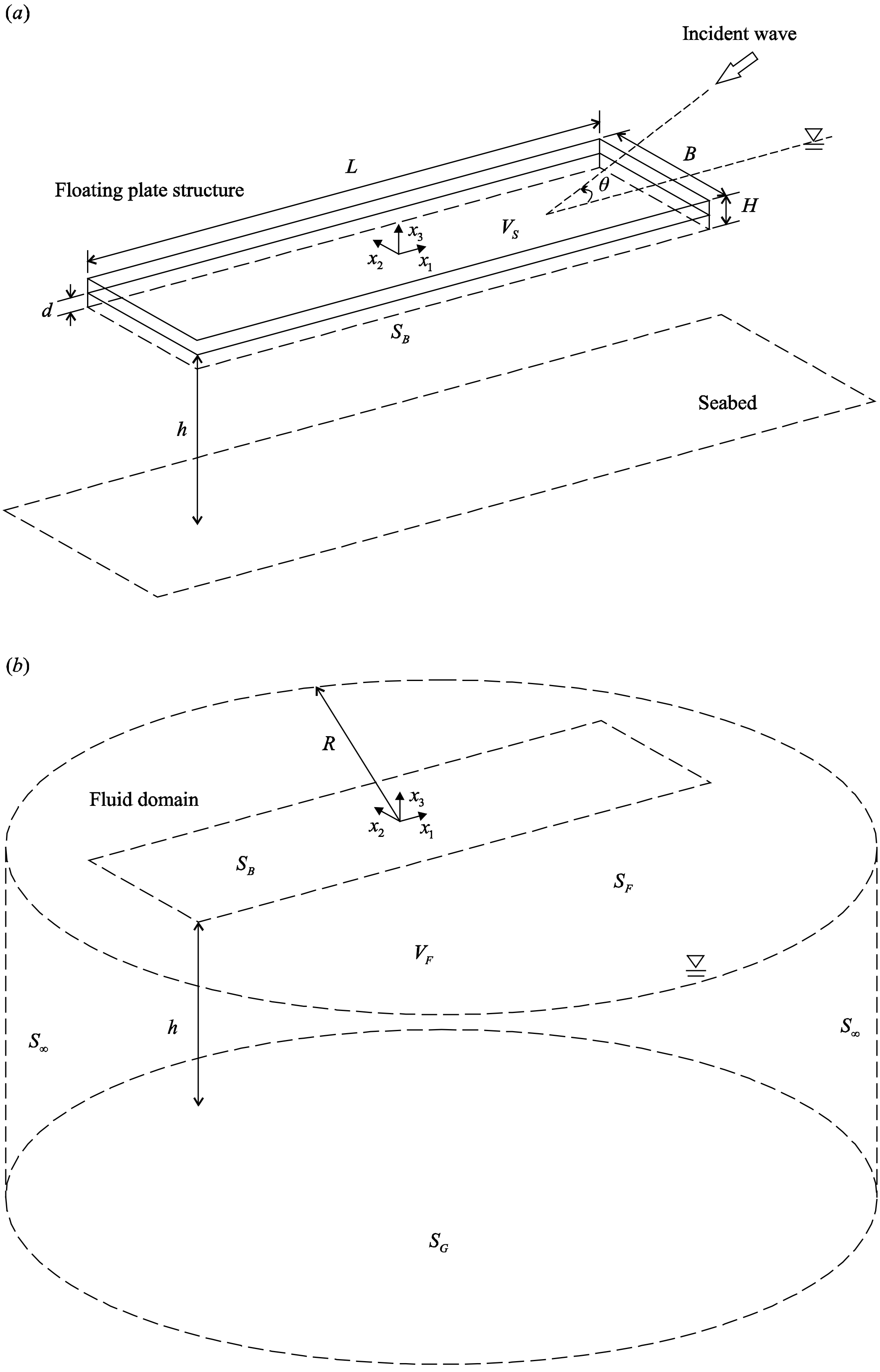

Figure 2.1. Problem description for floating plate structure subjected to an incident regular wave: (a) floating plate structure and (b) fluid domain.

The equilibrium equations of the floating plate structure at time t

$$\frac{\partial \sigma_{ij}}{\partial x_j} - \rho_s g \delta_{i3} - \rho_s \ddot{u}_i = 0 \quad \text{in} \quad V_S \,, \tag{2.3a}$$

$$\sigma_{ij} n_j = -p n_i \quad \text{on} \quad S_B \,, \tag{2.3b}$$

where σ_{ij} are components of the Cauchy stress tensor, ρ_s is the structural density, δ_{i3} is the Kronecker delta, n_i denotes the unit normal vector outward from the plate structure to the fluid. Also, overdots denote the time derivative (i.e. $\dot{(\;)} = \frac{\partial (\;)}{\partial t}$, $\ddot{(\;)} = \frac{\partial^2 (\;)}{\partial t^2}$).

2.1.1 Formulation of the Floating Plate Structure

Then, the principle of virtual work at time t can be stated as [67]

$$\int_{V_S} \sigma_{ij} \delta e_{ij} \mathrm{d}V = -\int_{V_S} \rho_s g \delta u_3 \mathrm{d}V + \int_{S_B} \rho_w g x_3 n_i \delta u_i \mathrm{d}S - \int_{S_B} p_d n_i \delta u_i \mathrm{d}S - \int_{V_S} \rho_s \ddot{u}_i \delta u_i \mathrm{d}V \,, \tag{2.4}$$

where

$$\delta e_{ij} = \frac{1}{2}\left(\frac{\partial \delta u_i}{\partial x_j} + \frac{\partial \delta u_j}{\partial x_i} \right), \tag{2.5}$$

in which δu_i are components of the virtual displacement vector imposed on the configuration at time t, and δe_{ij} are components of the virtual strain tensor corresponding to the virtual displacements. In the static equilibrium at time $t = 0$, in which the hydrodynamic pressure p_d and the acceleration $\ddot{u}_i$ are equal to zero, Equation (2.4) becomes

$$\int_{V_S} \sigma_{ij} \delta e_{ij} \mathrm{d}V + \int_{V_S} \rho_s g \delta u_3 \mathrm{d}V - \int_{S_B} \rho_w g x_3 n_i \delta u_i \mathrm{d}S = 0 \,. \tag{2.6}$$

According to assumptions, which is that the motion of the floating plate structure is small, and the linear elastic material is considered, the integral term on the left-hand side of Equation (2.4) can be written as

$$\int_{V_S(t)} \sigma_{ij}(\mathbf{x};t) \delta e_{ij} \mathrm{d}V = \int_{V_S(0)} C_{ijkl} e_{kl} \delta e_{ij} \mathrm{d}V + \int_{V_S(0)} \sigma_{ij}(\mathbf{x};0) \delta e_{ij} \mathrm{d}V \,, \tag{2.7}$$

where

$$e_{ij} = \frac{1}{2}\left(\frac{\partial u_i}{\partial x_j} + \frac{\partial u_j}{\partial x_i} \right), \tag{2.8}$$

in which e_{ij} are components of the linear strain tensor, and C_{ijkl} are components of the elastic stress-strain relation tensor.

Also, the second integral term on the right-hand side of Equation (2.4) can be written as

$$\int_{S_B(t)} \rho_w g x_3(t) n_i(\mathbf{x};t)\delta u_i \mathrm{d}S = \int_{S_B(0)} \rho_w g x_3(0) n_i(\mathbf{x};0)\delta u_i \mathrm{d}S + \int_{S_B(0)} \rho_w g u_3 n_i(\mathbf{x};0)\delta u_i \mathrm{d}S \,, \tag{2.9}$$

in which the change of wet surface is assumed to be negligible.

After substituting Equation (2.7) and (2.9) into the terms and applying the condition (2.6) for the static equilibrium, Equation (2.4) becomes:

$$\int_{V_S} \rho_s \ddot{u}_i \delta u_i \mathrm{d}V + \int_{V_S} C_{ijkl} e_{kl} \delta e_{ij} \mathrm{d}V - \int_{S_B} \rho_w g u_3 n_i \delta u_i \mathrm{d}S + \int_{S_B} p_d n_i \delta u_i \mathrm{d}S = 0 \,. \tag{2.10}$$

Invoking a harmonic response to the excitation of an incident regular wave with angular frequency ω, the steady state equation can be finally obtained as

$$-\omega^2 \int_{V_S} \rho_s \tilde{u}_i \delta\tilde{u}_i \mathrm{d}V + \int_{V_S} C_{ijkl} \tilde{e}_{kl} \delta\tilde{e}_{ij} \mathrm{d}V - \int_{S_B} \rho_w g \tilde{u}_3 n_i \delta\tilde{u}_i \mathrm{d}S + \int_{S_B} \tilde{p}_d n_i \delta\tilde{u}_i \mathrm{d}S = 0 \,, \tag{2.11}$$

where

$$u_i(\mathbf{x};t) = \mathrm{Re}\left\{\tilde{u}_i(\mathbf{x})e^{j\omega t}\right\}, \quad e_{ij}(\mathbf{x};t) = \mathrm{Re}\left\{\tilde{e}_{ij}(\mathbf{x})e^{j\omega t}\right\}, \; p_d(\mathbf{x};t) = \mathrm{Re}\left\{\tilde{p}_d(\mathbf{x})e^{j\omega t}\right\}, \quad j = \sqrt{-1} \,. \tag{2.12}$$

2.1.2 Formulation of the Fluid

In the steady state, the velocity potential $\phi(\mathbf{x};t)$ is governed by

$$\phi(\mathbf{x};t) = \mathrm{Re}\left\{\tilde{\phi}(\mathbf{x})e^{j\omega t}\right\}, \tag{2.13a}$$

$$\nabla^2 \tilde{\phi} = 0 \quad \text{in} \quad V_F \,, \tag{2.13b}$$

$$\frac{\partial \tilde{\phi}}{\partial x_3} = \frac{\omega^2}{g}\tilde{\phi} \quad \text{for} \quad x_3 = 0 \quad \text{on} \quad S_F \,, \tag{2.13c}$$

$$\frac{\partial \tilde{\phi}}{\partial x_3} = 0 \quad \text{on} \quad S_G \,, \tag{2.13d}$$

$$\sqrt{R}\left(\frac{\partial}{\partial R} + jk\right)\left(\tilde{\phi} - \tilde{\phi}^I\right) = 0 \quad \text{on} \quad S_\infty \quad (R \to \infty), \tag{2.13e}$$

$$\frac{\partial \tilde{\phi}}{\partial n} = -j\omega \tilde{u}_3 \quad \text{on} \quad S_B \,, \tag{2.13f}$$

where ∇^2 is the Laplace operator, k is the wave number, and $\tilde{\phi}^I$ is the velocity potential for the incident wave. The condition (2.13c) is the combined free surface boundary condition linearized on $x_3 = 0$ [68, 69], the condition (2.13e) is the Sommerfeld radiation condition [68]. The body boundary condition (2.13f) means that the normal velocities of plate structure and fluid on the wet surface should be the same. The conditions (2.13b) and (2.13f) are approximated on the configuration of the static equilibrium at time $t = 0$.

The incident velocity potential $\tilde{\phi}^I$ and dispersion relationship according to water depths are given in Table 2-1 [68, 69].

Table 2.1. Definitions of incident velocity potentials and dispersion relationships.

Cases	Incident velocity potential $\tilde{\phi}^I$	Dispersion relationship
Finite depth	$j\dfrac{ag}{\omega}\dfrac{\cosh k(x_3+h)}{\cosh kh}e^{jk(x_1\cos\theta+x_2\cos\theta)}$	$k\tanh kh-\dfrac{\omega^2}{g}=0$
Infinite depth	$j\dfrac{ag}{\omega}e^{kx_3}e^{jk(x_1\cos\theta+x_2\cos\theta)}$	$k-\dfrac{\omega^2}{g}=0$

The Laplace equation and boundary conditions of the velocity potential $\tilde{\phi}$ in Equation (2.13) can be transformed in a useful integral form, i.e., as the boundary integral equation by the Green's theorem. The Green's second identity for the velocity potential $\tilde{\phi}$ and the Green's function, which is generated by a source potential pulsated at position ξ_i with angular frequency ω and strength -4π, takes the following form:

$$\int_{V_F}\left(\nabla^2\tilde{\phi}(\mathbf{x})\tilde{G}(\mathbf{x},\boldsymbol{\xi})-\tilde{\phi}(\mathbf{x})\nabla^2\tilde{G}(\mathbf{x},\boldsymbol{\xi})\right)dV_x=\int_{S_C}\left(\tilde{\phi}(\mathbf{x})\frac{\partial\tilde{G}(\mathbf{x},\boldsymbol{\xi})}{\partial n(\mathbf{x})}-\frac{\partial\tilde{\phi}(\mathbf{x})}{\partial n(\mathbf{x})}\tilde{G}(\mathbf{x};\boldsymbol{\xi})\right)dS_x\,, \tag{2.14}$$

where S_C is closed surface bounding the fluid domain V_F, and the subscript x means the variable of integration.

If the free surface Green's function $\tilde{G}$, see Appendix A, is employed, the boundary integral equation for the spatial position x_i on the wet surface S_B can be given by

$$4\pi\tilde{\phi}(\mathbf{x})+p.v.\int_{S_B}\left(\tilde{\phi}(\boldsymbol{\xi})\frac{\omega^2}{g}+\frac{\partial\tilde{\phi}(\boldsymbol{\xi})}{\partial n(\boldsymbol{\xi})}\right)\tilde{G}(\mathbf{x},\boldsymbol{\xi})dS_\xi=4\pi\tilde{\phi}^I(\mathbf{x})\,, \tag{2.15}$$

where $p.v.$ indicates the Cauchy principal value. The detailed procedure of formulation of the boundary integral equation can be found in Reference [42].

For the boundary element approximations, Equation (2.15) is multiplied by a test function $\delta\tilde{\phi}$, and integrated over the wet surface S_B. Then, the following equation are obtained:

$$4\pi\int_{S_B}\tilde{\phi}(\mathbf{x})\delta\tilde{\phi}dS_x+\int_{S_B}p.v.\int_{S_B}\left(\tilde{\phi}(\boldsymbol{\xi})\frac{\omega^2}{g}+\frac{\partial\tilde{\phi}(\boldsymbol{\xi})}{\partial n(\boldsymbol{\xi})}\right)\tilde{G}(\mathbf{x},\boldsymbol{\xi})dS_\xi\delta\tilde{\phi}dS_x=4\pi\int_{S_B}\tilde{\phi}^I(\mathbf{x})\delta\tilde{\phi}dS_x\,. \tag{2.16}$$

2.1.3 Coupled Equations

To obtain coupled equations, the Bernoulli equation and the body boundary condition (2.13f) are applied to the formulations for the floating plate structure (2.11) and fluid (2.16). Using the linearized Bernoulli equation at the static equilibrium configuration, the hydrodynamic pressure $\tilde{p}_d$ can be represented as

$$\tilde{p}_d = -j\omega\rho_w\tilde{\phi} \,, \tag{2.17}$$

Then, by substituting Equation (2.17) and (2.13f) with (2.11) and (2.16), respectively, the following coupled equations are obtained:

$$-\omega^2\int_{V_S}\rho_s\tilde{u}_i\delta\tilde{u}_i\mathrm{d}V + \int_{V_S}C_{ijkl}\tilde{e}_{kl}\delta\tilde{e}_{ij}\mathrm{d}V - \int_{S_B}\rho_w g\tilde{u}_3 n_i\delta\tilde{u}_i\mathrm{d}S - j\omega\int_{S_B}\rho_w\tilde{\phi}n_i\delta\tilde{u}_i\mathrm{d}S = 0 \,, \tag{2.18}$$

and

$$4\pi\int_{S_B}\tilde{\phi}\delta\tilde{\phi}dS_x + \int_{S_B}p.v.\int_{S_B}\left(\tilde{\phi}\frac{\omega^2}{g} + j\omega\tilde{u}_i n_i\right)\tilde{G}dS_\xi\delta\tilde{\phi}dS_x = 4\pi\int_{S_B}\tilde{\phi}^I\delta\tilde{\phi}dS_x \,. \tag{2.19}$$

Alternatively, the coupled equations can be derived with respect to the total water pressure $\tilde{p}$ and displacement $\tilde{u}_i$:

$$-\omega^2\int_{V_S}\rho_s\tilde{u}_i\delta\tilde{u}_i\mathrm{d}V + \int_{V_S}C_{ijkl}\tilde{e}_{kl}\delta\tilde{e}_{ij}\mathrm{d}V - \int_{S_B}\tilde{p}\delta\tilde{u}_3\mathrm{d}S = 0 \,, \tag{2.20}$$

and

$$-\int_{S_B}\tilde{u}_3\delta\tilde{p}\mathrm{d}S_x - \frac{1}{\rho_w g}\int_{S_B}\tilde{p}\delta\tilde{p}\mathrm{d}S_x - \frac{\omega^2}{4\pi\rho_w g^2}\int_{S_B}p.v.\int_{S_B}\tilde{p}\tilde{G}\mathrm{d}S_\xi\delta\tilde{p}\mathrm{d}S_x = j\frac{\omega}{g}\int_{S_B}\tilde{\phi}^I\delta\tilde{p}\mathrm{d}S_x \,, \tag{2.21}$$

where $p(\mathbf{x};t) = \mathrm{Re}\left\{\tilde{p}(\mathbf{x})e^{j\omega t}\right\}$, and $\delta\tilde{p}$ is a test function.

2.2 Numerical Procedure

In this section, the matrix formulation for the hydroelaistc problem of floating plate structures subjected to incident waves. The coupled equations (2.20) and (2.21) are discretized by the finite and boundary element methods and result in the following matrix form

$$\begin{bmatrix} -\omega^2\mathbf{S}_M + \mathbf{S}_K & -\mathbf{C}_{up} \\ -\mathbf{C}_{up}^T & -\mathbf{F}_M - \mathbf{F}_G \end{bmatrix}\begin{bmatrix}\hat{\mathbf{u}} \\ \hat{\mathbf{p}}\end{bmatrix} = \begin{bmatrix}\mathbf{0} \\ \mathbf{R}_I\end{bmatrix}, \tag{2.22}$$

in which $\hat{\mathbf{u}}$ and $\hat{\mathbf{p}}$ are the unknown displacement and pressure vectors, respectively, and the submatrices and subvectors are defined as follows

$$\int_{V_F} \rho_s \tilde{u}_i \delta\tilde{u}_i \mathrm{d}V = \delta\hat{\mathbf{u}}^T \mathbf{S}_M \hat{\mathbf{u}} \,, \tag{2.23a}$$

$$\int_{V_F} C_{ijkl} \tilde{e}_{kl} \; \delta\tilde{e}_{ij} \mathrm{d}V = \delta\hat{\mathbf{u}}^T \mathbf{S}_K \hat{\mathbf{u}} \,, \tag{2.23b}$$

$$\int_{S_B} \tilde{p} \delta\tilde{u}_3 \mathrm{d}S = \delta\hat{\mathbf{u}}_3{}^T \mathbf{C}_{up} \hat{\mathbf{p}} \,, \tag{2.23c}$$

$$\frac{1}{\rho_w g} \int_{S_B} \tilde{p} \delta\tilde{p} \mathrm{d}S = \delta\hat{\mathbf{p}}^T \mathbf{F}_M \hat{\mathbf{p}} \,, \tag{2.23d}$$

$$\frac{\omega^2}{4\pi\rho_w g^2} \int_{S_B} p.v. \int_{S_B} \tilde{p}\tilde{G} \mathrm{d}S_\xi \delta\tilde{p} \; \mathrm{d}S_x = \delta\hat{\mathbf{p}}^T \mathbf{F}_G \hat{\mathbf{p}} \;\,, \tag{2.23e}$$

$$j \frac{\omega}{g} \int_{S_B} \tilde{\phi}^I \delta\tilde{p} \mathrm{d}S = \delta\hat{\mathbf{p}}^T \mathbf{R}_I \,, \tag{2.23f}$$

where $\mathbf{S}_M$ and $\mathbf{S}_K$ are the matrices for structural mass and stiffness, $\mathbf{C}_{up}$ is the symmetric matrix for the fluid-structure interaction, in which the total water pressure $\hat{\mathbf{p}}$ and structural displacement $\hat{\mathbf{u}}$ are directly coupled.

For the finite element model of Mindlin type plate structures, the 4-node MITC plate finite element (MITC4) is employed, in which the MITC (Mixed Interpolation of Tensorial Components) method is applied to alleviate undesired shear locking phenomenon [70-78]. For the boundary element model of fluid, a 4-node quadrilateral boundary element is used, in which the isoparametric procedure is adopted for the geometry and pressure interpolations on boundary surface.

By condensing out the total water pressure $\hat{\mathbf{p}}$ in Equation (2.22), the condensed structural equation with added mass, radiated wave damping, wave excitation force vector, and hydrostatic stiffness is obtained:

$$\left[-\omega^2(\mathbf{S}_M + \mathbf{S}_{MA}) + j\omega\mathbf{S}_{CW} + \mathbf{S}_K + \mathbf{S}_H\right]\hat{\mathbf{u}} = \mathbf{R}_W \,, \tag{2.24}$$

where

$$\mathbf{S}_{MA} = -\frac{1}{\omega^2} \times \mathrm{Re}\left\{\mathbf{C}_{up}(\mathbf{F}_M + \mathbf{F}_G)^{-1}\mathbf{C}_{up}^T - \mathbf{S}_H\right\}, \tag{2.25a}$$

$$\mathbf{S}_{CW} = \frac{1}{\omega} \times \mathrm{Im}\left\{\mathbf{C}_{up}(\mathbf{F}_M + \mathbf{F}_G)^{-1}\mathbf{C}_{up}^T - \mathbf{S}_H\right\}, \tag{2.25b}$$

$$\mathbf{R}_W = -\mathbf{C}_{up}(\mathbf{F}_M + \mathbf{F}_G)^{-1}\mathbf{R}_I \,, \tag{2.25c}$$

$$\hat{\mathbf{u}}_3 \mathbf{S}_H \delta\hat{\mathbf{u}} = \int_{S_B} \rho_w g \tilde{u}_3 n_i \delta\tilde{u}_i \mathrm{d}S \,, \tag{2.25d}$$

in which $\mathbf{S}_{MA}$, $\mathbf{S}_{CW}$, and $\mathbf{S}_H$ are the matrices for added mass, radiated wave damping, and hydrostatic stiffness, and $\mathbf{R}_W$ is wave excitation force vector.

2.3 Numerical Examples

In this section, to verify the formulation proposed, numerical solutions are compared with experimental results conducted by Yago and Endo [15]. The details of the floating plate model used in the hydroelastic experiments are given in **Table 2.2**. In all the numerical examples, the water depth is assumed to be finite, the density of water ρ_w is $1000 kg/m^3$ and the acceleration of gravity g is $9.8 m/s^2$.

Table 2.2. Details of the floating plate model used in the hydroelastic experiments by Yago and Endo

Parameter	Value
Length (L)	$9.75m$
Width (B)	$1.95m$
Thickness(H)	$0.0545m$
Draft (d)	$0.0167m$
Water depth(h)	$1.9m$
Bending stiffness (EI)	$17.522kNm^2$

32 (in length) × 6 (in breadth) mesh of the MITC4 plate elements and the 4-node node quadrilateral boundary element is used. Hydroelastic analysis of the floating plate structure subjected to incident regular waves with four angles ($0°$, $30°$, $60°$ and $90°$) and six different wavelengths ($\lambda / L = 0.1$, 0.2 , 0.3 , 0.4 , 0.5 and 0.6) is performed as shown in **Figure 2.2**. The numerical and experimental results are comparison in the following **Figures 2.3 ~ 2.6** and **Tables 2.3 ~ 2.6**. The numerical results agree well with the experimental results.

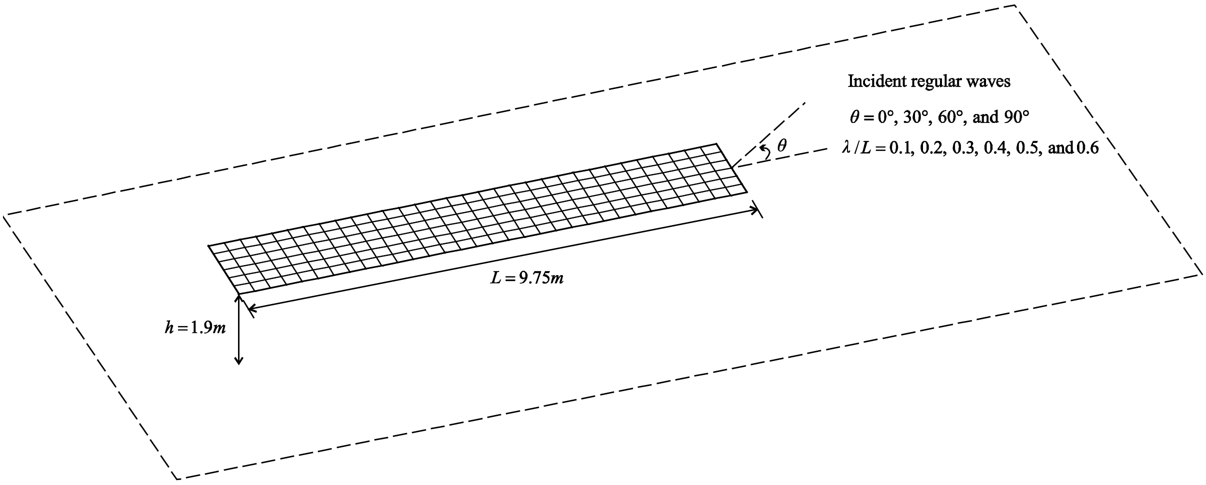

Figure 2.2. Description of hydroelastic problems and finite and boundary element meshes

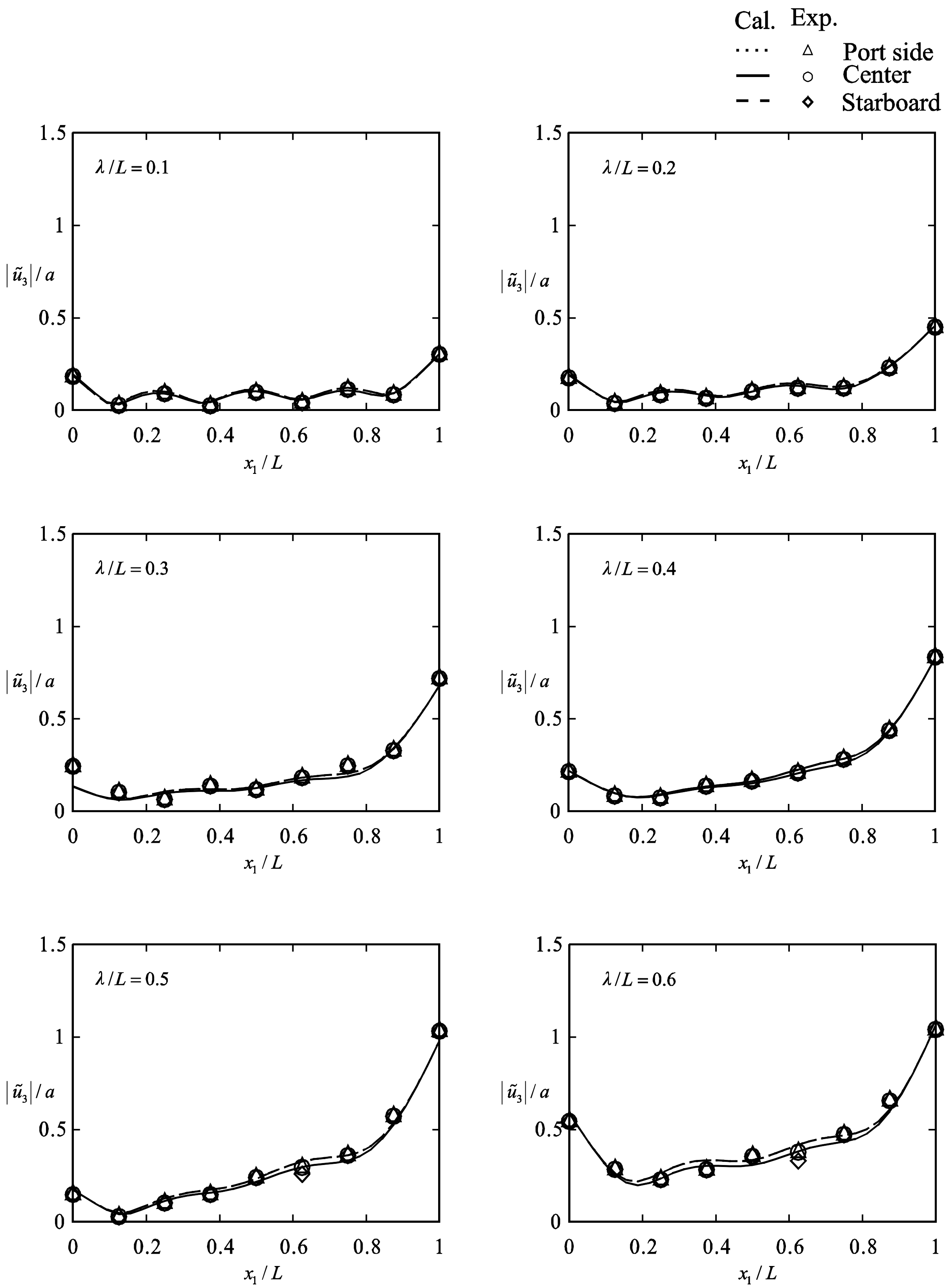

Figure 2.3. RAOs of deflection of the floating plate structures under incident regular waves with an angle ($\theta = 0°$) and six wavelengths ($\lambda / L = 0.1$, 0.2, 0.3, 0.4, 0.5 and 0.6).

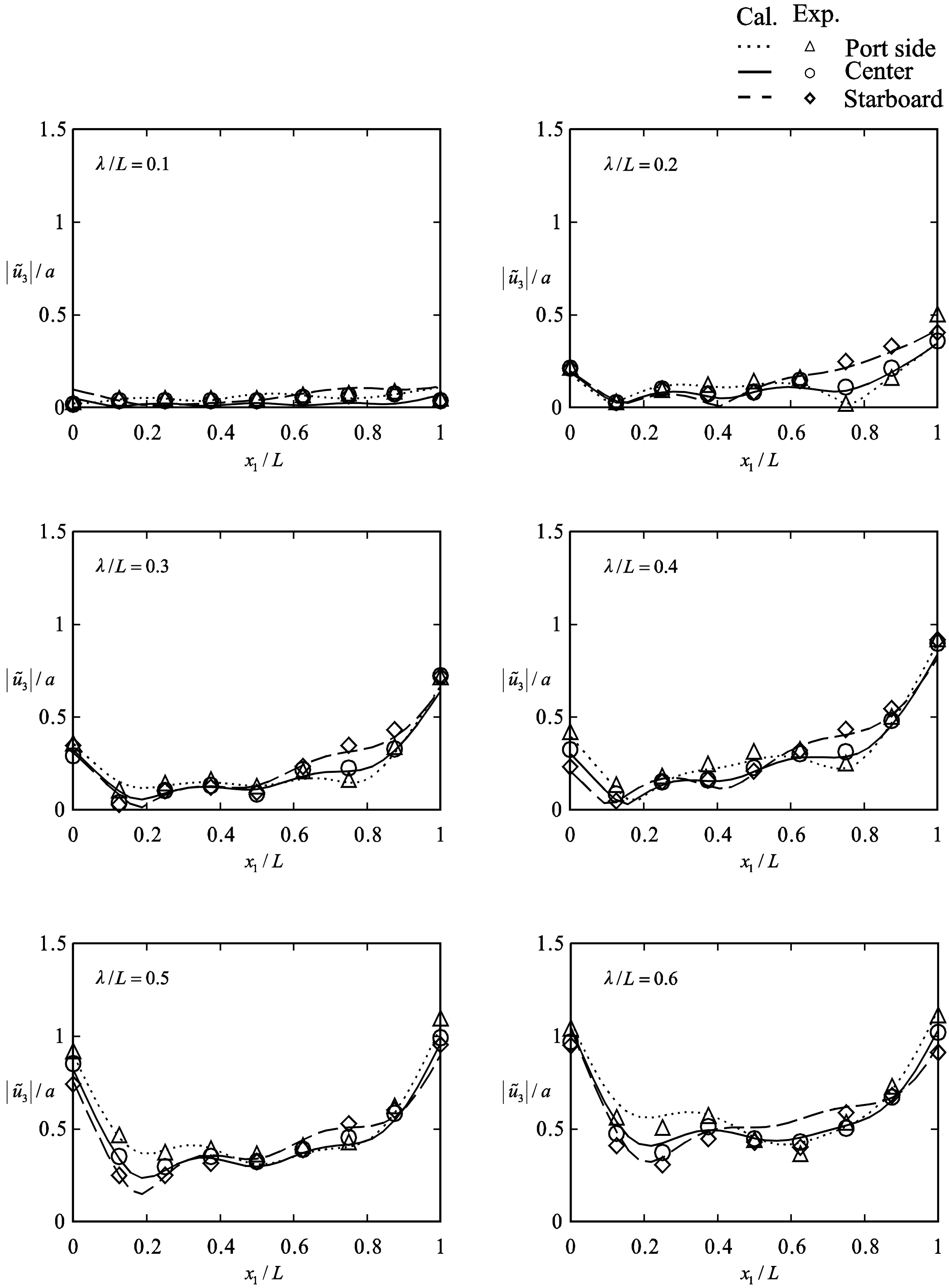

Figure 2.4. RAOs of deflection of the floating plate structures under incident regular waves with an angle ($\theta = 30°$) and six wavelengths ($\lambda/L = 0.1$, 0.2, 0.3, 0.4, 0.5 and 0.6).

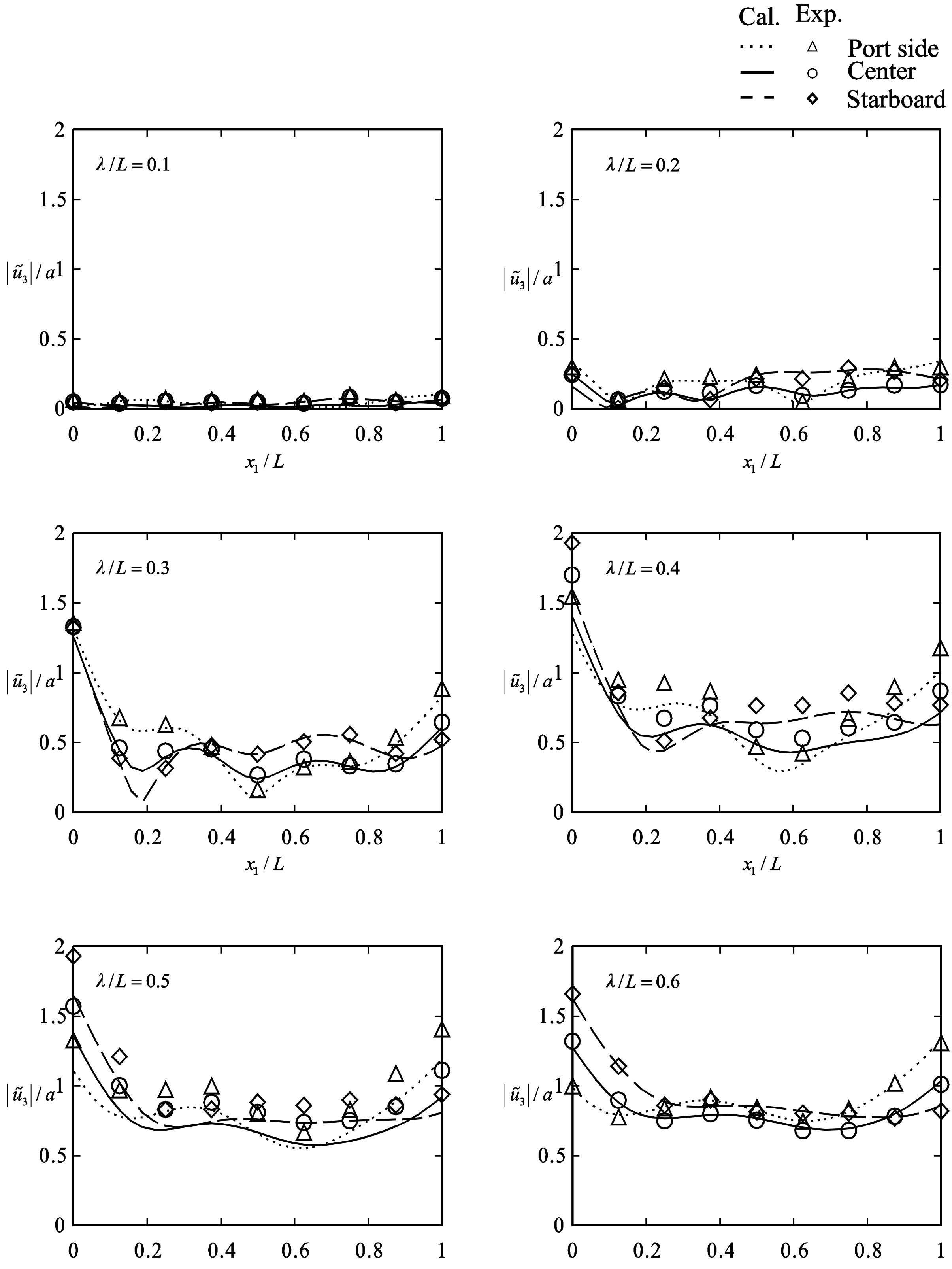

Figure 2.5. RAOs of deflection of the floating plate structures under incident regular waves with an angle ($\theta = 60°$) and six wavelengths ($\lambda / L = 0.1$, 0.2, 0.3, 0.4, 0.5 and 0.6).

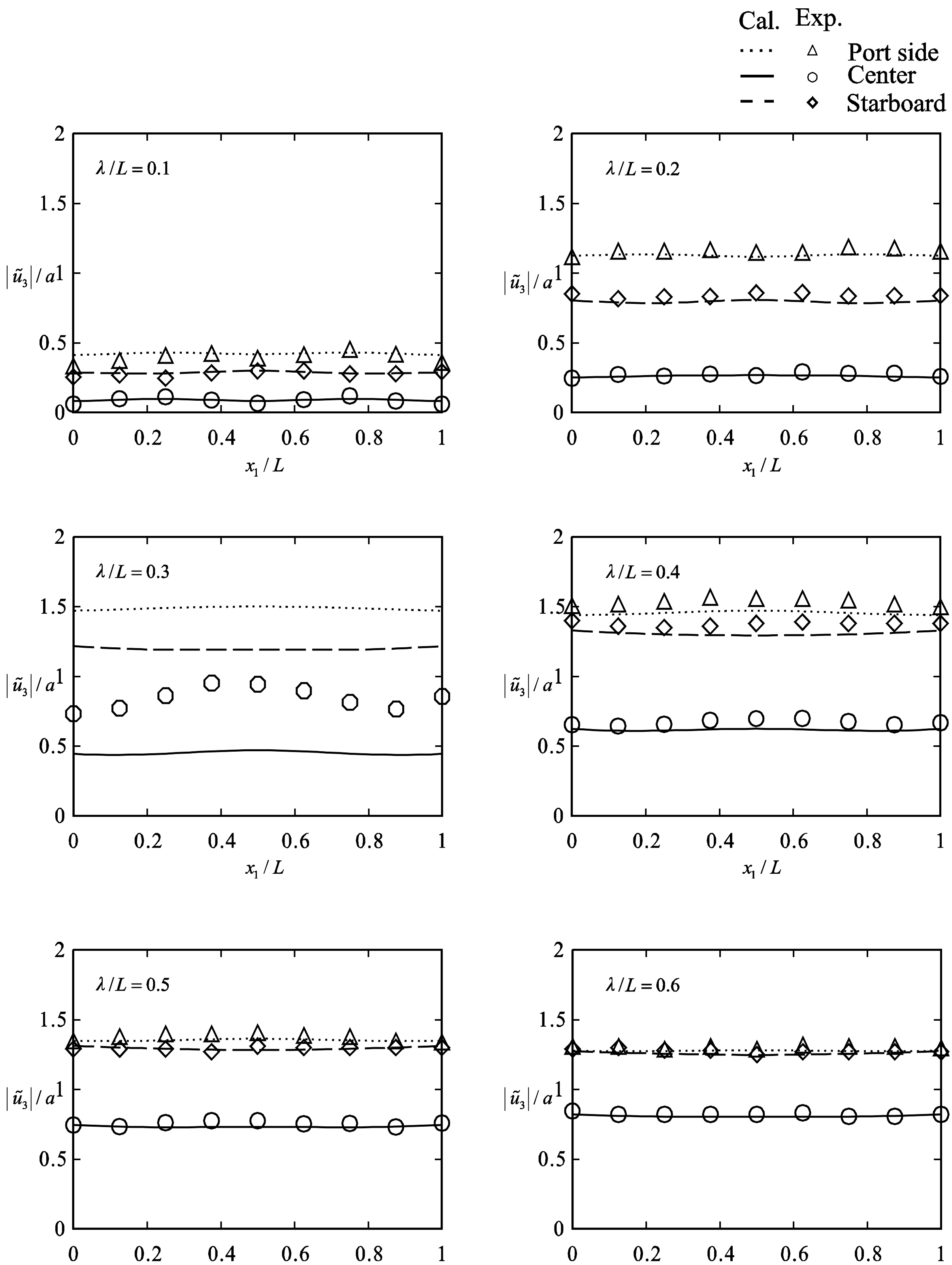

Figure 2.6. RAOs of deflection of the floating plate structures under incident regular waves with an angle ($\theta = 90°$) and six wavelengths ($\lambda / L = 0.1$, 0.2, 0.3, 0.4, 0.5 and 0.6).

Table 2.3. RAOs of deflection of the floating plate structures under incident regular waves with an angle ($\theta = 0°$) and six wavelengths ($\lambda / L = 0.1$, 0.2, 0.3, 0.4, 0.5 and 0.6) obtained by the present procedure and the experiments.

λ / L	Points	Calculation			Experiment		
		Starboard	Center	Port side	Starboard	Center	Port side
0.1	0.000	0.189	0.197	0.189	0.183	0.183	0.183
	0.125	0.038	0.030	0.038	0.026	0.026	0.026
	0.250	0.101	0.090	0.101	0.089	0.089	0.089
	0.375	0.047	0.044	0.047	0.024	0.024	0.024
	0.500	0.111	0.103	0.111	0.096	0.096	0.096
	0.625	0.061	0.056	0.061	0.040	0.040	0.040
	0.750	0.120	0.107	0.120	0.112	0.112	0.112
	0.875	0.093	0.092	0.093	0.083	0.083	0.083
	1.000	0.303	0.308	0.303	0.302	0.302	0.302
0.2	0.000	0.192	0.195	0.192	0.174	0.174	0.174
	0.125	0.045	0.044	0.045	0.037	0.037	0.037
	0.250	0.106	0.096	0.106	0.082	0.082	0.082
	0.375	0.086	0.079	0.086	0.064	0.064	0.064
	0.500	0.109	0.101	0.109	0.101	0.101	0.101
	0.625	0.145	0.133	0.145	0.119	0.119	0.119
	0.750	0.129	0.117	0.129	0.119	0.119	0.119
	0.875	0.240	0.236	0.240	0.229	0.229	0.229
	1.000	0.461	0.460	0.461	0.448	0.448	0.448
0.3	0.000	0.133	0.135	0.133	0.242	0.242	0.242
	0.125	0.064	0.062	0.064	0.101	0.101	0.101
	0.250	0.105	0.096	0.105	0.063	0.063	0.063
	0.375	0.118	0.109	0.118	0.136	0.136	0.136
	0.500	0.134	0.125	0.134	0.116	0.116	0.116
	0.625	0.181	0.166	0.181	0.181	0.181	0.181
	0.750	0.205	0.187	0.205	0.245	0.245	0.245
	0.875	0.342	0.338	0.342	0.327	0.327	0.327
	1.000	0.681	0.682	0.681	0.717	0.717	0.717
0.4	0.000	0.219	0.220	0.219	0.213	0.213	0.213
	0.125	0.097	0.097	0.097	0.082	0.082	0.082
	0.250	0.091	0.086	0.091	0.072	0.072	0.072
	0.375	0.134	0.126	0.134	0.135	0.135	0.135
	0.500	0.162	0.151	0.162	0.162	0.162	0.162
	0.625	0.225	0.204	0.225	0.207	0.207	0.207
	0.750	0.284	0.260	0.284	0.280	0.280	0.280
	0.875	0.440	0.433	0.440	0.436	0.436	0.436
	1.000	0.831	0.832	0.831	0.833	0.833	0.833
0.5	0.000	0.175	0.174	0.175	0.147	0.147	0.147
	0.125	0.047	0.041	0.047	0.028	0.028	0.028
	0.250	0.126	0.113	0.126	0.101	0.101	0.101
	0.375	0.173	0.157	0.173	0.147	0.147	0.147
	0.500	0.235	0.215	0.235	0.239	0.239	0.239
	0.625	0.325	0.296	0.325	0.258	0.294	0.294
	0.750	0.360	0.331	0.360	0.359	0.359	0.359
	0.875	0.536	0.528	0.536	0.571	0.571	0.571
	1.000	0.982	0.982	0.982	1.031	1.031	1.031
0.6	0.000	0.588	0.588	0.588	0.543	0.543	0.543
	0.125	0.263	0.255	0.263	0.284	0.284	0.284
	0.250	0.265	0.236	0.265	0.228	0.228	0.228
	0.375	0.332	0.302	0.332	0.282	0.282	0.282
	0.500	0.334	0.306	0.334	0.354	0.354	0.354
	0.625	0.417	0.382	0.417	0.330	0.376	0.376
	0.750	0.467	0.433	0.467	0.472	0.472	0.472
	0.875	0.608	0.597	0.608	0.655	0.655	0.655
	1.000	1.065	1.065	1.065	1.040	1.040	1.040

Table 2.4. RAOs of deflection of the floating plate structures under incident regular waves with an angle ($\theta = 30°$) and six wavelengths ($\lambda / L = 0.1$, 0.2, 0.3, 0.4, 0.5 and 0.6) obtained by the present procedure and the experiments.

λ / L	Points	Calculation			Experiment		
		Starboard	**Center**	**Port side**	**Starboard**	**Center**	**Port side**
0.1	0.000	0.096	0.051	0.021	0.018	0.018	0.018
	0.125	0.037	0.004	0.044	0.037	0.037	0.037
	0.250	0.012	0.022	0.049	0.037	0.037	0.037
	0.375	0.023	0.007	0.039	0.037	0.037	0.037
	0.500	0.040	0.024	0.072	0.037	0.037	0.037
	0.625	0.074	0.011	0.065	0.055	0.055	0.055
	0.750	0.105	0.024	0.049	0.064	0.064	0.064
	0.875	0.098	0.020	0.070	0.074	0.074	0.074
	1.000	0.115	0.068	0.109	0.037	0.037	0.037
0.2	0.000	0.199	0.192	0.181	0.212	0.212	0.204
	0.125	0.036	0.025	0.030	0.028	0.028	0.019
	0.250	0.070	0.082	0.115	0.101	0.101	0.083
	0.375	0.023	0.060	0.114	0.074	0.074	0.111
	0.500	0.099	0.082	0.123	0.083	0.083	0.130
	0.625	0.170	0.107	0.122	0.147	0.147	0.148
	0.750	0.214	0.090	0.019	0.248	0.110	0.009
	0.875	0.302	0.192	0.168	0.331	0.212	0.148
	1.000	0.422	0.348	0.350	0.405	0.359	0.491
0.3	0.000	0.310	0.324	0.358	0.347	0.291	0.347
	0.125	0.082	0.101	0.151	0.028	0.038	0.094
	0.250	0.081	0.090	0.129	0.103	0.103	0.131
	0.375	0.126	0.123	0.147	0.122	0.131	0.150
	0.500	0.130	0.111	0.128	0.094	0.084	0.113
	0.625	0.241	0.180	0.166	0.234	0.216	0.197
	0.750	0.312	0.208	0.145	0.347	0.225	0.150
	0.875	0.392	0.320	0.306	0.431	0.328	0.328
	1.000	0.652	0.642	0.670	0.722	0.722	0.703
0.4	0.000	0.211	0.305	0.398	0.232	0.324	0.407
	0.125	0.039	0.052	0.114	0.047	0.084	0.121
	0.250	0.167	0.134	0.140	0.150	0.150	0.169
	0.375	0.128	0.154	0.218	0.161	0.161	0.235
	0.500	0.192	0.205	0.268	0.208	0.227	0.301
	0.625	0.344	0.280	0.278	0.321	0.302	0.311
	0.750	0.404	0.286	0.223	0.433	0.313	0.238
	0.875	0.512	0.456	0.468	0.545	0.480	0.490
	1.000	0.819	0.842	0.901	0.917	0.898	0.907
0.5	0.000	0.756	0.820	0.900	0.741	0.852	0.907
	0.125	0.250	0.338	0.454	0.250	0.352	0.454
	0.250	0.247	0.277	0.385	0.250	0.296	0.361
	0.375	0.358	0.342	0.396	0.315	0.352	0.380
	0.500	0.338	0.297	0.309	0.324	0.324	0.352
	0.625	0.443	0.370	0.366	0.389	0.389	0.398
	0.750	0.507	0.415	0.403	0.528	0.454	0.417
	0.875	0.566	0.547	0.587	0.602	0.583	0.611
	1.000	0.901	0.966	1.052	0.954	0.991	1.083
0.6	0.000	1.046	1.052	1.084	0.950	0.969	1.030
	0.125	0.483	0.537	0.642	0.410	0.475	0.550
	0.250	0.346	0.423	0.570	0.307	0.373	0.494
	0.375	0.488	0.493	0.576	0.447	0.512	0.559
	0.500	0.507	0.449	0.456	0.429	0.447	0.429
	0.625	0.553	0.452	0.425	0.401	0.429	0.354
	0.750	0.618	0.518	0.513	0.587	0.503	0.522
	0.875	0.668	0.654	0.710	0.680	0.671	0.717
	1.000	0.950	1.034	1.145	0.913	1.020	1.100

Table 2.5. RAOs of deflection of the floating plate structures under incident regular waves with an angle ($\theta = 60°$) and six wavelengths ($\lambda / L = 0.1$, 0.2, 0.3, 0.4, 0.5 and 0.6) obtained by the present procedure and the experiments.

λ / L	Points	Calculation			Experiment		
		Starboard	**Center**	**Port side**	**Starboard**	**Center**	**Port side**
0.1	0.000	0.045	0.022	0.032	0.049	0.049	0.049
	0.125	0.025	0.018	0.053	0.040	0.040	0.040
	0.250	0.022	0.015	0.052	0.055	0.055	0.055
	0.375	0.044	0.019	0.030	0.046	0.046	0.046
	0.500	0.034	0.020	0.023	0.049	0.049	0.049
	0.625	0.050	0.019	0.009	0.040	0.040	0.040
	0.750	0.071	0.023	0.018	0.080	0.080	0.080
	0.875	0.053	0.028	0.074	0.046	0.046	0.046
	1.000	0.045	0.064	0.105	0.074	0.074	0.074
0.2	0.000	0.163	0.251	0.336	0.245	0.245	0.282
	0.125	0.058	0.024	0.044	0.063	0.063	0.051
	0.250	0.116	0.115	0.189	0.150	0.126	0.199
	0.375	0.084	0.065	0.196	0.066	0.115	0.213
	0.500	0.242	0.156	0.182	0.215	0.166	0.227
	0.625	0.261	0.103	0.033	0.216	0.094	0.032
	0.750	0.276	0.132	0.214	0.291	0.132	0.193
	0.875	0.273	0.151	0.279	0.268	0.170	0.281
	1.000	0.212	0.171	0.345	0.208	0.172	0.282
0.3	0.000	1.264	1.260	1.317	1.320	1.330	1.340
	0.125	0.354	0.441	0.656	0.387	0.461	0.660
	0.250	0.330	0.398	0.607	0.314	0.438	0.612
	0.375	0.487	0.413	0.437	0.477	0.452	0.452
	0.500	0.416	0.240	0.110	0.416	0.267	0.143
	0.625	0.533	0.356	0.323	0.505	0.380	0.306
	0.750	0.521	0.328	0.330	0.556	0.332	0.345
	0.875	0.394	0.326	0.487	0.421	0.346	0.520
	1.000	0.480	0.610	0.829	0.522	0.646	0.870
0.4	0.000	1.579	1.409	1.284	1.930	1.700	1.530
	0.125	0.760	0.704	0.773	0.859	0.834	0.933
	0.250	0.443	0.562	0.769	0.512	0.674	0.910
	0.375	0.625	0.624	0.695	0.675	0.762	0.849
	0.500	0.638	0.487	0.378	0.764	0.590	0.453
	0.625	0.670	0.436	0.346	0.766	0.529	0.405
	0.750	0.720	0.499	0.546	0.854	0.606	0.655
	0.875	0.669	0.549	0.733	0.781	0.644	0.880
	1.000	0.627	0.718	1.014	0.770	0.869	1.160
0.5	0.000	1.650	1.356	1.109	1.930	1.570	1.310
	0.125	1.021	0.826	0.776	1.210	1.000	0.952
	0.250	0.712	0.685	0.818	0.830	0.830	0.954
	0.375	0.743	0.729	0.825	0.832	0.881	0.980
	0.500	0.758	0.664	0.657	0.883	0.809	0.784
	0.625	0.736	0.579	0.552	0.860	0.736	0.650
	0.750	0.750	0.604	0.671	0.898	0.750	0.812
	0.875	0.758	0.709	0.888	0.863	0.850	1.070
	1.000	0.808	0.922	1.191	0.938	1.110	1.390
0.6	0.000	1.625	1.275	0.988	1.660	1.320	0.981
	0.125	1.141	0.882	0.791	1.140	0.896	0.759
	0.250	0.885	0.766	0.850	0.860	0.748	0.823
	0.375	0.852	0.791	0.894	0.899	0.800	0.899
	0.500	0.855	0.766	0.822	0.814	0.752	0.826
	0.625	0.818	0.701	0.748	0.803	0.679	0.728
	0.750	0.782	0.695	0.814	0.804	0.680	0.817
	0.875	0.777	0.800	1.017	0.769	0.781	1.000
	1.000	0.861	1.036	1.331	0.820	1.010	1.290

Table 2.6. RAOs of deflection of the floating plate structures under incident regular waves with an angle ($\theta = 90°$) and six wavelengths ($\lambda / L = 0.1$, 0.2, 0.3, 0.4, 0.5 and 0.6) obtained by the present procedure and the experiments

λ / L	Points	Calculation			Experiment		
		Starboard	**Center**	**Port side**	**Starboard**	**Center**	**Port side**
0.1	0.000	0.287	0.082	0.412	0.256	0.061	0.317
	0.125	0.281	0.092	0.423	0.270	0.099	0.355
	0.250	0.281	0.098	0.430	0.247	0.113	0.393
	0.375	0.292	0.090	0.425	0.285	0.090	0.407
	0.500	0.299	0.083	0.419	0.299	0.067	0.372
	0.625	0.292	0.090	0.425	0.300	0.093	0.398
	0.750	0.281	0.098	0.430	0.277	0.119	0.436
	0.875	0.281	0.092	0.423	0.279	0.084	0.401
	1.000	0.287	0.082	0.412	0.293	0.061	0.341
0.2	0.000	0.804	0.253	1.124	0.852	0.247	1.100
	0.125	0.789	0.257	1.132	0.816	0.273	1.140
	0.250	0.786	0.264	1.134	0.830	0.262	1.140
	0.375	0.798	0.267	1.124	0.832	0.276	1.150
	0.500	0.807	0.268	1.117	0.858	0.265	1.130
	0.625	0.798	0.267	1.124	0.860	0.292	1.130
	0.750	0.786	0.264	1.134	0.836	0.281	1.170
	0.875	0.789	0.257	1.132	0.838	0.282	1.160
	1.000	0.804	0.253	1.124	0.839	0.259	1.140
0.3	0.000	1.217	0.444	1.471	-	0.733	-
	0.125	1.199	0.437	1.479	-	0.773	-
	0.250	1.189	0.446	1.490	-	0.863	-
	0.375	1.190	0.462	1.498	-	0.953	-
	0.500	1.192	0.470	1.500	-	0.944	-
	0.625	1.190	0.462	1.498	-	0.897	-
	0.750	1.189	0.446	1.490	-	0.814	-
	0.875	1.199	0.437	1.479	-	0.767	-
	1.000	1.217	0.444	1.471	-	0.857	-
0.4	0.000	1.328	0.623	1.439	1.400	0.654	1.490
	0.125	1.312	0.610	1.444	1.360	0.644	1.500
	0.250	1.301	0.611	1.454	1.350	0.657	1.520
	0.375	1.295	0.619	1.466	1.360	0.684	1.550
	0.500	1.294	0.624	1.471	1.380	0.697	1.540
	0.625	1.295	0.619	1.466	1.390	0.699	1.540
	0.750	1.301	0.611	1.454	1.380	0.676	1.530
	0.875	1.312	0.610	1.444	1.380	0.653	1.500
	1.000	1.328	0.623	1.439	1.380	0.667	1.480
0.5	0.000	1.312	0.746	1.347	1.290	0.745	1.330
	0.125	1.300	0.733	1.346	1.290	0.734	1.360
	0.250	1.291	0.729	1.351	1.290	0.761	1.380
	0.375	1.284	0.730	1.359	1.270	0.775	1.380
	0.500	1.282	0.731	1.363	1.310	0.776	1.390
	0.625	1.284	0.730	1.359	1.300	0.753	1.370
	0.750	1.291	0.729	1.351	1.300	0.755	1.360
	0.875	1.300	0.733	1.346	1.300	0.731	1.330
	1.000	1.312	0.746	1.347	1.300	0.758	1.320
0.6	0.000	1.273	0.822	1.277	1.290	0.845	1.290
	0.125	1.263	0.810	1.273	1.300	0.820	1.290
	0.250	1.255	0.805	1.274	1.280	0.820	1.270
	0.375	1.249	0.803	1.278	1.280	0.820	1.290
	0.500	1.247	0.802	1.280	1.250	0.820	1.270
	0.625	1.249	0.803	1.278	1.270	0.832	1.300
	0.750	1.255	0.805	1.274	1.270	0.807	1.290
	0.875	1.263	0.810	1.273	1.270	0.807	1.290
	1.000	1.273	0.822	1.277	1.270	0.820	1.280

2.4 Closure

In this chapter, a formulation for the hydroelastic analysis of floating plate structures in incident regular waves based on a direct coupling method is presented. The directly coupled equations of motion for the hydroelastic analysis are discretized the finite element method for plate structures and by the boundary element method for fluids and. The capability of the proposed numerical procedure was investigated through comparisons with the experimental results.

Chapter 3. Consideration of Multiple Hinge Connections

It is well known that the use of hinge connections can reduce the hydroelastic responses. That is, bending moment, deflection and strain energy stored in floating plate structures due to waves can be reduced depending on structural and wave parameters [44-52]. However, although the maximum responses are very important in the design of VLFSs, the effect of the number of hinge connections used on the maximum responses has not been studied well [48]. It has also not been well known that the hydroelastic responses could increase due to the use of hinge connections.

The hydroelastic analysis of floating structures with hinge connections or interconnected floating structures with hinges or rotational springs have been studied. In hydroelastic analysis of floating structures using the modal expansion method, hinge deflection modes have been used to model hinge connections [45-51, 54, 55]. The hinge deflection modes can be obtained analytically for simple problems [45-49] and numerically for complicated problems [50, 51, 54, 55]. The conditions for hinge connections can be enforced by adopting the penalty technique [52]. However, the numerical procedures have not been verified by experimental studies.

In order to solve the hydroelastic problems of floating plate structures with multiple hinge connections, the direct coupling method is employed and a complete condensation method is derived for modeling hinge connections, in which the rotational degrees of freedom (DOFs) of the plate finite elements are released. Hinge deflection modes are not used explicitly. The proposed formulation is mathematically complete because structural mass and stiffness matrices and fluid-structure interaction matrix are consistently condensed. To assess the validity of the proposed numerical procedure, the numerical calculations are compared with the experimental results.

The most important feature of the proposed hinge model is its modeling capability, which is shown in numerical examples: floating plate problems with 1- and 2-directional multiple hinge connections. Thus, it is able to easily deal with the hydroelastic responses of floating plate structures with arbitrarily positioned multiple hinge connections. The numerical analyses show the effect of the number of hinge connections used on the maximum bending moment and deflection of the floating plate structures according to the aspect ratio, bending stiffness and incident wavelength.

3.1 Modeling of Hinge Connections

Figure 3.1 shows the problem description of a floating plate structure with hinge connections in incident regular waves. The interaction between the floating plate structure and an incident regular wave is handled by the direct coupling method. For the finite element model of plate structures, the MITC4 plate element is employed. On the other hand, for the boundary element model of fluid, a 4-node quadrilateral boundary element is used. Thus, in the discretized coupled equation (2.22), the Nodal DOFs vectors for unknown structural displacement $\hat{\mathbf{u}}$ and total water pressure $\hat{\mathbf{p}}$ of the elements is as follows

$$\hat{\mathbf{u}} = \left[u_3^1 \quad \theta_{x_1}^1 \quad \theta_{x_2}^1 \quad u_3^2 \quad \theta_{x_1}^2 \quad \theta_{x_2}^2 \quad u_3^3 \quad \theta_{x_1}^3 \quad \theta_{x_2}^3 \quad u_3^4 \quad \theta_{x_1}^4 \quad \theta_{x_2}^4 \right], \tag{3.1}$$

$$\hat{\mathbf{p}} = \left[p^1 \quad p^2 \quad p^3 \quad p^4 \right], \tag{3.2}$$

in which u_3^1, $\theta_{x_1}^1$ and $\theta_{x_2}^1$ are the one translational and two rotational DOFs at the plate element local node 1, and p^1 is the pressure DOF at the boundary element local node 1.

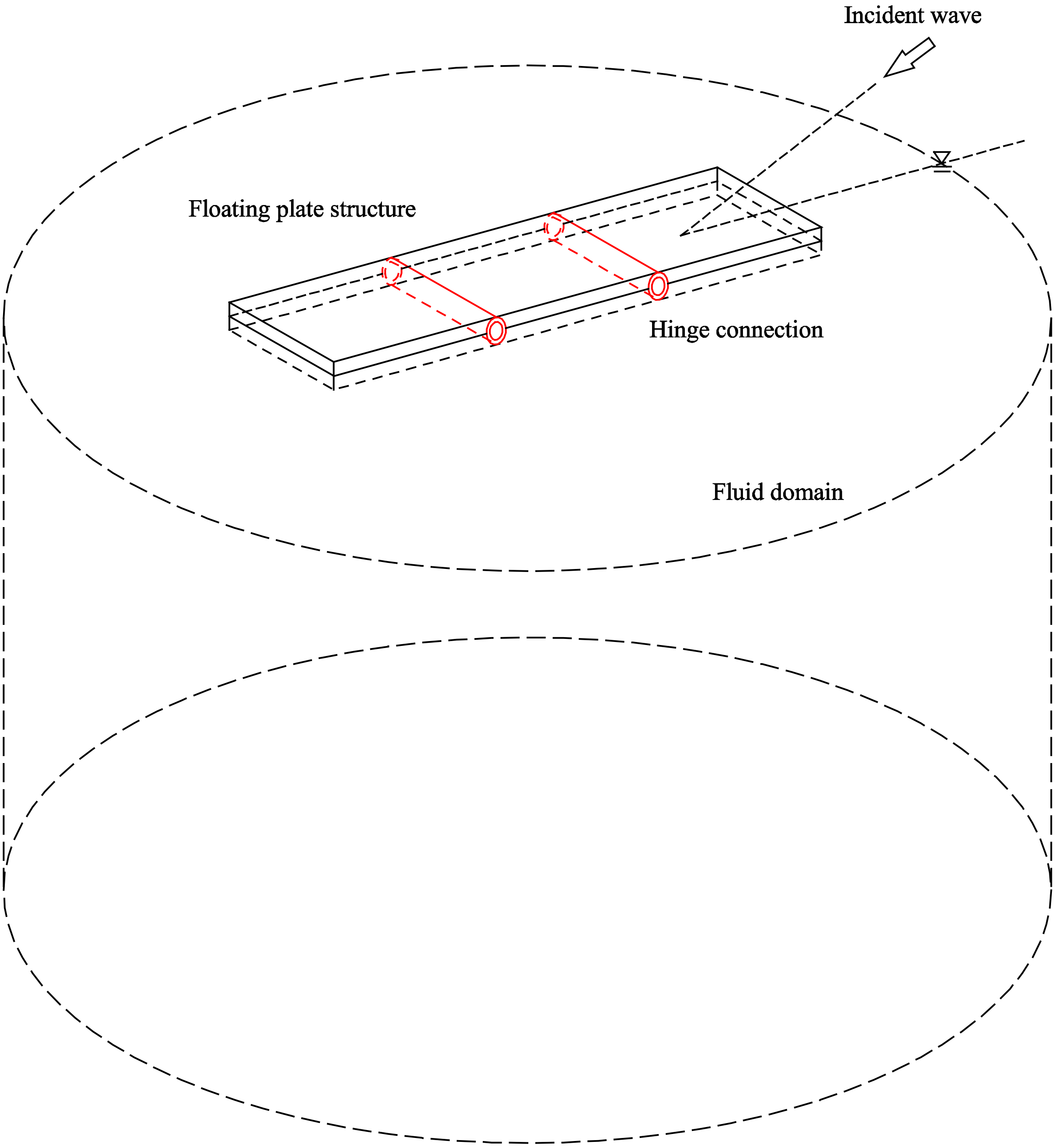

Figure 3.1. A floating plate structure with multiple hinge connections

Since the bending moments are zero at hinge connections, they can be modeled by releasing the rotational DOFs associated with the bending moment at the element local nodes. In static analysis, a stiffness matrix is condensed to release specific DOFs [67]. This technique is named as static condensation. In order to release DOFs in dynamic analysis, however, the mass matrix also need to be condensed through the dynamic condensation technique [79]. Similar to the dynamic condensation procedures, the rotational DOFs are released by condensing structural mass and stiffness matrices, and fluid-structure interaction matrix in Equation (2.22).

In order to condense the rotational DOFs, the matrix is partitioned

$$\begin{bmatrix} -\omega^2\mathbf{S}_M^{aa}+\mathbf{S}_K^{aa} & -\omega^2\mathbf{S}_M^{ac}+\mathbf{S}_K^{ac} & -\mathbf{C}_{up}^{ap} \\ -\omega^2\mathbf{S}_M^{ca}+\mathbf{S}_K^{ca} & -\omega^2\mathbf{S}_M^{cc}+\mathbf{S}_K^{cc} & -\mathbf{C}_{up}^{cp} \\ -\mathbf{C}_{up}^{ap\,T} & -\mathbf{C}_{up}^{cp\,T} & -\mathbf{F}_M-\mathbf{F}_G \end{bmatrix} \begin{bmatrix} \hat{\mathbf{u}}_a \\ \hat{\mathbf{u}}_c \\ \hat{\mathbf{p}} \end{bmatrix} = \begin{bmatrix} \mathbf{0} \\ \mathbf{0} \\ \hat{\mathbf{R}}_{\mathbf{I}} \end{bmatrix}, \tag{3.3}$$

and the matrix in Equation (3.3) is rearranged as follows

$$\begin{bmatrix} -\omega^2\mathbf{S}_M^{aa}+\mathbf{S}_K^{aa} & -\mathbf{C}_{up}^{ap} & -\omega^2\mathbf{S}_M^{ac}+\mathbf{S}_K^{ac} \\ -\mathbf{C}_{up}^{ap\,T} & -\mathbf{F}_M-\mathbf{F}_G & -\mathbf{C}_{up}^{cp\,T} \\ -\omega^2\mathbf{S}_M^{ca}+\mathbf{S}_K^{ca} & -\mathbf{C}_{up}^{cp} & -\omega^2\mathbf{S}_M^{cc}+\mathbf{S}_K^{cc} \end{bmatrix} \begin{bmatrix} \hat{\mathbf{u}}_a \\ \hat{\mathbf{p}} \\ \hat{\mathbf{u}}_c \end{bmatrix} = \begin{bmatrix} \mathbf{0} \\ \hat{\mathbf{R}}_{\mathbf{I}} \\ \mathbf{0} \end{bmatrix}, \tag{3.4}$$

where $\hat{\mathbf{u}}_a$ and $\hat{\mathbf{u}}_c$ are the displacement vectors to be retained and condensed, respectively. Therefore, $\hat{\mathbf{u}}_c$ is the vector of the rotational DOFs corresponding to the hinge connections as shown in **Figure 3.2**.

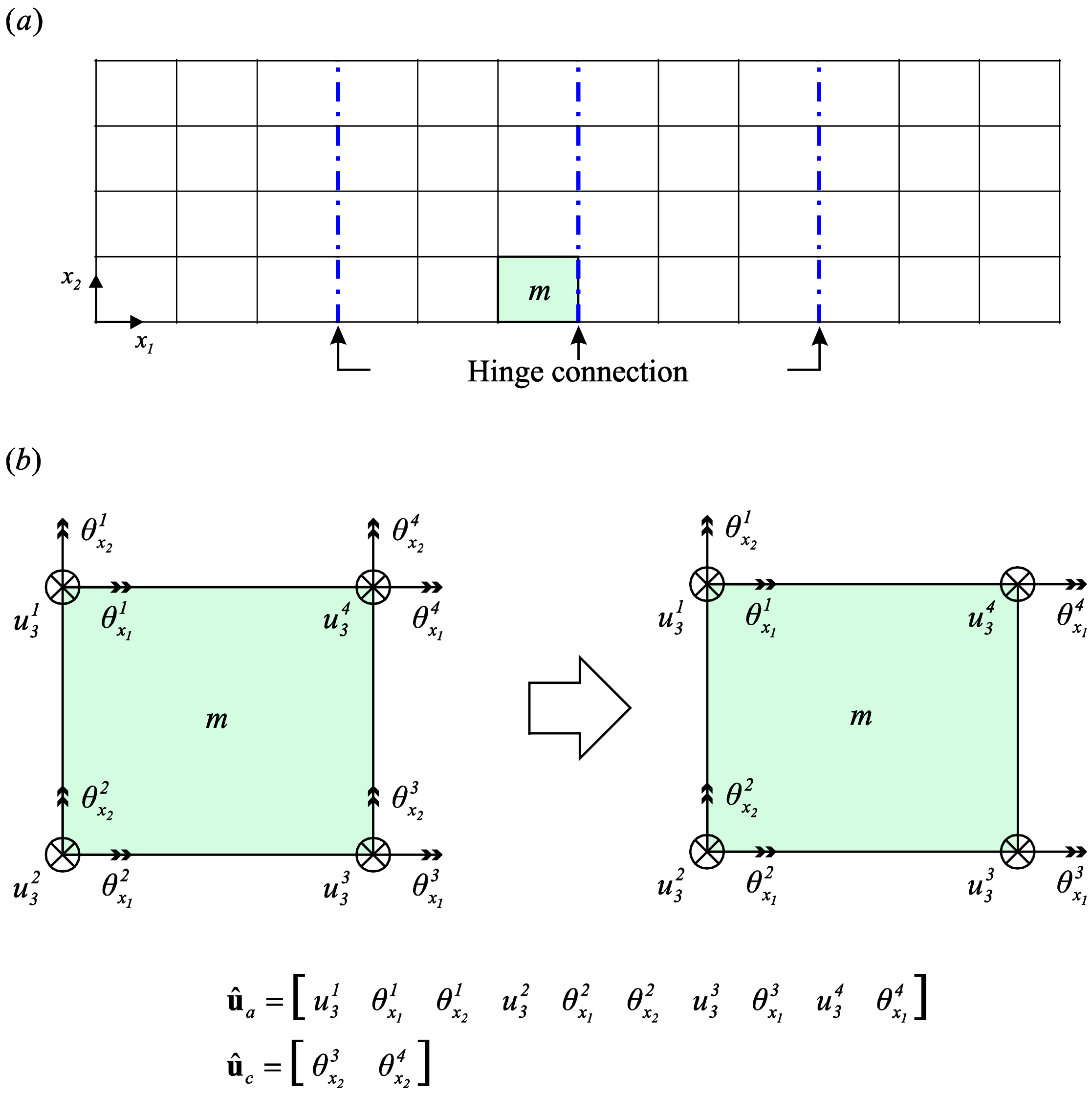

Figure 3.2. Nodal DOFs of a MITC4 plate element: (a) a floating plate structure with three hinge connections, (b) retained and condensed nodal DOFs.

From the third row in Equation (3.4), the following equation can be obtained:

$$\left(-\omega^2 \mathbf{S}_M^{ca} + \mathbf{S}_K^{ca}\right)\hat{\mathbf{u}}_a - \mathbf{C}_{up}^{cp}\,\hat{\mathbf{p}} + \left(-\omega^2 \mathbf{S}_M^{cc} + \mathbf{S}_K^{cc}\right)\hat{\mathbf{u}}_c = \mathbf{0}\,, \tag{3.5}$$

and

$$\hat{\mathbf{u}}_c = -\left(-\omega^2 \mathbf{S}_M^{cc} + \mathbf{S}_K^{cc}\right)^{-1}\left(-\omega^2 \mathbf{S}_M^{ca} + \mathbf{S}_K^{ca}\right)\hat{\mathbf{u}}_a + \left(-\omega^2 \mathbf{S}_M^{cc} + \mathbf{S}_K^{cc}\right)^{-1}\mathbf{C}_{up}^{cp}\,\hat{\mathbf{p}}\,. \tag{3.6}$$

Let us transform Equation (3.6) into a matrix form as follows

$$\begin{bmatrix} \hat{\mathbf{u}}_a \\ \hat{\mathbf{p}} \\ \hat{\mathbf{u}}_c \end{bmatrix} = [\mathbf{T}] \begin{bmatrix} \hat{\mathbf{u}}_a \\ \hat{\mathbf{p}} \end{bmatrix}, \tag{3.7}$$

where

$$[\mathbf{T}] = \begin{bmatrix} \mathbf{I}_a & \mathbf{0} \\ \mathbf{0} & \mathbf{I}_p \\ -\left(-\omega^2 \mathbf{S}_M^{cc} + \mathbf{S}_K^{cc}\right)^{-1}\left(-\omega^2 \mathbf{S}_M^{ca} + \mathbf{S}_K^{ca}\right) & \left(-\omega^2 \mathbf{S}_M^{cc} + \mathbf{S}_K^{cc}\right)^{-1} \mathbf{C}_{up}^{cp} \end{bmatrix}, \tag{3.8}$$

in which $\mathbf{I}_a$ and $\mathbf{I}_p$ are the identity matrices corresponding to $\hat{\mathbf{u}}_a$ and $\hat{\mathbf{p}}$, respectively.

By substituting Equation (3.7) into Equation (3.4) and premultiplying $[\mathbf{T}]^T$:

$$[\mathbf{T}]^T \begin{bmatrix} -\omega^2 \mathbf{S}_M^{aa} + \mathbf{S}_K^{aa} & -\mathbf{C}_{up}^{ap} & -\omega^2 \mathbf{S}_M^{ac} + \mathbf{S}_K^{ac} \\ -\mathbf{C}_{up}^{ap\,T} & -\mathbf{F}_M - \mathbf{F}_G & -\mathbf{C}_{up}^{cp\,T} \\ -\omega^2 \mathbf{S}_M^{ca} + \mathbf{S}_K^{ca} & -\mathbf{C}_{up}^{cp} & -\omega^2 \mathbf{S}_M^{cc} + \mathbf{S}_K^{cc} \end{bmatrix} [\mathbf{T}] \begin{bmatrix} \hat{\mathbf{u}}_a \\ \hat{\mathbf{p}} \end{bmatrix} = [\mathbf{T}]^T \begin{bmatrix} \mathbf{0} \\ \hat{\mathbf{R}}_\mathbf{I} \\ \mathbf{0} \end{bmatrix}, \tag{3.9}$$

the condensed matrix form is finally obtained:

$$\begin{bmatrix} \mathbf{S}^{aa} & \mathbf{C}^{ap} \\ \mathbf{C}^{apT} & \mathbf{F}^{pp} \end{bmatrix} \begin{bmatrix} \hat{\mathbf{u}}_a \\ \hat{\mathbf{p}} \end{bmatrix} = \begin{bmatrix} \mathbf{0} \\ \hat{\mathbf{R}}_\mathbf{I} \end{bmatrix}, \tag{3.10}$$

where

$$\mathbf{S}^{aa} = -\omega^2 \mathbf{S}_M^{aa} + \mathbf{S}_K^{aa} - \left(-\omega^2 \mathbf{S}_M^{ac} + \mathbf{S}_K^{ac}\right)\left(-\omega^2 \mathbf{S}_M^{cc} + \mathbf{S}_K^{cc}\right)^{-1}\left(-\omega^2 \mathbf{S}_M^{ca} + \mathbf{S}_K^{ca}\right), \tag{3.11a}$$

$$\mathbf{C}^{ap} = -\mathbf{C}_{up}^{ap} + \left(-\omega^2 \mathbf{S}_M^{ac} + \mathbf{S}_K^{ac}\right)\left(-\omega^2 \mathbf{S}_M^{cc} + \mathbf{S}_K^{cc}\right)^{-1} \mathbf{C}_{up}^{cp}, \tag{3.11b}$$

$$\mathbf{F}^{pp} = -\mathbf{F}_M - \mathbf{F}_G - \mathbf{C}_{up}^{cp\,T}\left(-\omega^2 \mathbf{S}_M^{cc} + \mathbf{S}_K^{cc}\right)^{-1} \mathbf{C}_{up}^{cp}. \tag{3.11c}$$

By solving Equation (3.10), the hydroelastic responses of floating plate structures with multiple hinge connections in incident regular waves are directly calculated.

3.2 Verification and Modeling Capability

The proposed numerical procedure can be easily applied to calculate the hydroelastic response of floating plates with arbitrarily positioned multiple hinge connections. To verify the proposed numerical procedure, we compare the numerical results with the experimental and previous numerical results. Then, to demonstrate the modeling capability of the proposed numerical procedure, the hydroelastic analysis of floating plate structures with 1- and 2- directional multiple hinge connections are conducted.

Three dimensionless parameters are considered: aspect ratio L_r (the ratio of the structural length to the width), dimensionless wavelength α the ratio of the incident wavelength λ to the structural length) and dimensionless bending stiffness S (the ratio of the longitudinal bending stiffness to the hydrostatic restoring force)

$$L_r = \frac{L}{B}, \quad \alpha = \frac{\lambda}{L}, \text{ and } \quad S = \frac{EI}{\rho_w g L^5}, \tag{3.12}$$

in which E and I denote Young's modulus and the second moment of area on the x_2 - axis ($I = BH^3/12$).

In addition, two response amplitude operators (RAOs) of the dimensionless bending moment $\overline{M}_{x_2x_2}$ and deflection $\overline{u}_3$ are estimated:

$$\overline{M}_{x_2x_2} = \frac{\left|M_{x_2x_2}\right|}{\rho_w g L^2} \quad \text{and} \quad \overline{u}_3 = \frac{\left|\tilde{u}_3\right|}{a}, \tag{3.13}$$

where $M_{x_2x_2}$ is the RAO of the bending moment per unit width.

3.2.1 Comparison with Experimental Results

In order to verify the proposed numerical procedure, present results are compared with hydroelastic experimental results of floating plate structures conducted by Cho [80]. **Table 3.1** presents the details of the floating plate structures used for the hydroelastic experiments.

Table 3.1. Details of the floating plate model for hydroelastic experiments.

Parameter	Value
Length (L)	$3m$
Width (B)	$0.6m$
Thickness (H)	$0.04m$
Draft (d)	$0.011m$
Bending stiffness (EI)	$30.385Nm^2$
Dimensionless bending stiffness (S)	1.244×10^{-5}

Figure 3.3 illustrates the experimental setup in the wave tank [80]. In order to measure the wave frequency and amplitude, one wave probe was installed. The heave motions of the floating plate structures were measured through four motion capture cameras with IR reflective markers. **Figure 3.4** shows the positions of the IR reflective markers attached on the floating plates. The drift of plate structures due to waves was prevented by mooring the plates with four strings, see **Figures 3.3**. Since the strings should prevent the drift without restraining the heave motions, small tension was introduced so that the strings were horizontally connected to the plate structures. That is, the connection angle between strings and plate structures is almost $180°$, see **Figure 3.3(c)**.

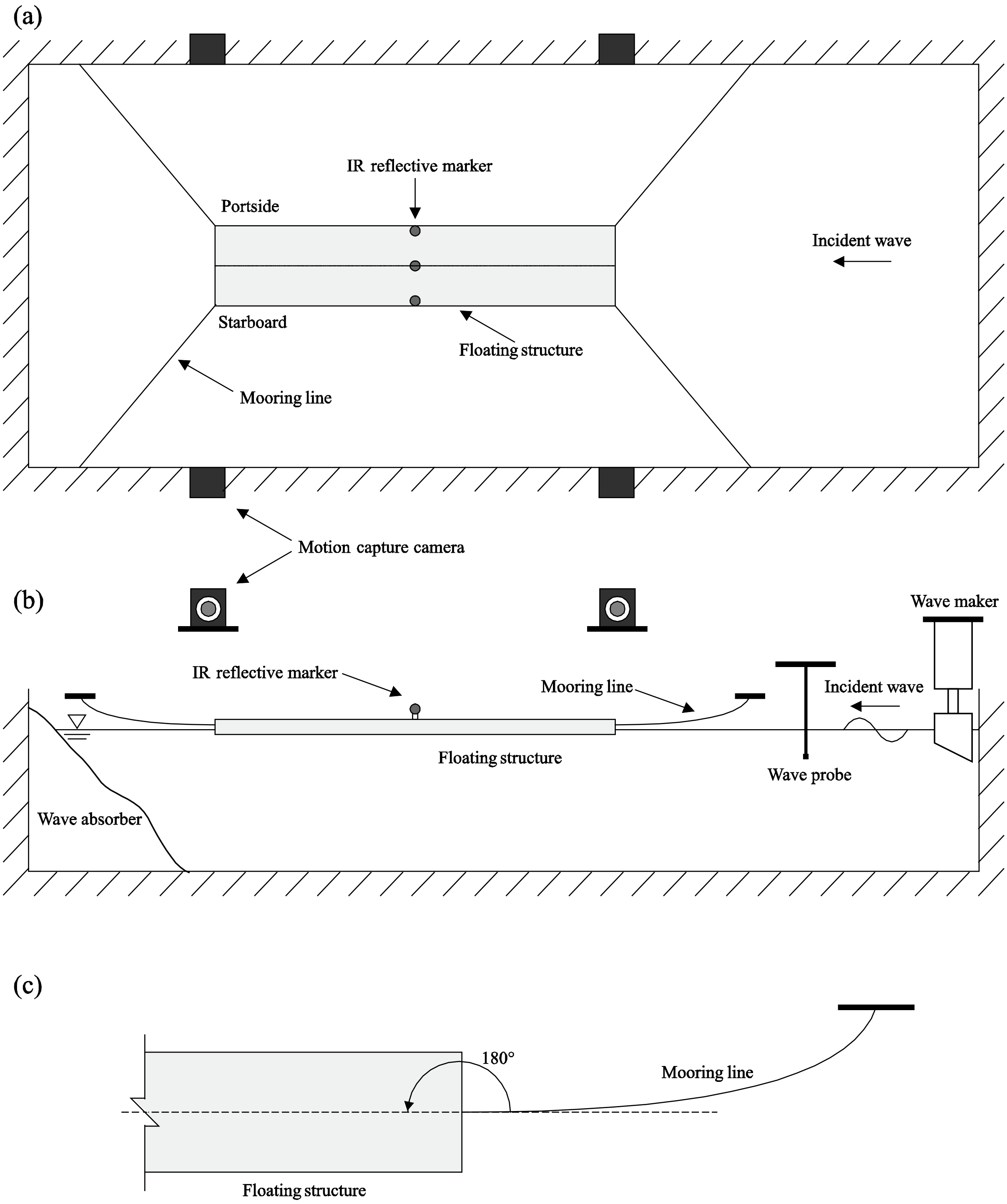

Figure 3.3. A schematic of the experimental setup: (a) Top view, (b) Front view, (c) Mooring lines.

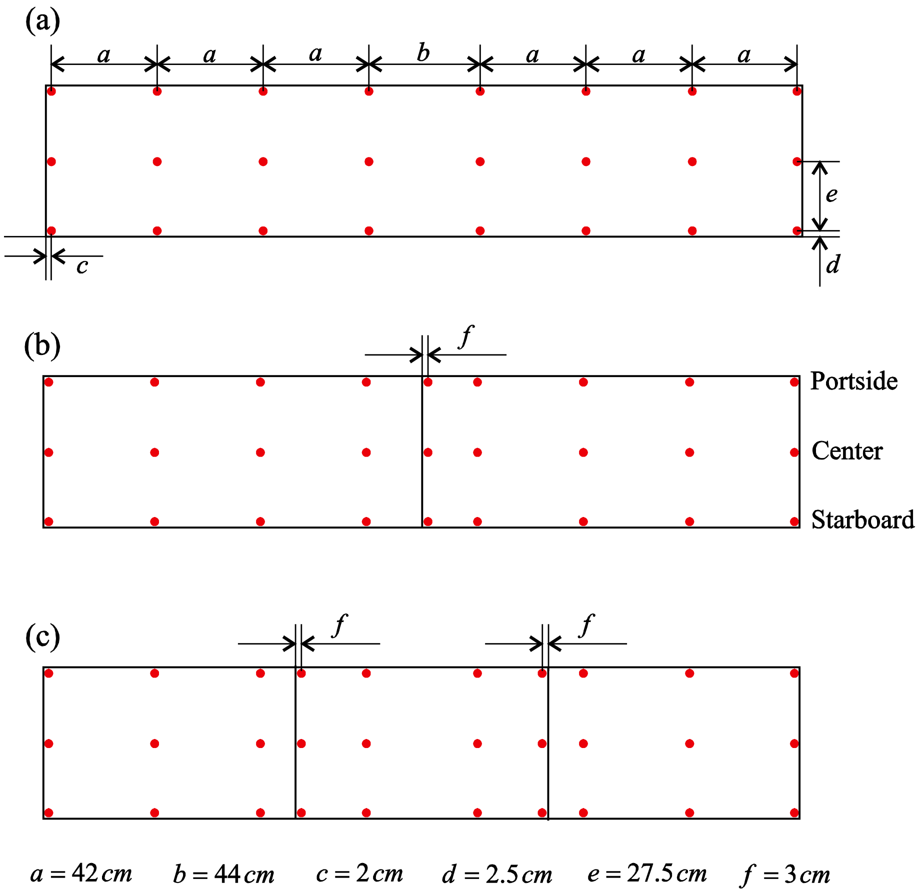

Figure 3.4. Positions of the IR reflective markers on floating structures: (a) no hinge, (b) 1 hinge, and (c) 2 hinges.

In the hydroelastic experiments, zero to two hinge connections in the floating plate structures subjected to regular waves ($a = 0.01m$ and $\alpha = 0.6$) with four different angles ($\theta = 0°$, $30°$, $60°$ and $90°$) were considered. The water depth is $1.5m$. Note that incident wave conditions ($2a/h = 0.0133$ and $h/\lambda = 0.8333$) are included in the range of the linear wave theory in deep water ($2a/h < 0.1$ and $h/\lambda = 0.5$) [81].

Figures. 3.5 and 3.6 show the comparisons between experimental and numerical results for RAOs of deflection along the longitudinal lines of the plates. For the numerical results, the structural and fluid domains are modeled by the 60×12 mesh of the MITC4 plate elements and the 60×12 mesh of the boundary elements, respectively. The numerical results agree well with those obtained by experimental tests.

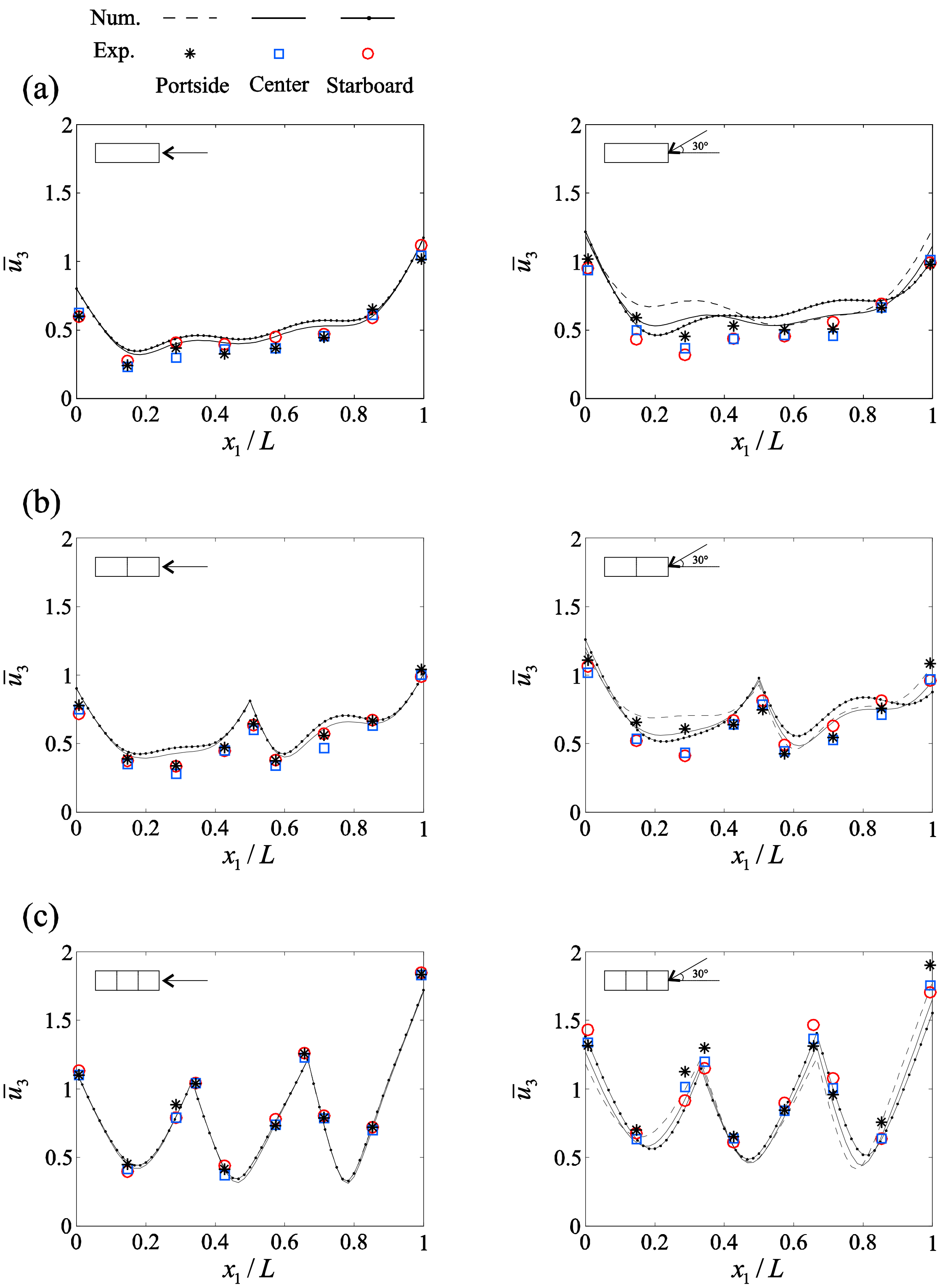

Figure 3.5. RAOs of deflection of the floating plates with multiple hinge connections with $\alpha = 0.6$ for two wave angles ($\theta = 0°$ and $30°$) : (a) no hinge, (b) 1 hinge, and (c) 2 hinges.

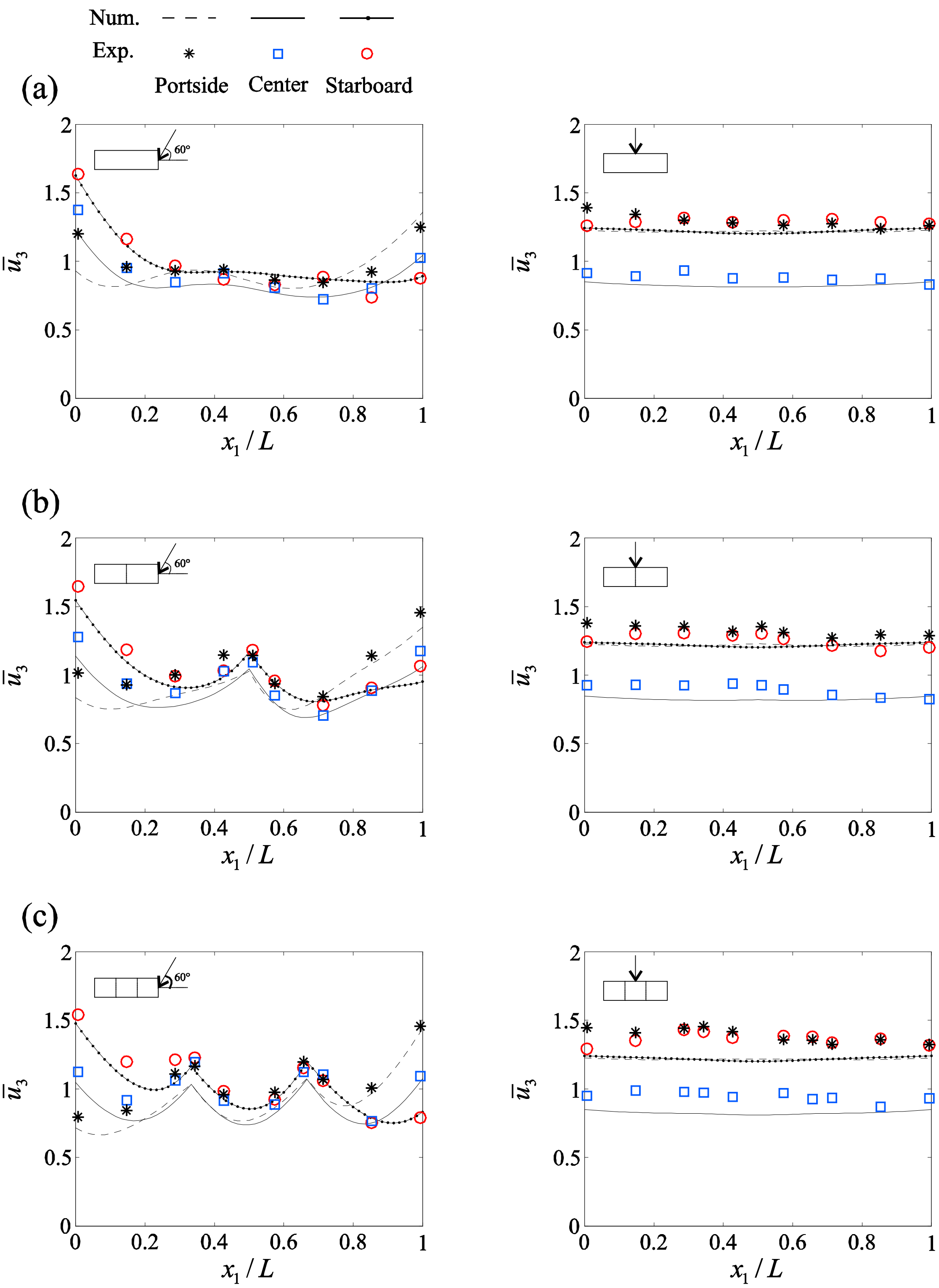

Figure 3.6. RAOs of deflection of the floating plates with multiple hinge connections with $\alpha = 0.6$ for two wave angles ($\theta = 60°$ and $90°$) : (a) no hinge, (b) 1 hinge, and (c) 2 hinges.

3.2.2 Comparison with Previous Numerical Results

In hydroelastic analysis of floating plate structures with multiple hinge connections, the proposed numerical procedure is based on the direct coupling formulation in contrast to previous studies. The hydroelastic responses of a floating plate structure with a hinge connection are calculate, and then the results are compared with those obtained by S. Fu et al. [50]. A scaled model of the Mega-Float ($L = 300m$, $B = 60m$, $H = 2m$, $d = 0.5m$, and $EI = 4.77 \times 10^{11} Nm^2$) is considered and the water depth is $58.5m$ [15]. They used the 150×30 mesh of the plate and boundary elements for modeling the structural and fluid domains, respectively.

The floating plate structure is modeled by the 60×12 mesh of the plate and boundary elements. **Figure 3.7** shows $\bar{u}_3$ and $\overline{M}_{x_2x_2}$ along the longitudinal centerline of the plate with a hinge connection. The numerical results are in good agreement with those obtained by S. Fu et al., thereby confirming the validity of the proposed condensation method for modeling hinge connections.

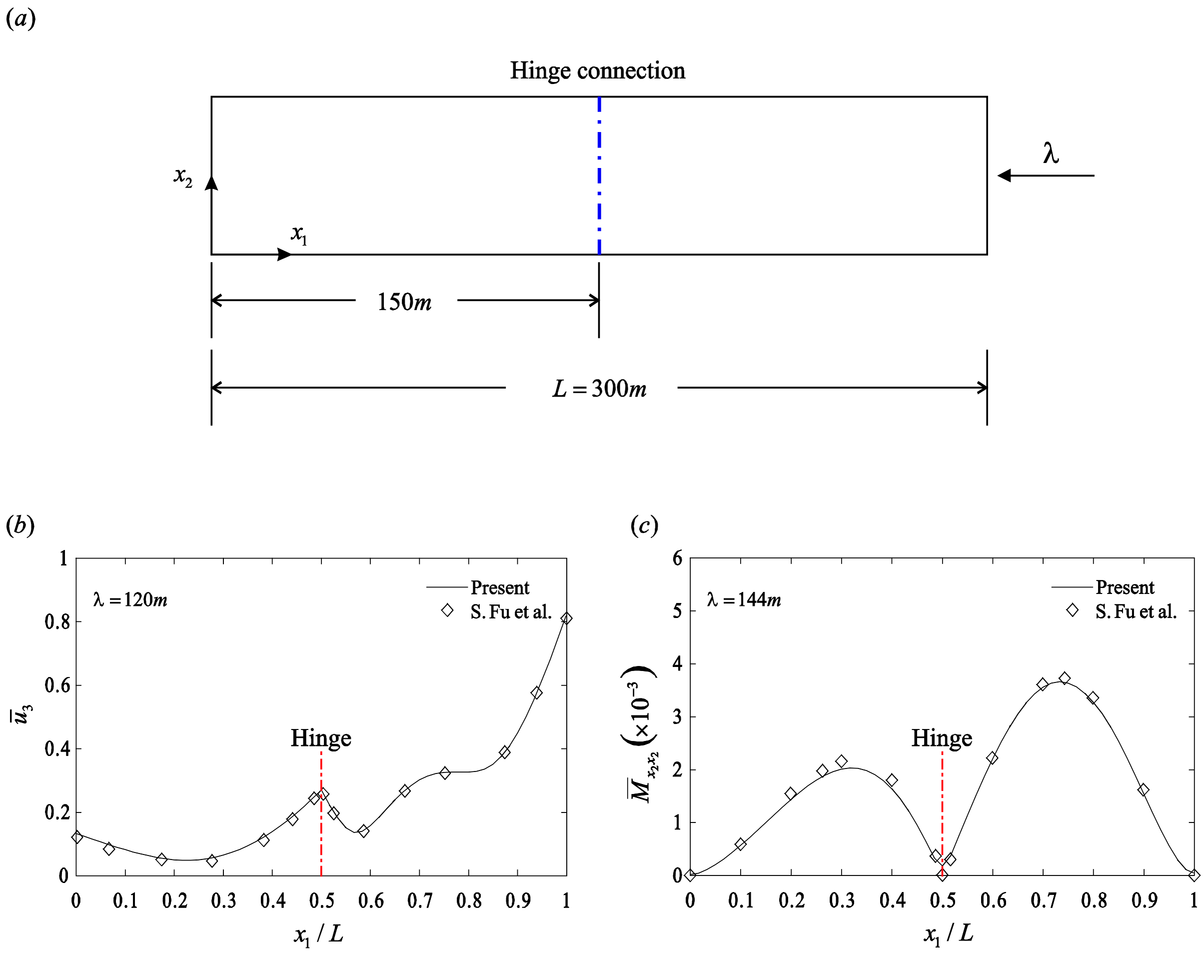

Figure 3.7. Hydroelastic responses along the longitudinal centerline: (a) Problem description, (b) RAOs of deflection for $\lambda / L = 0.4$, (c) RAOs of dimensionless bending moment for $\lambda / L = 0.48$

3.2.3 Numerical Examples

In this section, the hydroelastic responses of floating plate structures with 1- and 2-directional multiple hinge connections are presented. The numerical examples demonstrate the modeling capability of the proposed numerical procedure**. Figure 3.8** shows the description of the floating plate structures ($S = 3.04 \times 10^{-5}$) with 1- and 2-directional multiple hinge connections under a regular wave of $\alpha = 0.6$**.** Hinge connections are uniformly positioned.

First, the hydroelastic analysis of the floating plate structures ($L_r = 5.0$) with 1-directional multiple hinge connections in a head sea ($\theta = 0°$) is performed as shown in **Figure 3.8(a)**. Zero to three hinge connections are considered and 60×12 mesh is used to model the floating plate. The resulting RAOs of deflection are presented in **Figure 3.9**. **Figure 3.10** shows the RAOs of dimensionless bending moment and the RAOs of deflection along the longitudinal centerline of the floating plate structures.

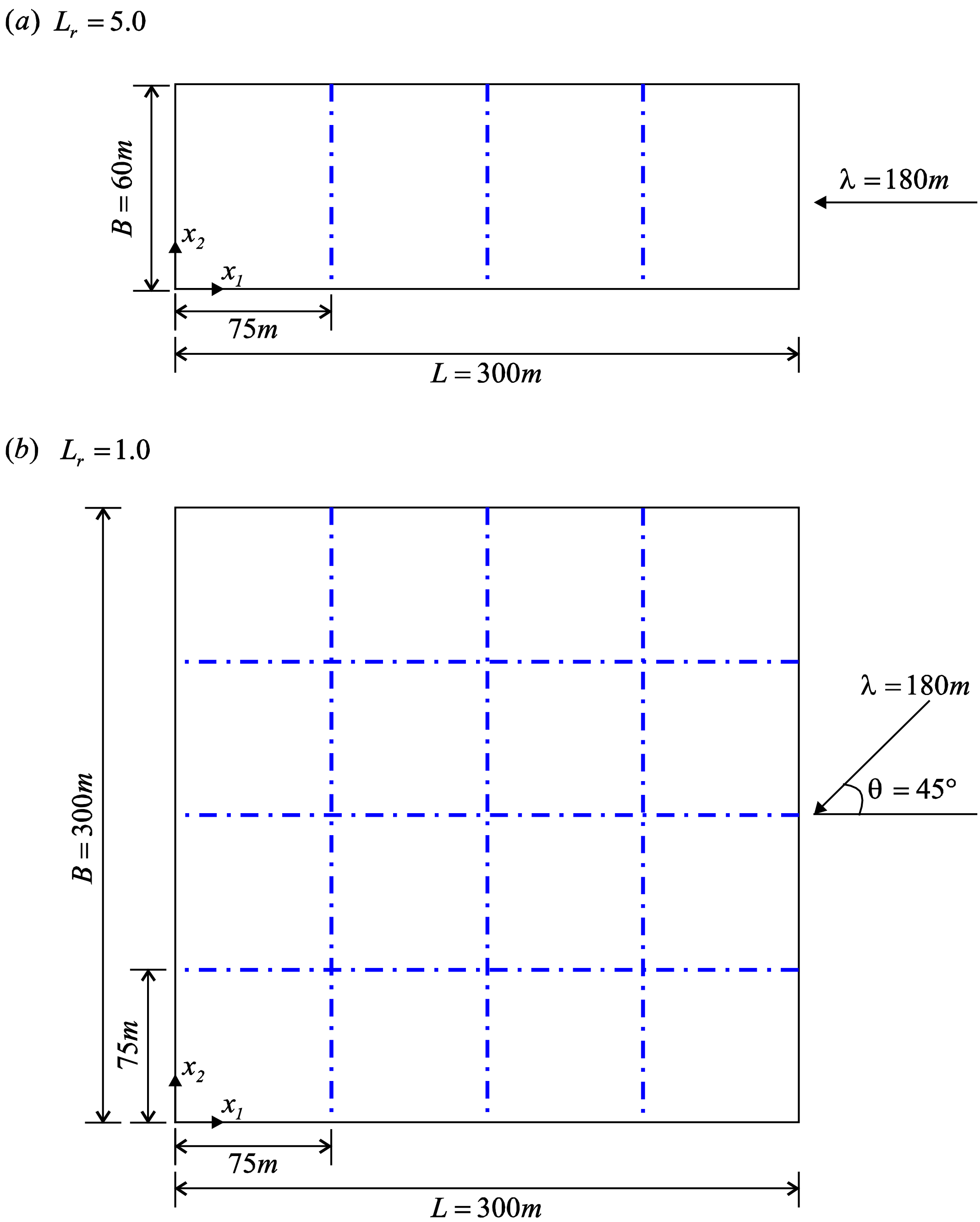

Figure 3.8. Floating plate problems with (a) 1- and (b) 2-directional multiple hinge connections under an incident regular wave.

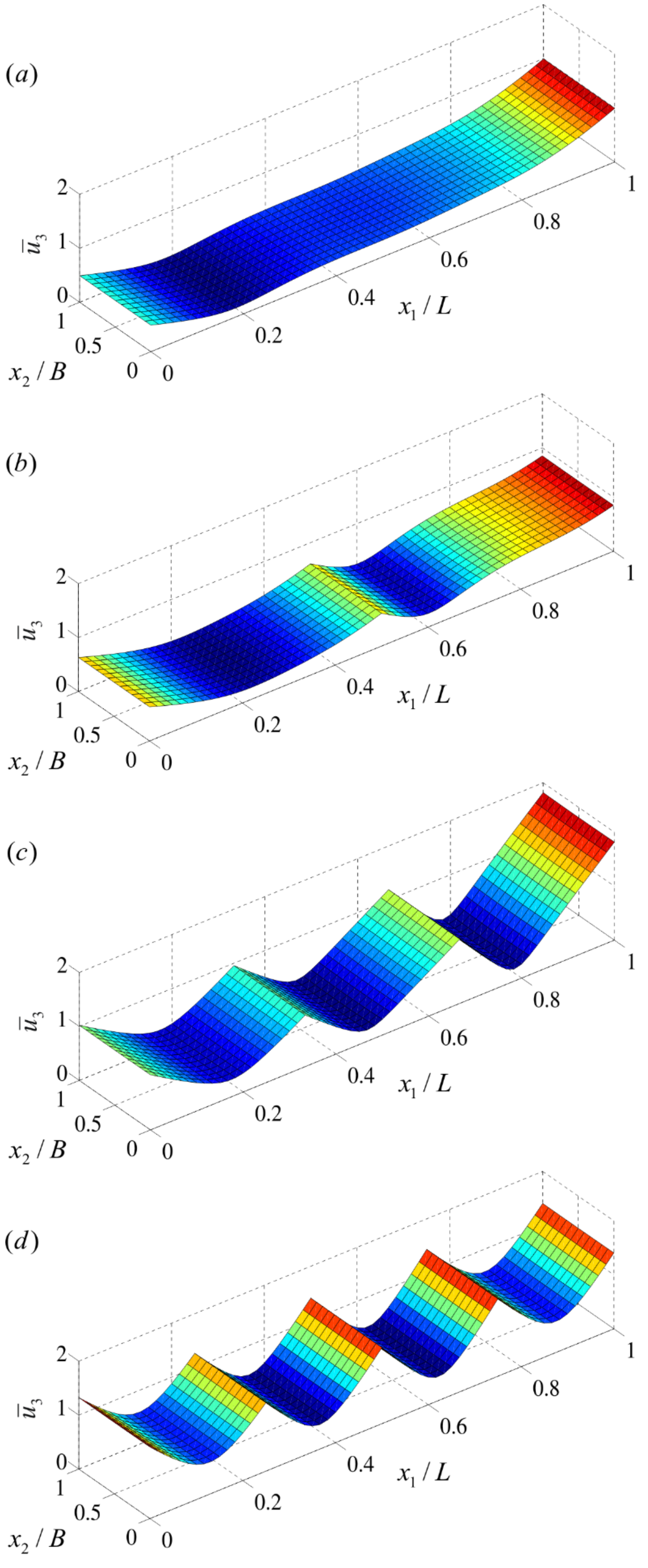

Figure 3.9. RAOs of deflection of the floating plate structures with 1-directional multiple hinge connections in a head sea: (a) no hinge, (b) 1 hinge, (c) 2 hinges, and (d) 3 hinges.

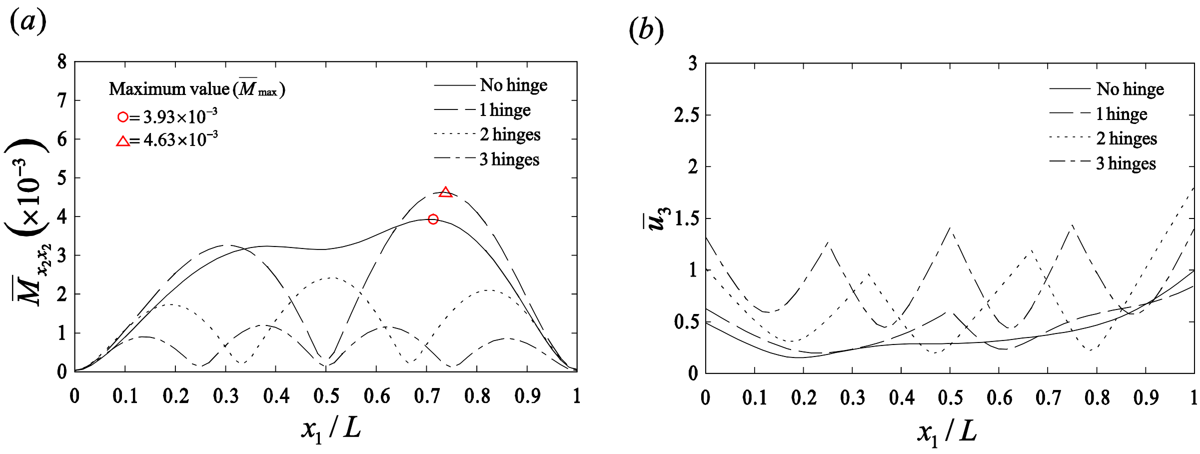

Figure 3.10. Hydroelastic responses along the longitudinal centerline: (a) RAOs of dimensionless bending moment, (b) RAOs of deflection.

It is obvious that the hydroelastic responses are highly affected by the number of hinge connections used. In general, the bending moment decreases in the floating plate structures as the number of hinge connections increases. Each plate partitioned by the hinge connections has the maximum moment around its center. It is important to note that the maximum bending moment can be larger for floating plates with more hinge connections. For example, the maximum bending moment of the floating plate structure with one hinge connection ($\overline{M}_{\max} = 4.63\times10^{-3}$) is larger than that of the floating plate without any hinge connections ($\overline{M}_{\max} = 3.93\times10^{-3}$) as shown in **Figure 3.10(a)**. That is, the use of hinge connections is not always beneficial in reducing the maximum bending moment. As the number of hinge connections increases, the deflections in the floating plates increase in general (see **Figure 3.10(b)**). The deflections have peaks at hinge connections.

Then, the hydroelastic analysis of the floating plate structures ($L_r = 1.0$) with 2-directional multiple hinge connections under an incident regular wave ($\theta = 45°$) is perform, see **Figure 3.8(b)**. The four configurations of 2-directional hinge connections are considered: no hinge, 1×1 hinges, 2×2 hinges and 3×3 hinges. In the numerical example, the floating plate models are discretized by 60×60 mesh.

Figure 3.11 shows the RAOs of deflection of the floating plates. In **Figure 3.12**, the RAOs of the dimensionless bending moment and deflection are plotted along the three longitudinal lines ($x_2/B = 0.0$, 0.5 and 1.0). The basic tendency of RAOs is similar to the results of the floating plates with 1-directional multiple hinge connections. As expected, the larger response is obtained along the starboard side ($x_2/B = 1.0$) rather than along the centerline and port side due to the effect of wave direction.

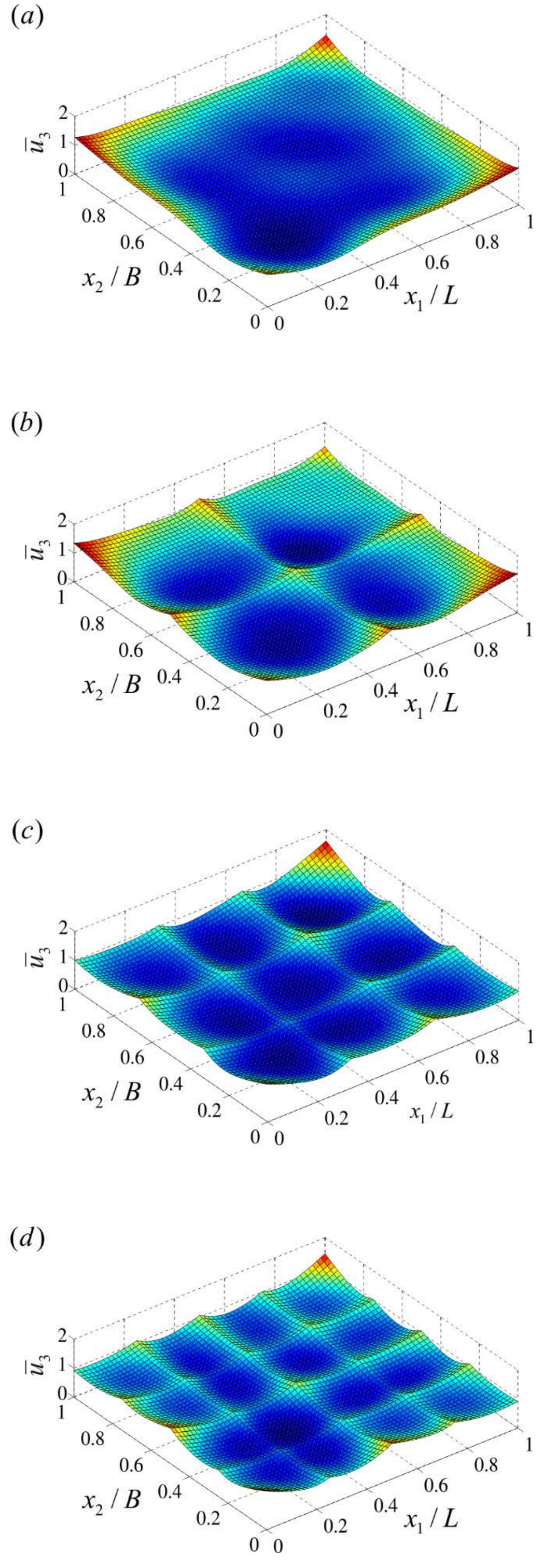

Figure 3.11. RAOs of deflection of the floating plate structures with 2-directional multiple hinge connections under an oblique wave: (a) no hinge, (b) 1 hinge, (c) 2 hinges, and (d) 3 hinges.

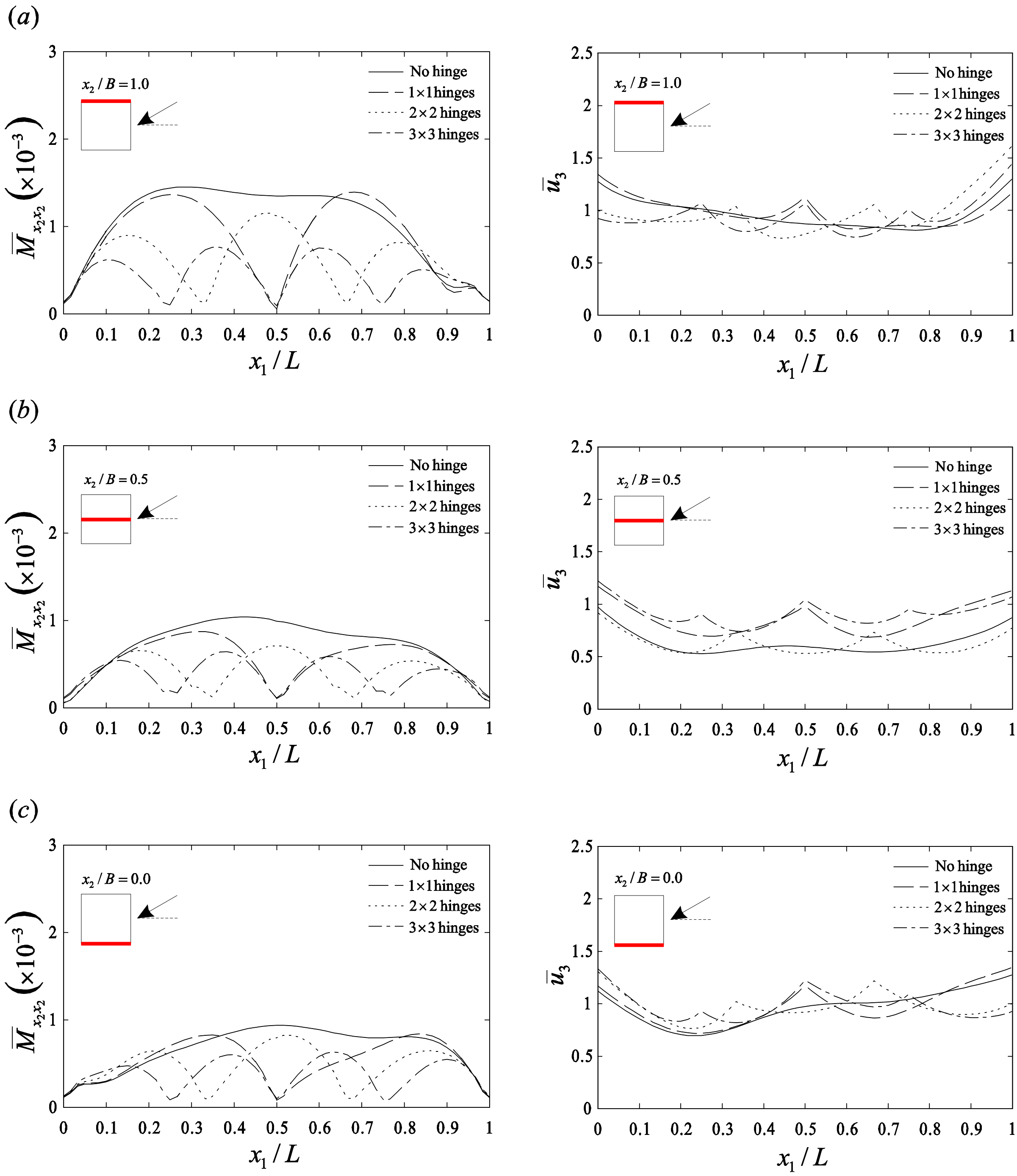

Figure 3.12. Hydroelastic responses along the longitudinal (a) starboard side, (b) centerline, and (c) port side.

3.3 Effect of Multiple Hinge Connections

To investigate the effect of multiple hinge connections, numerical experiments are conducted for the floating plate structures with 1-directional multiple hinge connections under several structural and wave conditions. The maximum value of hydroelastic responses are numerically calculated in the floating plate structures with an increasing number of hinge connections.

In these numerical analyses, zero to three hinge connections are considered in the floating plate structures according to three dimensionless bending stiffnesses ($S = 3.04 \times 10^{-4}$, 3.04×10^{-5}, and 3.04×10^{-6}) and two aspect ratios ($L_r = 1.0$ and 5.0). Note that the range of dimensionless bending stiffness is chosen by referring to the previous experimental and numerical studies. The hinge connections are uniformly positioned in the floating plates as shown in **Figure 3.13**. The structures are subjected to an incident wave with four angles ($\theta = 0°$, $30°$, $45°$, and $60°$) and seven different wavelengths ($\alpha = 0.2$, 0.4, 0.6, 0.8, 1.0, 1.2, and 1.4). The water depth is assumed to be infinite.

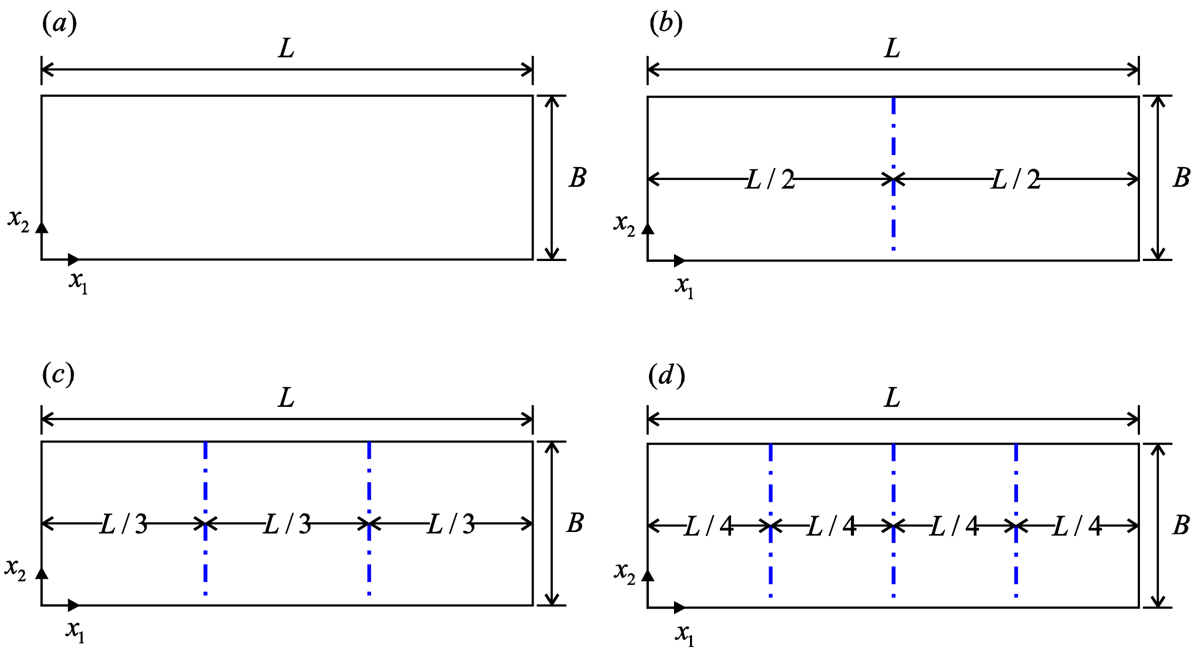

Figure 3.13. Floating plate problems with 1-directional multiple hinge connections: (a) no hinge, (b) 1 hinge, (c) 2 hinges, (d) 3 hinges

The floating plates are modeled by the plate and boundary elements with 60×60 mesh for $L/B = 1$ and with 60×12 mesh for $L/B = 5$. In order to choose appropriate meshes, the convergence study for the maximum hydroelastic responses were carried out for the smallest wavelength ratio considered ($\alpha = 0.2$). The errors in the maximum hydroelastic responses for the meshes chosen are less than 1% compared to well-converged solutions.

Note that, although the hydroelastic responses were calculated for many different cases considering various bending stiffnesses, aspect ratios, wave directions and the configurations of the hinge connections, here the results of some selected cases only presented.

3.3.1 Effects on the Maximum Bending Moment

The maximum bending moment is very important in the cross-sectional design of VLFSs. To investigate the effect of the number of hinge connections on the maximum bending moment, the RAO of the dimensionless maximum bending moment $\overline{M}_{\max}$ (the maximum value of $\overline{M}_{x_2x_2}$ in the entire floating plate structure) is used.

Figure 3.14 ~ 3.17 show $\overline{M}_{\max}$ for the floating plate structures with two different aspect ratios ($L_r = 1.0$ and 5.0) depending on dimensionless bending stiffness, wavelength, and wave angle. In general, as the number of hinge connections increases, the maximum bending moment decreases. Comparing **Figure 3.14(a)** with **Figure 3.14(c)**, it is found that the reductions in the maximum bending moment are larger for stiffer floating plates. **Figure 3.14(c)** shows that the use of hinge connections in very flexible floating structures is not very effective in reducing the maximum bending moment.

It is important to note that the maximum bending moment could increase even if more hinge connections are used. This unexpected phenomenon appears when the wavelength is relatively short. For example, for the case $L_r = 1.0$ in **Figure. 3.14(a)**, the maximum bending moment of the floating plate structure with 1 hinge connection is larger than that without any hinge connection when $\alpha = 0.45$. A similar phenomenon is shown in **Figures. 3.14(b)** and **(c)**, but the range of the wavelength where the phenomenon appears depends on the aspect ratio and bending stiffness of the floating plate structures.

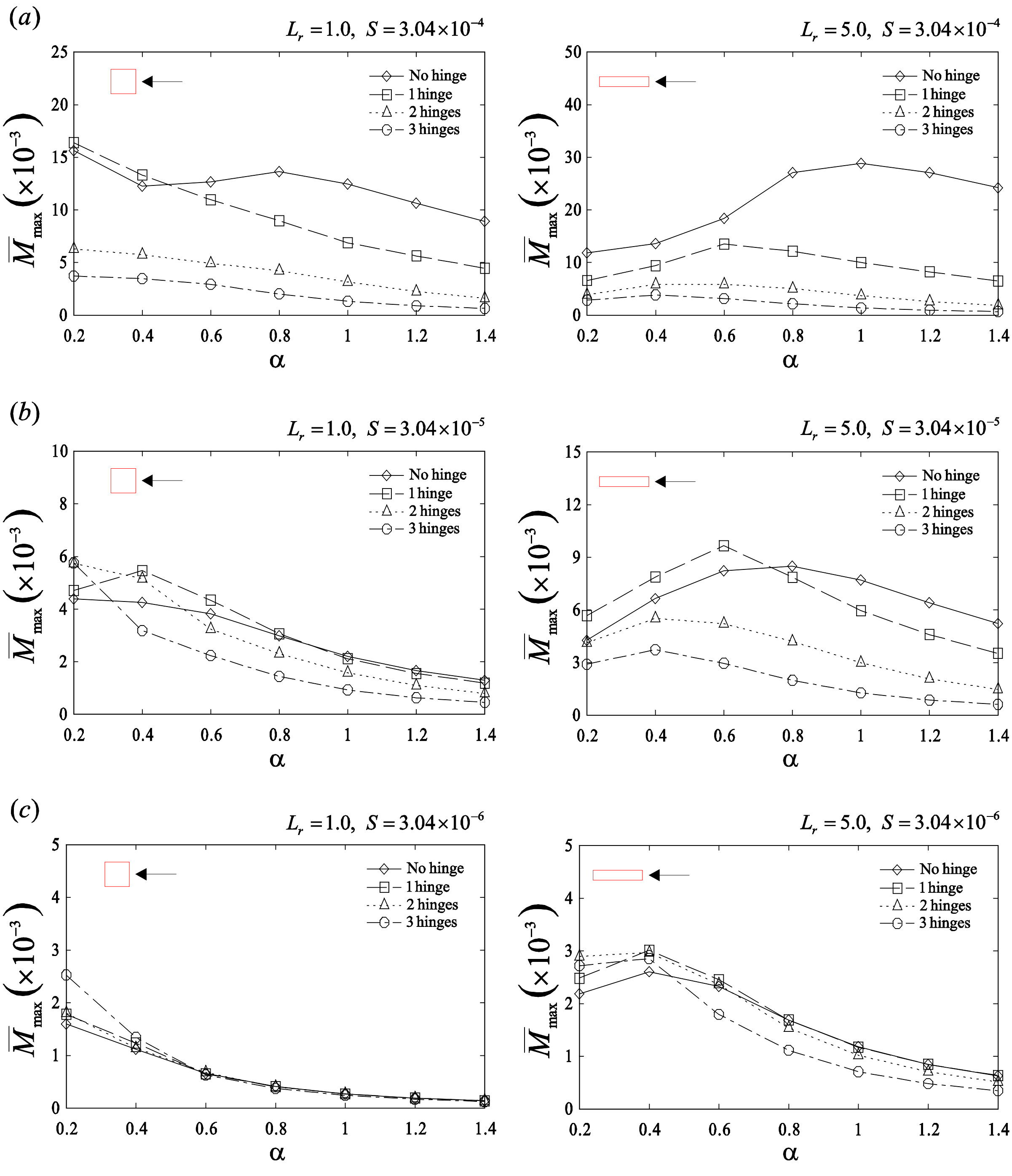

Figure 3.14. RAOs of the dimensionless maximum bending moment $\overline{M}_{\max}$ of floating plate structures with two different aspect ratios: $L_r = 1.0$ and 5.0: (a) $S = 3.04\times10^{-4}$, (b) 3.04×10^{-5}, and (c) 3.04×10^{-6} under an incident regular wave ($\theta = 0°$)

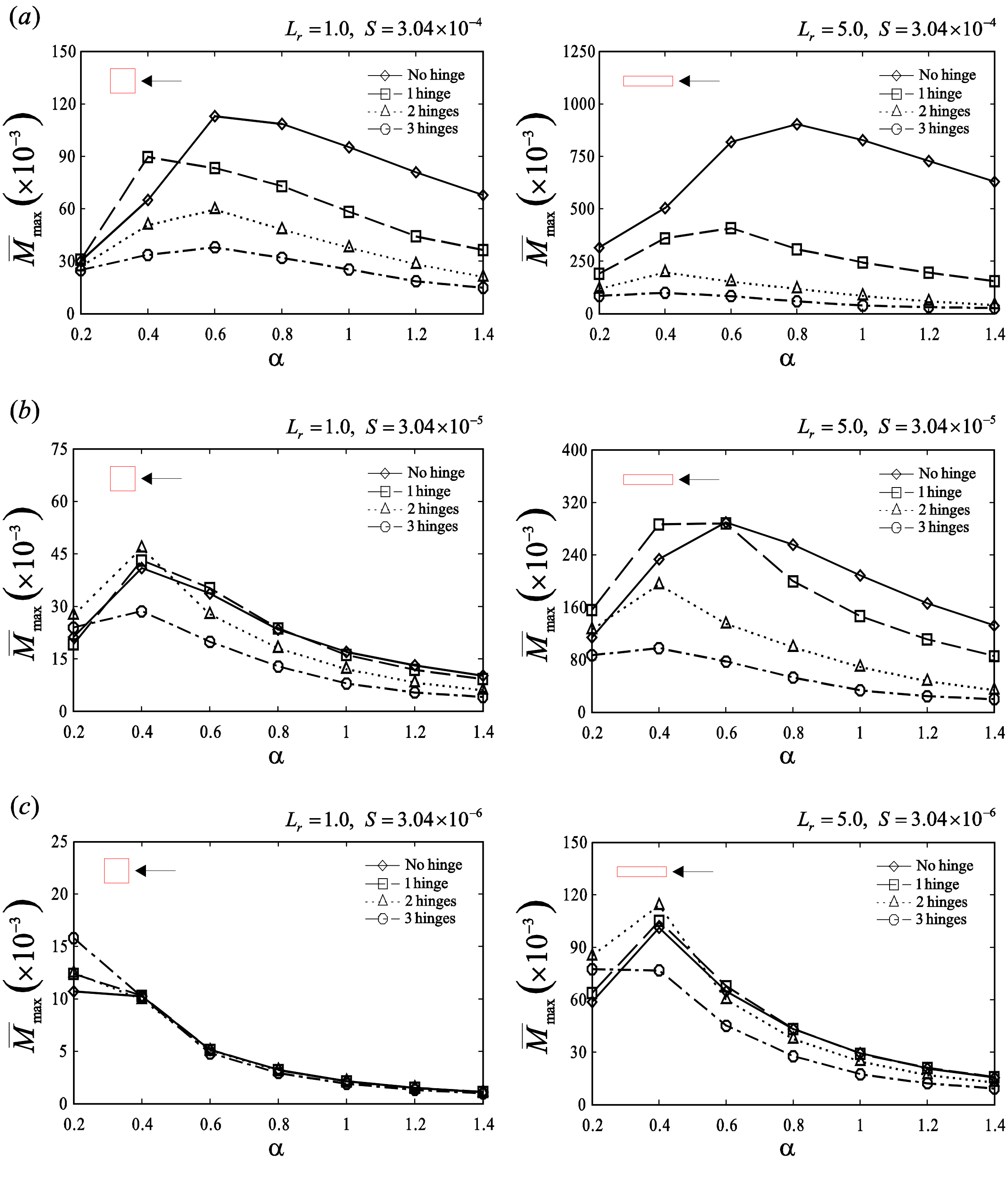

Figure 3.15. RAOs of the dimensionless maximum bending moment $\overline{M}_{\max}$ of floating plate structures with two different aspect ratios: $L_r = 1.0$ and 5.0: (a) $S = 3.04\times10^{-4}$, (b) 3.04×10^{-5}, and (c) 3.04×10^{-6} under an incident regular wave ($\theta = 30°$).

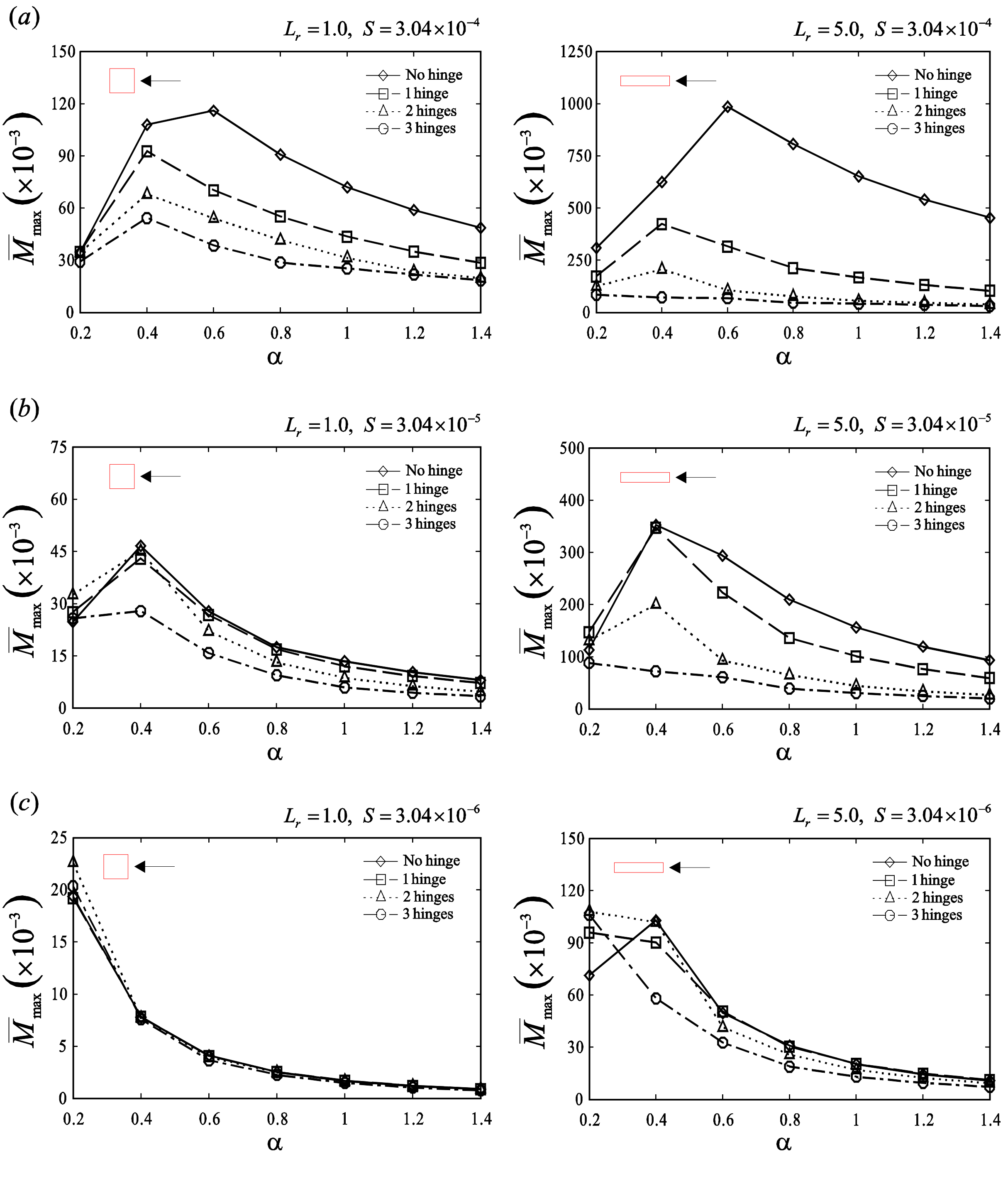

Figure 3.16. RAOs of the dimensionless maximum bending moment $\overline{M}_{\max}$ of floating plate structures with two different aspect ratios: $L_r = 1.0$ and 5.0: (a) $S = 3.04\times10^{-4}$, (b) 3.04×10^{-5}, and (c) 3.04×10^{-6} under an incident regular wave ($\theta = 45°$).

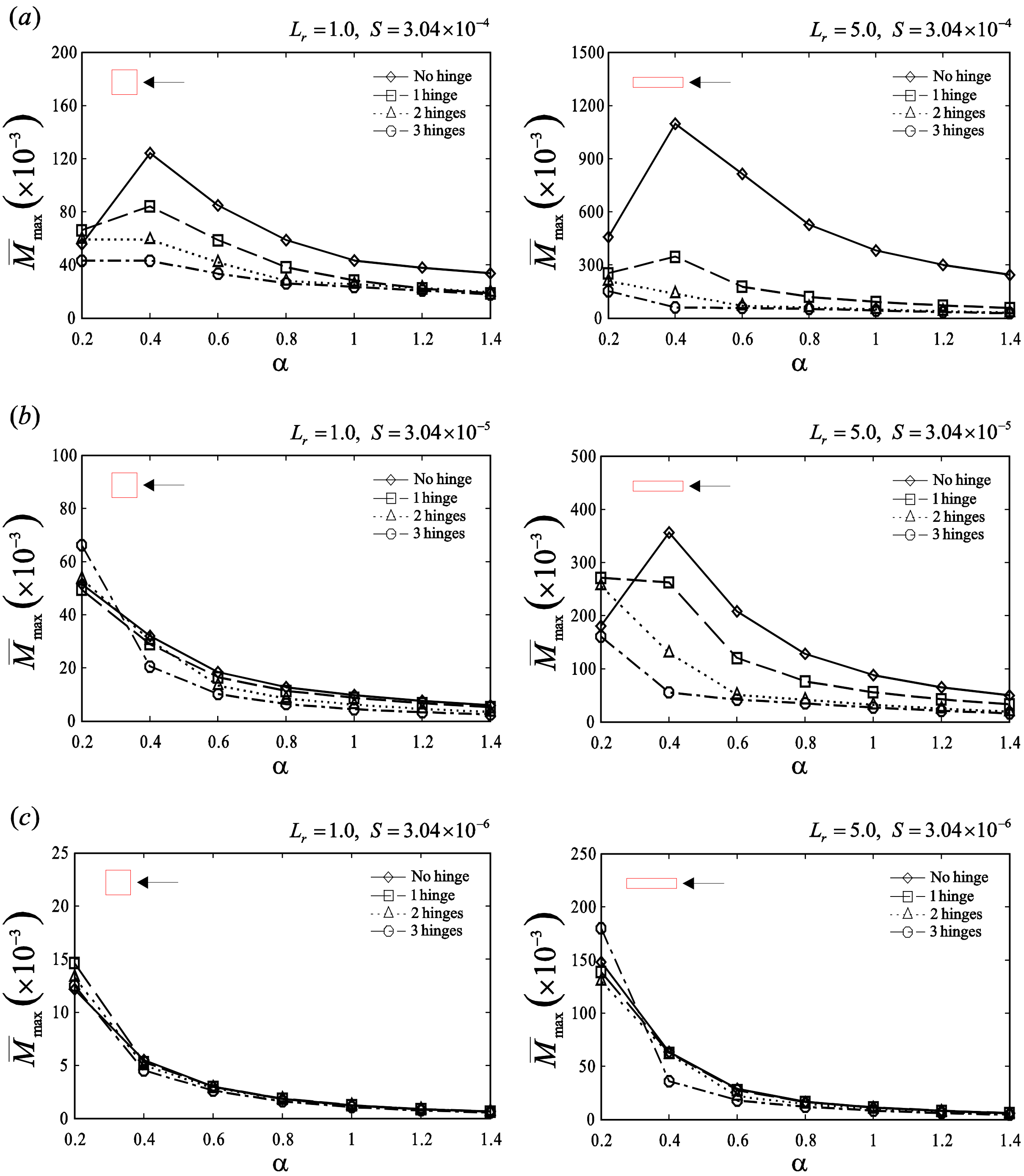

Figure 3.17. RAOs of the dimensionless maximum bending moment $\overline{M}_{max}$ of floating plate structures with two different aspect ratios: $L_r = 1.0$ and 5.0: (a) $S = 3.04\times10^{-4}$, (b) 3.04×10^{-5}, and (c) 3.04×10^{-6} under an incident regular wave ($\theta = 60°$).

Figure 3.18 ~ 3.21 show the ratio of the maximum bending moments defined by

$$R_M = \frac{\overline{M}_{\max}}{\overline{M}_{\max}^{no\,hinge}}, \tag{3.14}$$

where $\overline{M}_{\max}^{no\,hinge}$ is the maximum bending moment for the no hinge case. In general, as the number of hinge connections increases, the additional reduction in the maximum bending moment becomes smaller for stiffer plates. The reduction effect is larger for relatively longer waves. It should be noted that the reduction in the maximum bending moment by hinge connections can result in smaller size cross-sections and less structural materials in used VLFSs, that is, it can reduce construction cost. However, considering the additional implementation cost for hinge connections, it can be expected that there is an optimal number of hinge connections that can minimize the construction cost. Considering the two aspect ratios studied here, we conclude that the use of multiple hinge connections is more effective for floating structures with a larger aspect ratio.

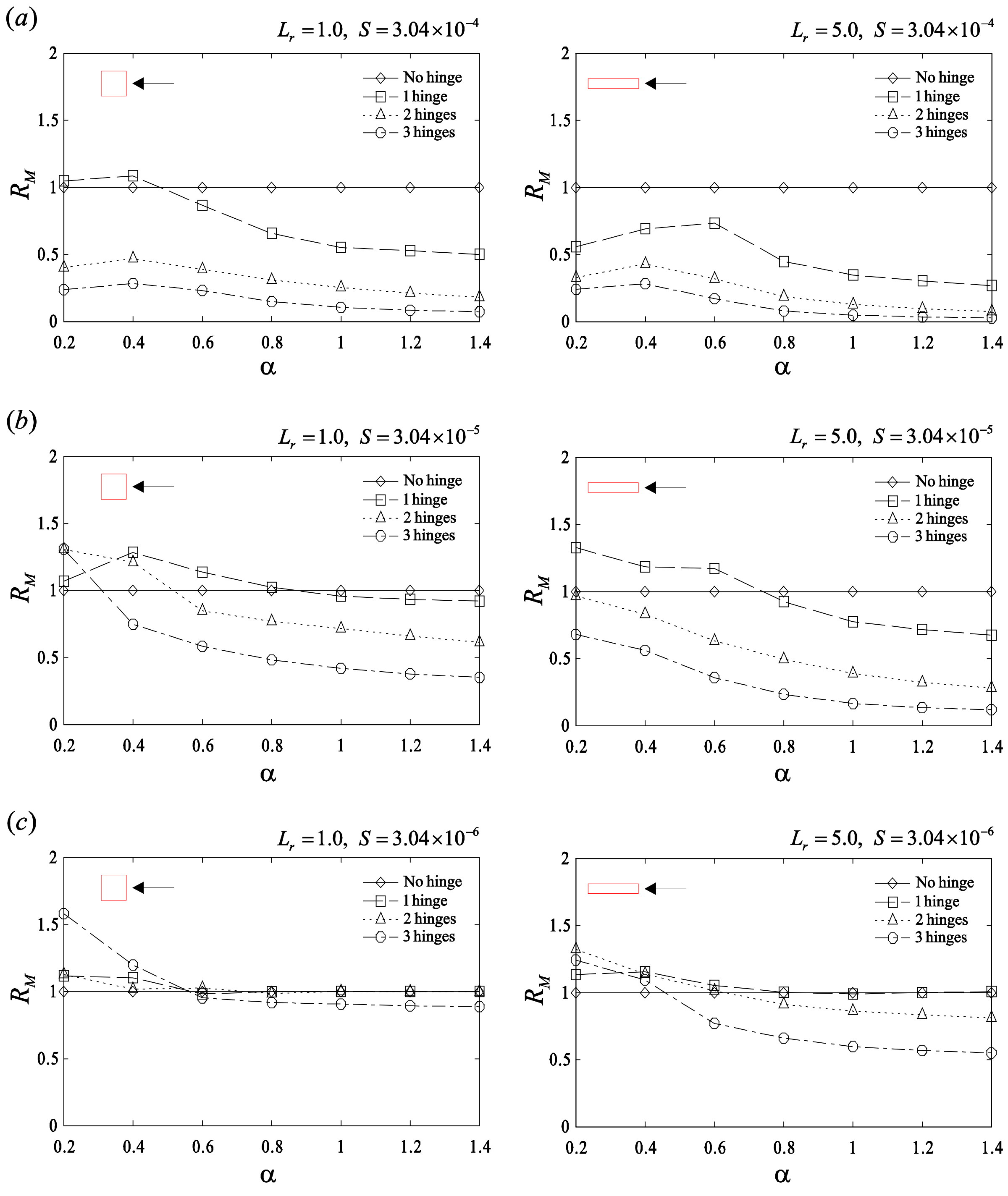

Figure 3.18. Bending moment ratio R_M of floating plate structures with two different aspect ratios: $L_r = 1.0$ and 5.0: (a) $S = 3.04\times10^{-4}$, (b) 3.04×10^{-5}, and (c) 3.04×10^{-6} under an incident regular wave ($\theta = 0°$).

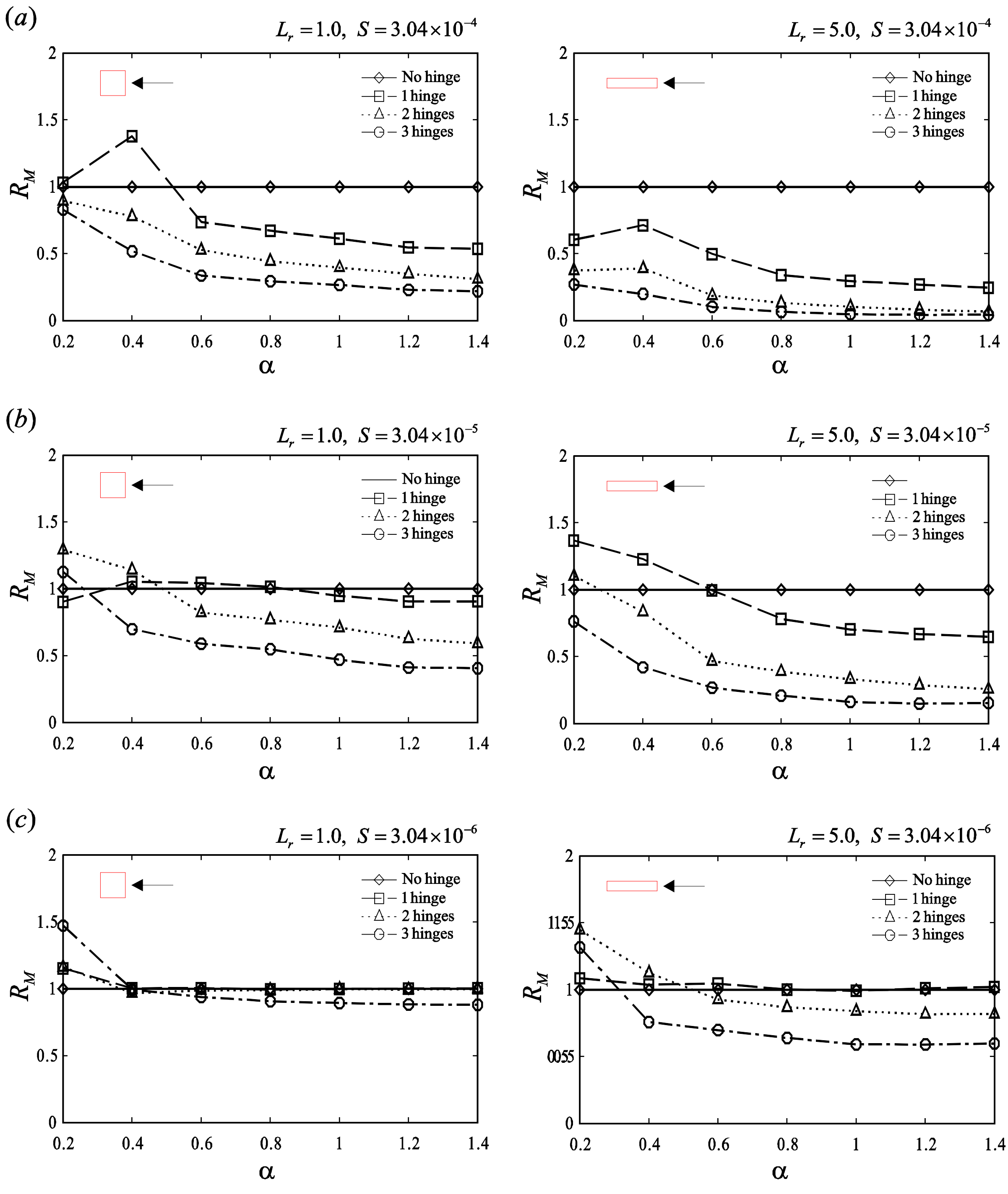

Figure 3.19. Bending moment ratio R_M of floating plate structures with two different aspect ratios: $L_r = 1.0$ and 5.0: (a) $S = 3.04\times10^{-4}$, (b) 3.04×10^{-5}, and (c) 3.04×10^{-6} under an incident regular wave ($\theta = 30°$).

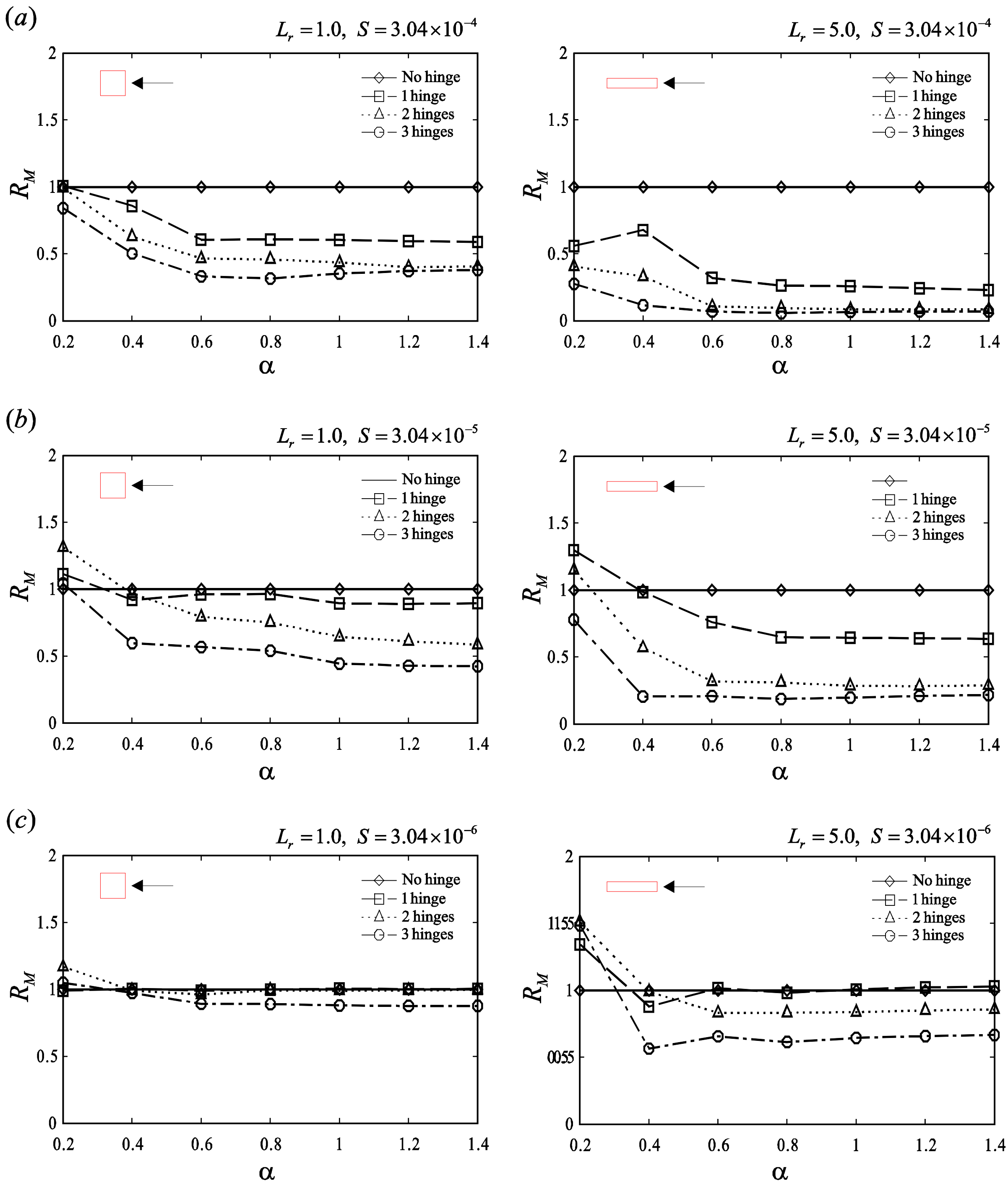

Figure 3.20. Bending moment ratio R_M of floating plate structures with two different aspect ratios: $L_r = 1.0$ and 5.0: (a) $S = 3.04\times10^{-4}$, (b) 3.04×10^{-5}, and (c) 3.04×10^{-6} under an incident regular wave ($\theta = 45°$).

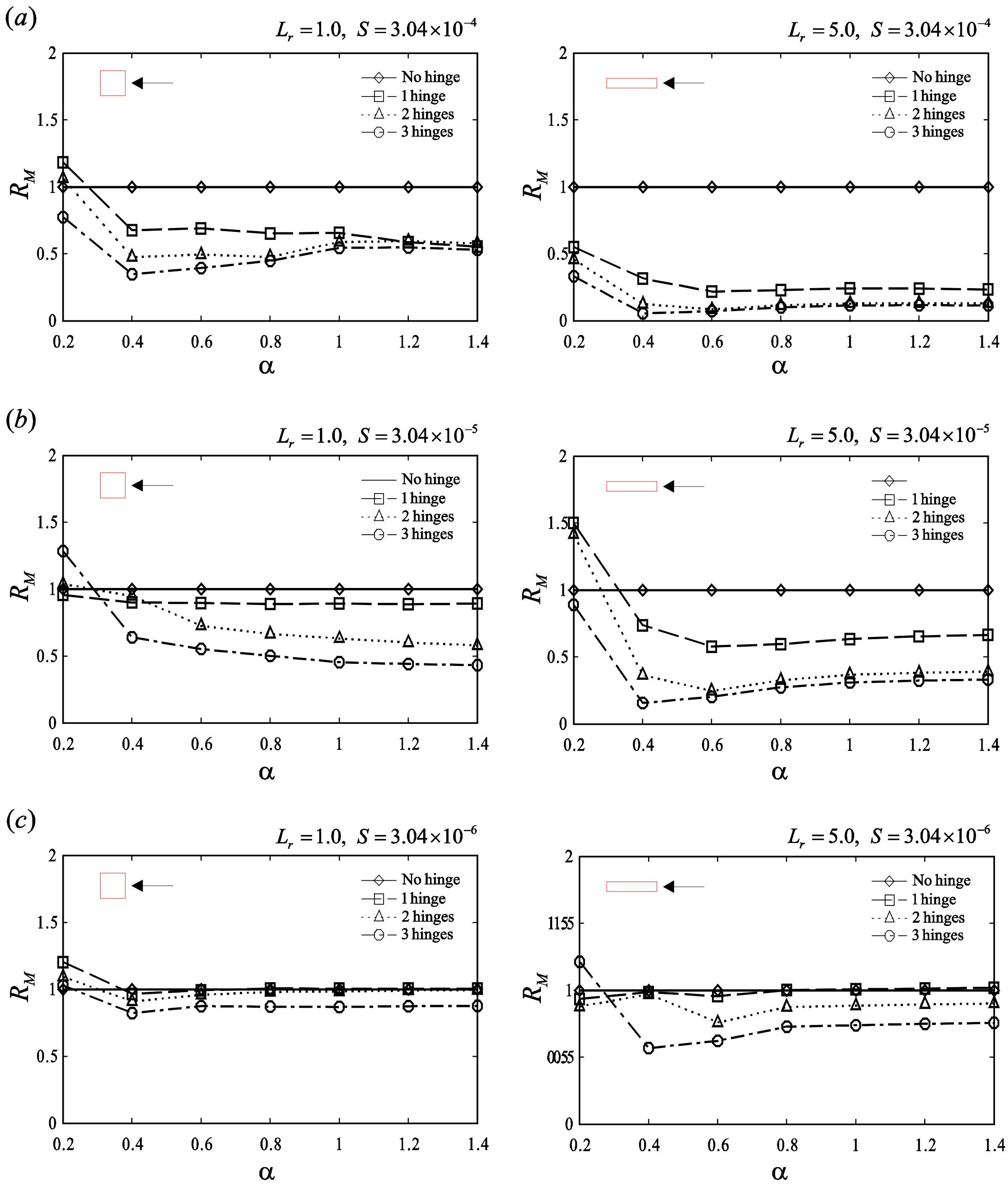

Figure 3.21. Bending moment ratio R_M of floating plate structures with two different aspect ratios: $L_r = 1.0$ and 5.0: (a) $S = 3.04\times10^{-4}$, (b) 3.04×10^{-5}, and (c) 3.04×10^{-6} under an incident regular wave ($\theta = 60°$).

3.3.2 Effects on the Maximum Deflection

In this section, we study how the maximum deflection is influenced by the number of hinge connections used. **Figure 3.22 ~ 3.25** present the RAOs of the maximum deflection $\bar{u}_{3\max}$ for the floating plates with two different aspect ratios ($L_r = 1.0$ and 5.0) depending on dimensionless bending stiffness, wavelength and wave angle. **Figure 3.26 ~ 3.29** show the ratio of the maximum deflection defined by

$$R_M = \frac{|u_3|_{\max}}{|u_3|_{\max}^{no\,hinge}}, \tag{3.15}$$

where $|u_3|_{\max}^{no\,hinge}$ is the maximum deflection for the no hinge case.

Following figures show the effect of the number of hinge connections on the maximum deflection of floating plate structures. In particular, the effect is very large in the range of long wave. Recalling the investigation on the reduction of the maximum bending moment, it is concluded that the use of multiple hinge connections is very effective for larger wavelengths, because, in this case, the maximum bending moment decreases significantly and the maximum deflection has little effect. When the floating structure is very flexible, the effect of multiple hinge connections on the maximum deflection is very small.

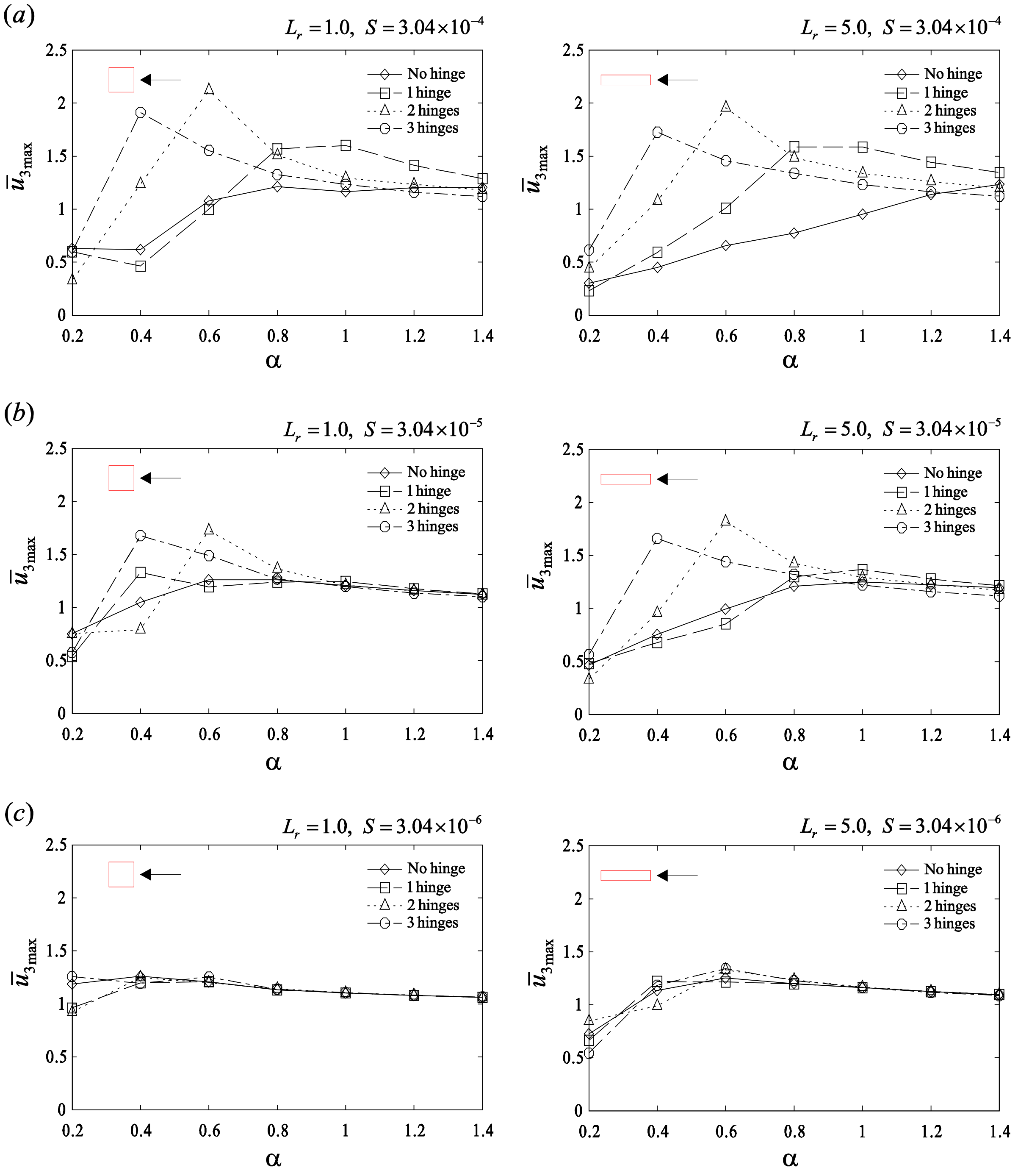

Figure 3.22. RAOs of the maximum deflection $\overline{u}_{3\max}$ of floating plate structures with two different aspect ratios: $L_r = 1.0$ and 5.0: (a) $S = 3.04\times10^{-4}$, (b) 3.04×10^{-5}, and (c) 3.04×10^{-6} under an incident regular wave ($\theta = 0°$).

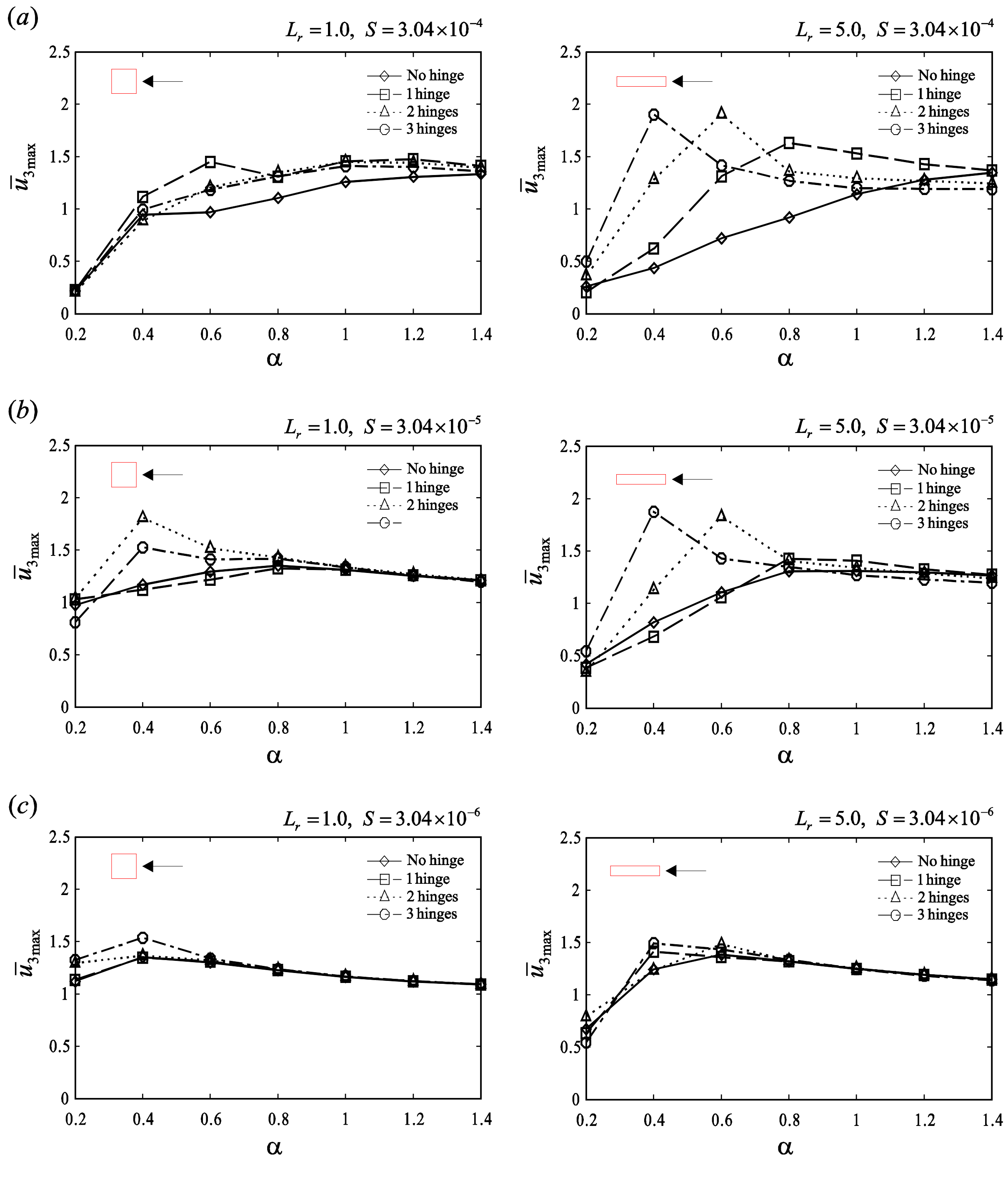

Figure 3.23. RAOs of the maximum deflection $\bar{u}_{3\max}$ of floating plate structures with two different aspect ratios: $L_r = 1.0$ and 5.0: (a) $S = 3.04\times10^{-4}$, (b) 3.04×10^{-5}, and (c) 3.04×10^{-6} under an incident regular wave ($\theta = 30°$).

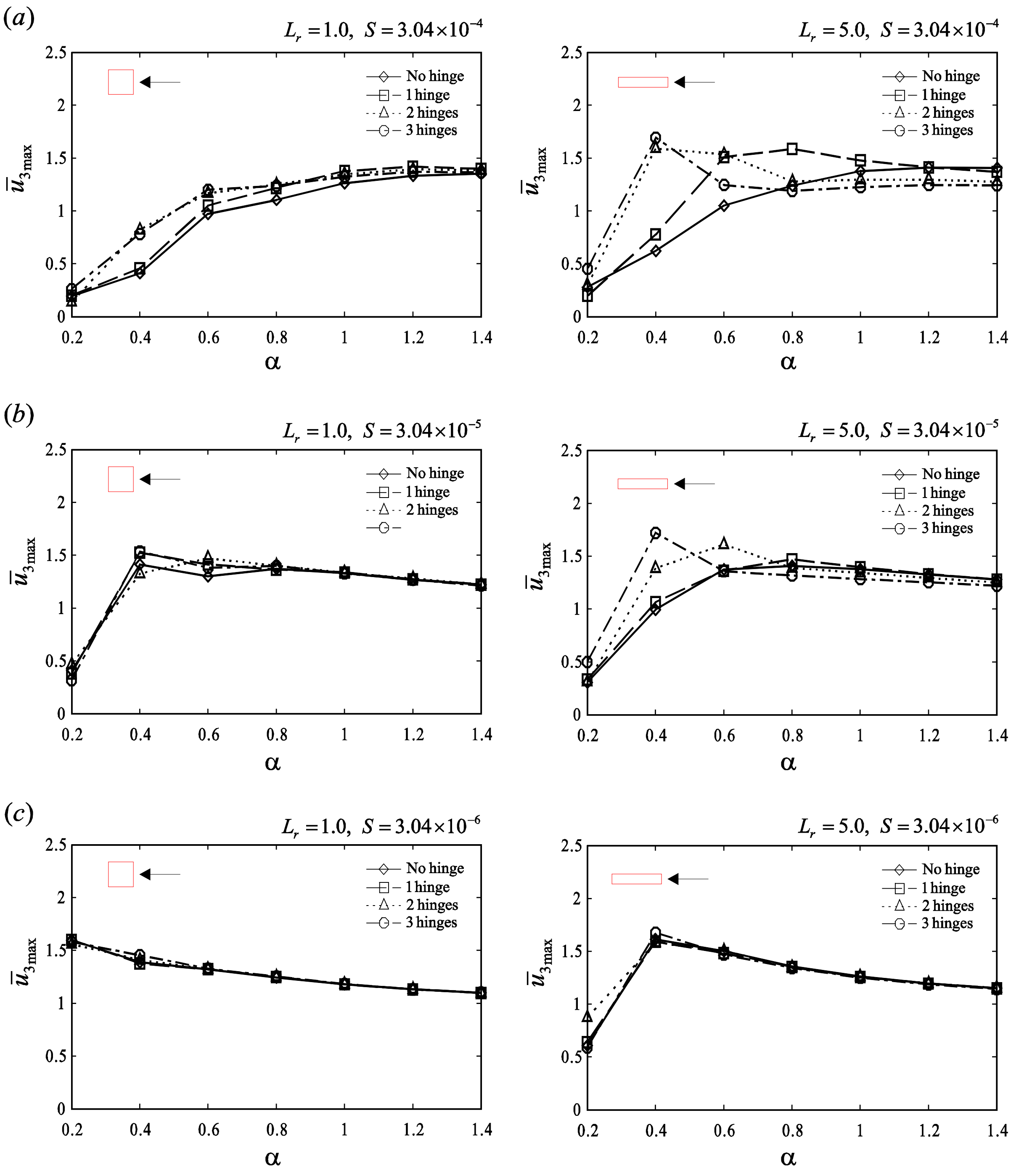

Figure 3.24. RAOs of the maximum deflection $\bar{u}_{3\max}$ of floating plate structures with two different aspect ratios: $L_r = 1.0$ and 5.0: (a) $S = 3.04\times10^{-4}$, (b) 3.04×10^{-5}, and (c) 3.04×10^{-6} under an incident regular wave ($\theta = 45°$).

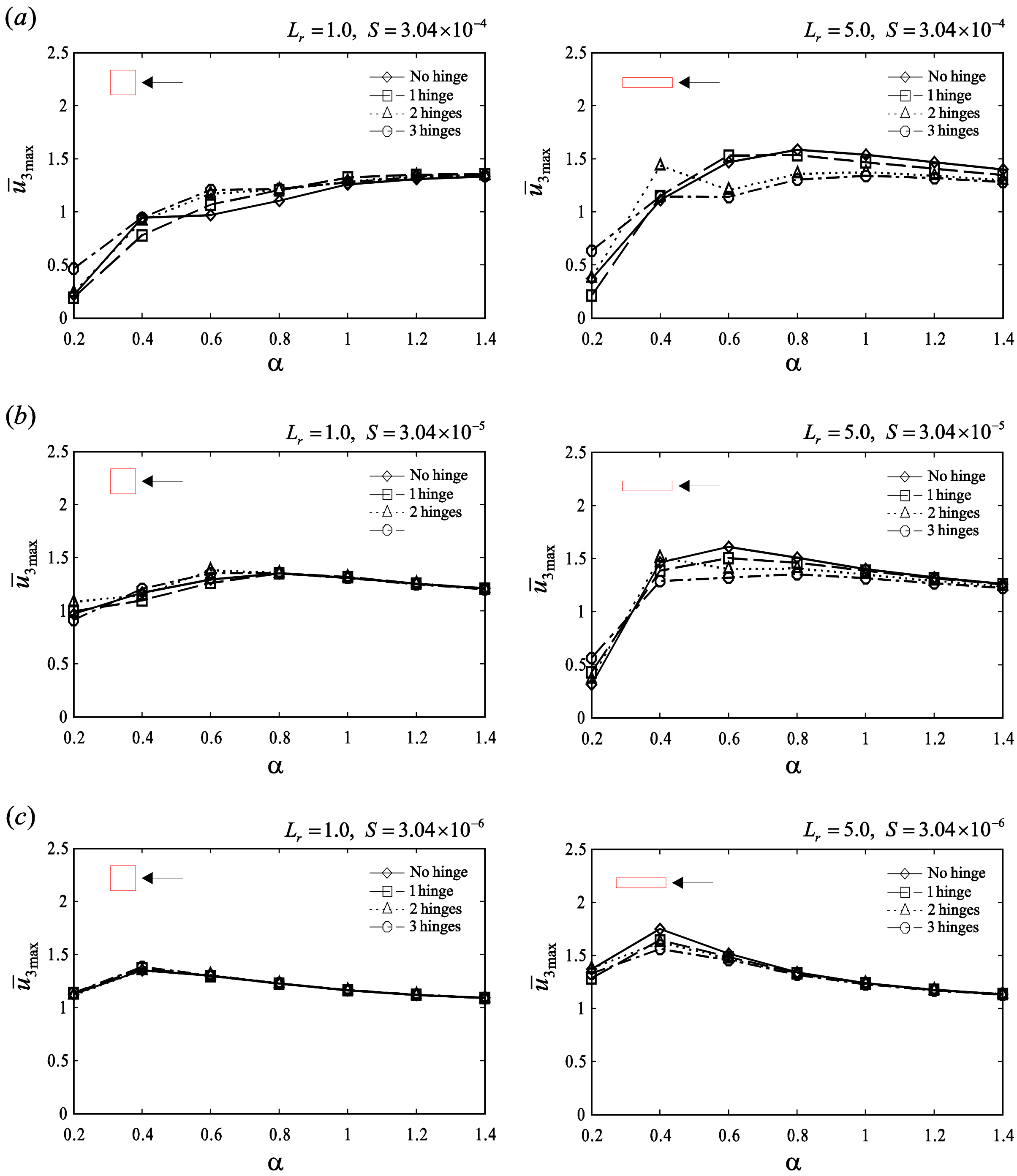

Figure 3.25. RAOs of the maximum deflection $\bar{u}_{3\max}$ of floating plate structures with two different aspect ratios: $L_r = 1.0$ and 5.0: (a) $S = 3.04\times10^{-4}$, (b) 3.04×10^{-5}, and (c) 3.04×10^{-6} under an incident regular wave ($\theta = 60°$).

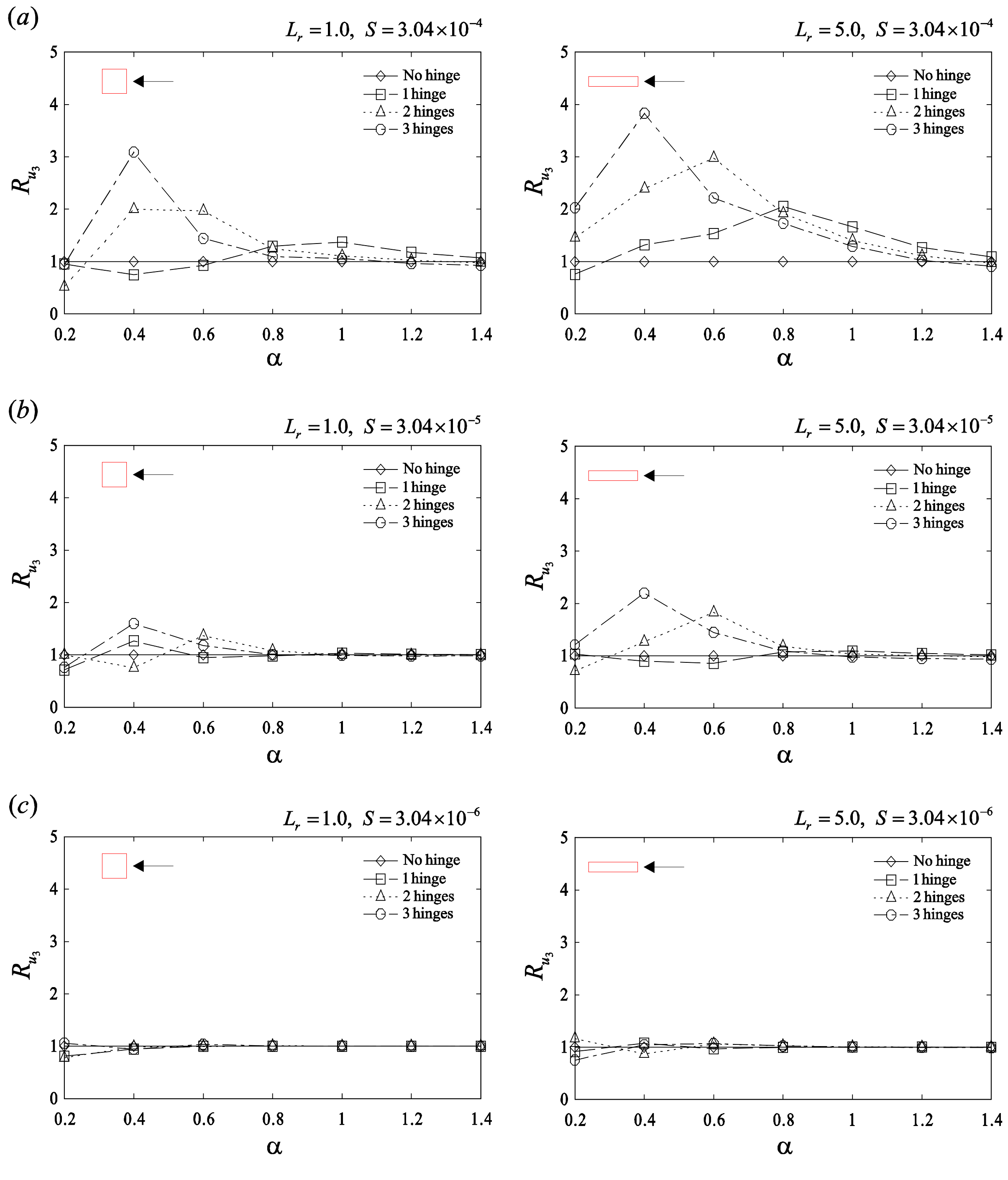

Figure 3.26. Deflection ratio R_{u_3} of floating plate structures with two different aspect ratios: $L_r = 1.0$ and 5.0 : (a) $S = 3.04\times10^{-4}$, (b) 3.04×10^{-5}, and (c) 3.04×10^{-6} under an incident regular wave ($\theta = 0°$).

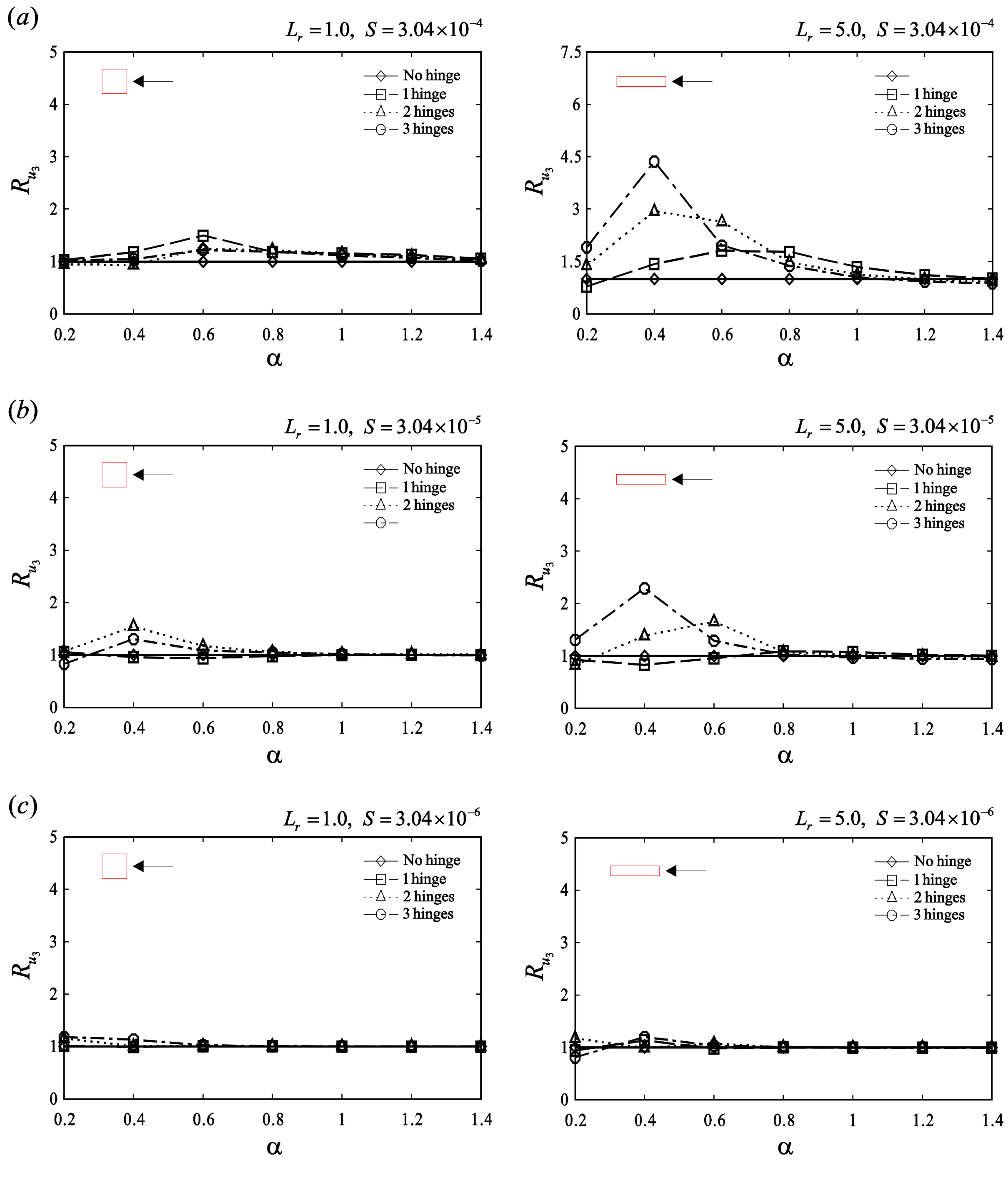

Figure 3.27. Deflection ratio R_{u_3} of floating plate structures with two different aspect ratios: $L_r = 1.0$ and 5.0 : (a) $S = 3.04\times10^{-4}$, (b) 3.04×10^{-5}, and (c) 3.04×10^{-6} under an incident regular wave ($\theta = 30°$).

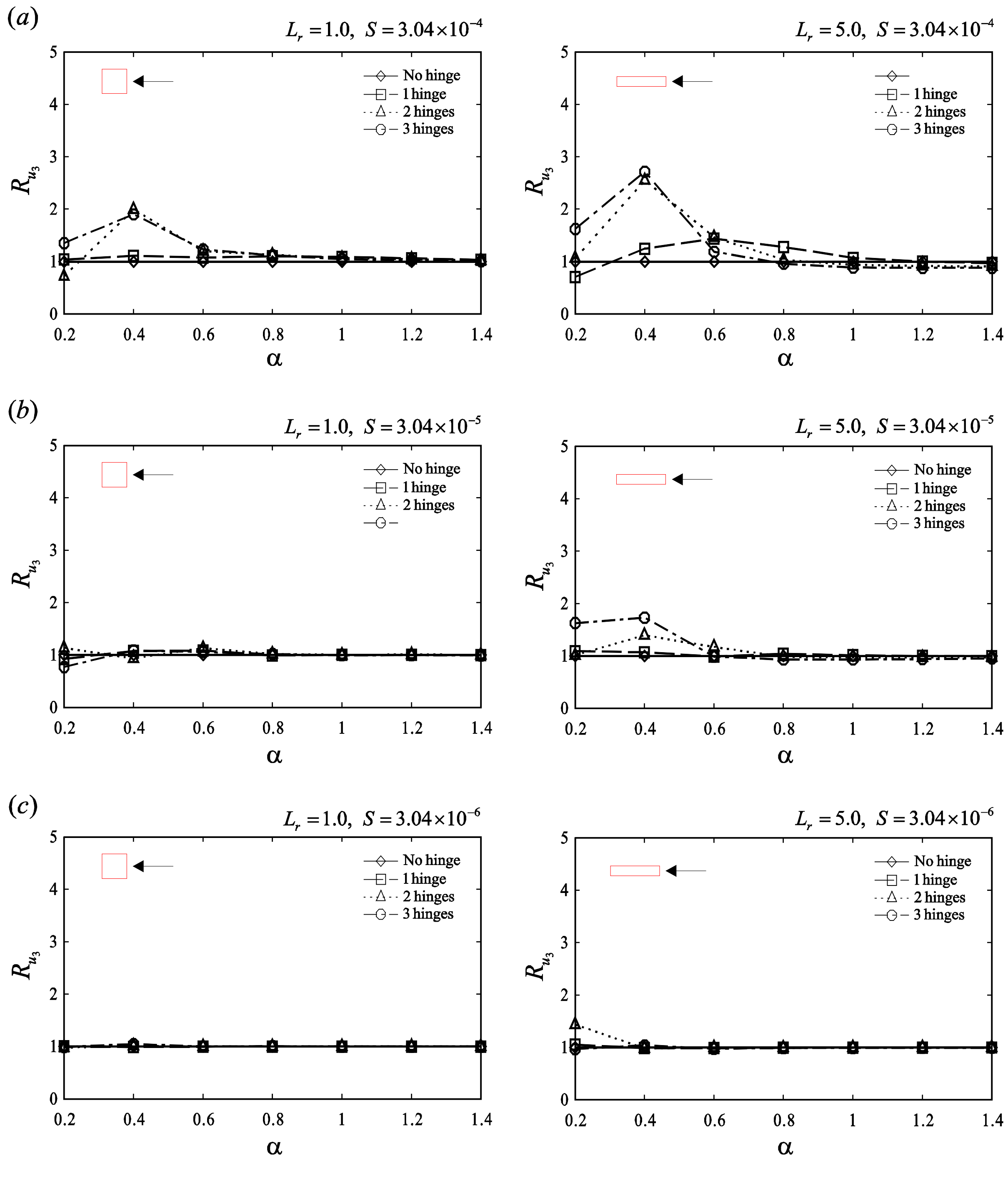

Figure 3.28. Deflection ratio R_{u_3} of floating plate structures with two different aspect ratios: $L_r = 1.0$ and 5.0 : (a) $S = 3.04\times10^{-4}$, (b) 3.04×10^{-5}, and (c) 3.04×10^{-6} under an incident regular wave ($\theta = 45°$).

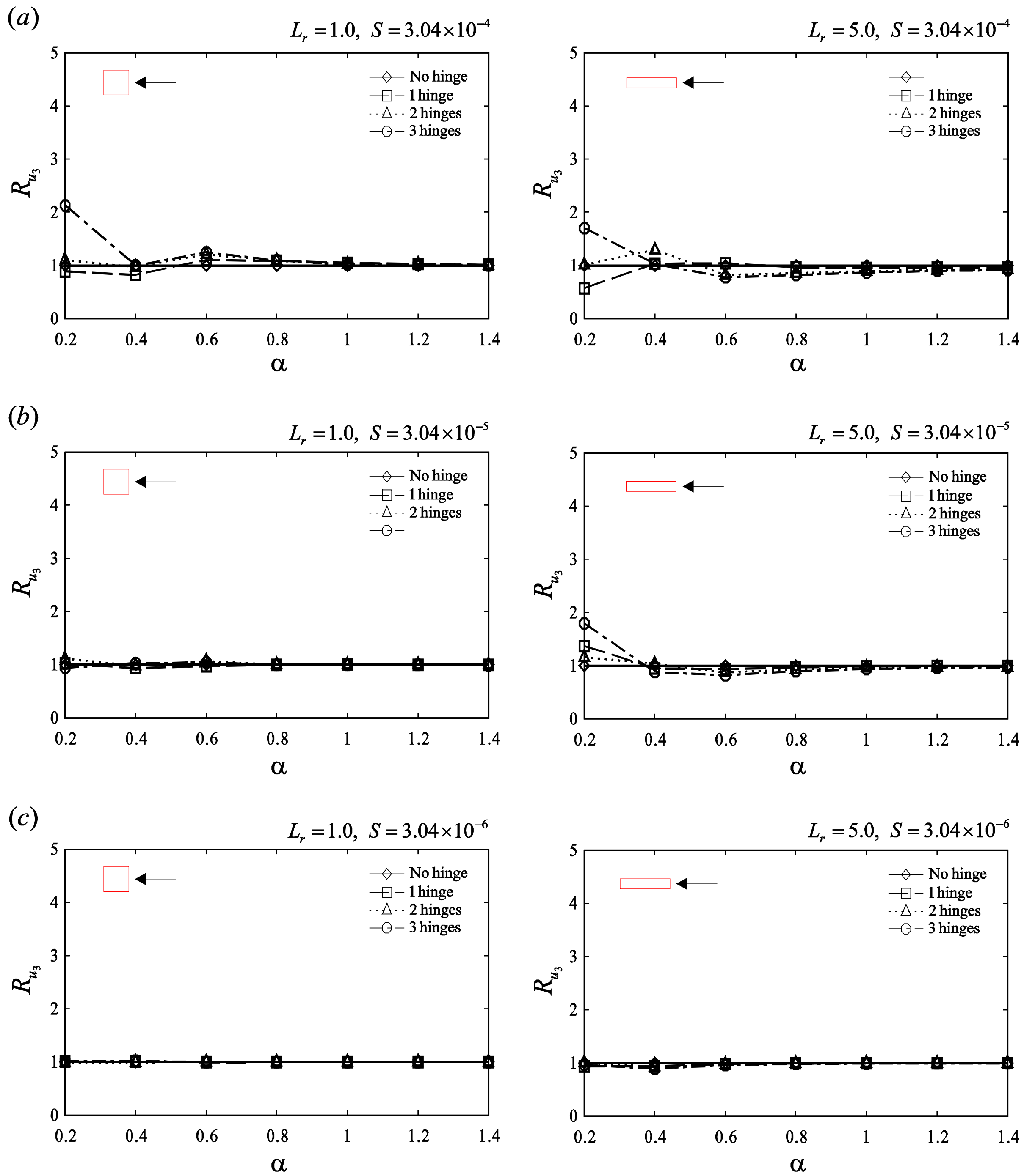

Figure 3.29. Deflection ratio R_{u_3} of floating plate structures with two different aspect ratios: $L_r = 1.0$ and 5.0 : (a) $S = 3.04\times10^{-4}$, (b) 3.04×10^{-5}, and (c) 3.04×10^{-6} under an incident regular wave ($\theta = 60°$).

3.4 Closure

In this chapter, a numerical procedure is proposed to effectively model hinge connections based on the direct coupling method for hydroelastic analysis of floating plate problems. In the formulation, the structural mass and stiffness and fluid-structure interaction terms are completely condensed. The advantage of the procedure exists in the capability to easily model multiple hinge connections arbitrarily positioned. The validity of the numerical procedure was confirmed through comparisons with experimental and previous numerical results. The modeling capability was demonstrated through floating plate problems with 1- and 2-directional multiple hinge connections.

Then, the numerical analyses are performed to investigate the effect of 1-directional multiple hinge connections on the maximum bending moment and deflection in floating plate structures according to aspect ratio, bending stiffness, wavelength, and wave angle. Through this analyses, the following observations have been made:

- In general, as the number of hinge connections increases, the maximum bending moment in the floating plate structure decreases. However, the moment could increase for the range of short wavelength even if more hinge connections are used. The hinge connection can more effectively reduce the maximum bending moment for the stiffer floating plate structure with a larger aspect ratio. Increasing the number of hinge connections, the additional reduction in the maximum bending moment decreases when the plate structures are stiffer.

- In general, the change in the maximum deflection due to hinge connections is large in the range of short wave. It becomes smaller as the wavelength becomes larger.

- When the floating plate structure is very flexible, the effect of the multiple hinge connections on the maximum bending moment and deflection is small. Therefore, the use of hinge connections is not effective in this case.

- When a floating plate structure is stiff, has a large aspect ratio and is subjected to long waves, the hinge connections can be more effectively used with a large reduction in the maximum bending moment and a small change in the maximum deflection.

Finally, the investigation offers valuable information on how to select the number of hinge connections to satisfy structural design requirements.

Chapter 4. A Numerical Method for Hydro-elastoplastic Analysis of Floating Plate Structures

This chapter covers issues for plastic structural behaviors in the hydrodynamic analysis of floating plate structures. The plastic behavior of structural materials is nonlinear and thus the incremental solution procedure needs to be employed. In addition, since interactions between the structures with material nonlinearity and surrounding fluids are a transient phenomenon, a time-domain analysis is necessary.

For the hydro-elastoplastic analysis of floating plate structures subjected to external loads, time-domain incremental coupled equations are formulated, in which elastoplastic material behavior is considered. In the solution procedure, the floating plate structure is discretized using the finite element method, and the surrounding fluid is modeled using the boundary element method. Through comparisons with the numerical results of LS-DYNA, the capability of the proposed numerical procedure is investigated.

4.1 Mathematical Formulations

Let consider a floating plate structure on water surface under a constant water depth as shown in **Figure 4.1**. The basic assumptions used are that the plate structure has homogeneous, isotropic and elastoplastic material, the fluid flow is incompressible, inviscid, and irrotational, and the motions of the plate structure and the amplitudes of incident waves are small enough to use linear theory.

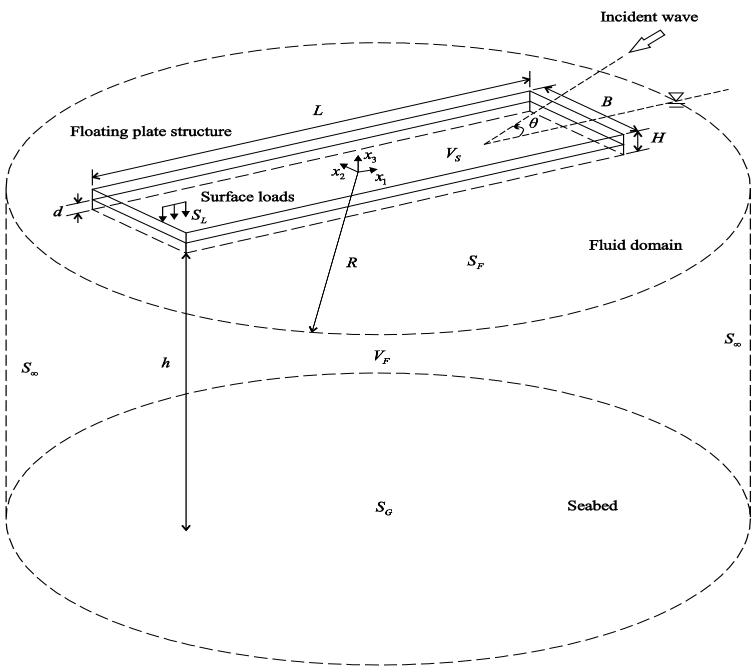

Figure 4.1. Problem description for the hydro-elastoplastic analysis of a floating plate structure

4.1.1 Incremental Equilibrium Equations of Floating Plate Structures

The structural responses associated with material nonlinearity are generally calculated by using incremental equilibrium equations [67], in which, assuming that the responses in the configuration at time t are given, the principle of virtual work in the configuration at time $t+\Delta t$ is considered.

The equilibrium equations of the floating plate at time $t+\Delta t$ are

$$\frac{\partial \sigma_{ij}}{\partial x_j} - \rho_s g \delta_{i3} - \rho_s \ddot{u}_i = 0 \quad \text{in} \quad V_S \,, \tag{4.1a}$$

$$\sigma_{ij} n_j = -p n_i \quad \text{on} \quad S_B \,, \tag{4.1b}$$

$$\sigma_{ij} n_j = f_i^{S_L} n_i \quad \text{on} \quad S_L \,, \tag{4.1c}$$

where $f_i^{S_L}$ is component of the surface load.

The principle of virtual work for the floating plate at time $t+\Delta t$ can be written as

$$\begin{aligned} &\int_{V_S} \sigma_{ij} \delta_{t+\Delta t} e_{ij} \mathrm{d}V \\ &= \int_{S_L} f_i^{S_L} n_i \delta u_i \mathrm{d}V - \int_{V_S} \rho_s g \delta u_3 \mathrm{d}V + \int_{S_B} \rho_w g x_3 n_i \delta u_i \mathrm{d}S - \int_{S_B} p_d n_i \delta u_i \mathrm{d}S - \int_{V_S} \rho_s \ddot{u}_i \delta u_i \mathrm{d}V \,, \end{aligned} \tag{4.2}$$

where

$$\delta_{t+\Delta t} e_{ij} = \frac{1}{2}\left(\frac{\partial \delta u_i}{\partial x_j (t+\Delta t)} + \frac{\partial \delta u_j}{\partial x_i (t+\Delta t)} \right). \tag{4.3}$$

Assuming that the motion of the floating plate structure is small, and only the material nonlinearity is considered, the integral term on the left side of Equation (4.2) can be transformed and linearized as [67]

$$\int_{V_S(t+\Delta t)} \sigma_{ij}(\mathbf{x}; t+\Delta t) \delta_{t+\Delta t} e_{ij} dV \approx \int_{V_S(t)} C_{ijkl}^{EP}(\mathbf{x}; t)\, {}_t e_{kl} \delta_t e_{ij} dV - \int_{V_S(t)} \sigma_{ij}(\mathbf{x}; t) \delta_t e_{ij} dV \,, \tag{4.4}$$

where

$${}_t e_{ij} = \frac{1}{2}\left(\frac{\partial \Delta u_i}{\partial x_j (t)} + \frac{\partial \Delta u_j}{\partial x_i (t)} \right), \tag{4.5}$$

in which Δu_i are components of the increments in the displacements from time t to $t+\Delta t$, and C_{ijkl}^{EP} are components of the elastoplastic stress-strain tensor.

Then, by substituting Equation (2.9) and (4.4) into the terms in Equation (4.2) and referring to the configuration of the static equilibrium at time $t = 0$, the following linearized form is obtained:

$$\begin{aligned}
&\int_{V_S} \rho_s \ddot{u}_i(\mathbf{x};t+\Delta t)\delta u_i dV + \int_{V_S} C_{ijkl}^{EP}(\mathbf{x};t)_0 e_{kl}\delta_0 e_{ij} dV - \int_{S_B} \rho_w g \Delta u_3 n_i \delta u_i dS \\
&= \int_{S_L} f_i^{S_L}(\mathbf{x};t+\Delta t) n_i \delta u_i dS - \int_{S_B} p_d(\mathbf{x};t+\Delta t) n_i \delta u_i dS + \int_{S_B} \rho_w g u_3(\mathbf{x};t) n_i \delta u_i dS \\
&- \int_{V_S} \sigma_{ij}(\mathbf{x};t)\delta_0 e_{ij} dV \ .
\end{aligned} \tag{4.6}$$

Note that, in the derivation of Equation (4.6), the following equilibrium condition for the static equilibrium state is considered as:

$$\int_{S_L} f_i^{S_L}(\mathbf{x};0) n_i \delta u_i dS - \int_{V_S} \rho_s g \delta u_i dV + \int_{S_B} \rho_w g x_3 n_i \delta u_i dS - \int_{V_S} \sigma_{ij}(\mathbf{x};0)\delta e_{ij} dV = 0 \,. \tag{4.7}$$

In order to formulate the material nonlinearity, the tensors of stress σ_{ij} and the elastoplastic stress-strain C_{ijkl}^{EP} in Equation (4.6) are evaluated according to the von Mises plasticity model, which is generally used for describing metal plasticity, with the associated flow rule and isotropic hardening.

4.1.2 The Mathematical Theory of Plasticity

In general, the theory of plasticity deals with structures that, after being subjected to loads, may sustain permanent (or plastic) deformations when completely unloaded, and can be divided into two categories: micromechanical and macromechanical theories, see References [82, 83]. In the former, the mechanism of the plastic deformations is explained on the microscopic scale based on the conditions in crystals and grains leading to plastic flow. The latter describes plastic deformations in the aspect of phenomenological behavior of materials on the marcoscopic scale and establishes relationship between the mechanical quantities (e.g. stresses and strains) based on general principle of mechanics and experimental observations.

The plasticity model can be formulated based on the properties, which are phenomenologically identified in the uniaxial experiments of a metal. The properties are enumerated below:

1. A yield function or yield surface, which gives the yield condition that defines the stress state when plastic flow occurs

2. A plastic flow rule, which describes the relationship between plastic strain and stresses when yielding occurs

3. A hardening rule, which specifies how the yield surface changes with plastic deformation.

Von Mises plastic model with isotropic hardening, which is considered as the plastic model of floating plate structures, is described in detail with the above properties as follows:

1. Yield condition – von Mises criterion, which is appropriate to describe plastic yielding in metals and proposed by von Mises (1913), can defined as

$$f_y(J_2) = J_2 - \frac{1}{3}\sigma_y^2 = 0\,, \tag{4.8}$$

   where f_y is von Mises yield function, J_2 is the second deviatoric stress invariant, and σ_y is the yield stress or

$$f_y(S_{ij}) = \frac{1}{2}S_{ij}S_{ij} - \frac{1}{3}\sigma_y^2 = 0\,, \tag{4.9}$$

   where S_{ij} is the deviatoric stress tensor. The von Mises criterion means yielding begins when the von Mises effective stress ($\sqrt{3J_2}$) reaches σ_y, and implies that the yielding is independent of hydrostatic stresses.

2. Plastic flow rule – Prandtl-Reuss equations, which use the von Mises yield function to obtain the increments of plastic strains when yielding, are given by

$$de_{ij}^P = d\chi\frac{\partial f_y}{\partial \sigma_{ij}} = d\chi S_{ij}\,, \tag{4.10}$$

   where $d\chi$ is a positive scalar to be determined. The equations mean that the increments of plastic strains are in the direction of and proportional to the deviatoric stress.

3. Hardening rule – isotropic hardening rule, which corresponds to the increase in size of the yield surface, can be defined by

$$\sigma_y = \sigma_y(\bar{e}^P)\,, \tag{4.11}$$

   where

$$\bar{e}^P = \int_0^t \sqrt{\frac{2}{3}de_{ij}^P de_{ij}^P} \tag{4.12}$$

   is the accumulated effective plastic strain.

Figure 4.2 shows a geometric interpretation of the von Mises plastic model with isotropic hardening. The yield condition, defined by Equation (4.9), is represented by the surface of a circular cylinder with the radius $R^P = \sqrt{2/3}\sigma_y$ and the hydrostatic axis $\sigma_1 = \sigma_2 = \sigma_3$ in the principal stress space, and by a circle with the radius in the deviatoric plane (π - plane). If the stress state change from t to $t+\Delta t$, the increments of plastic strains are in direction of the current deviatoric stress $S_{ij}(t+\Delta t)$ in the deviatoric plane.

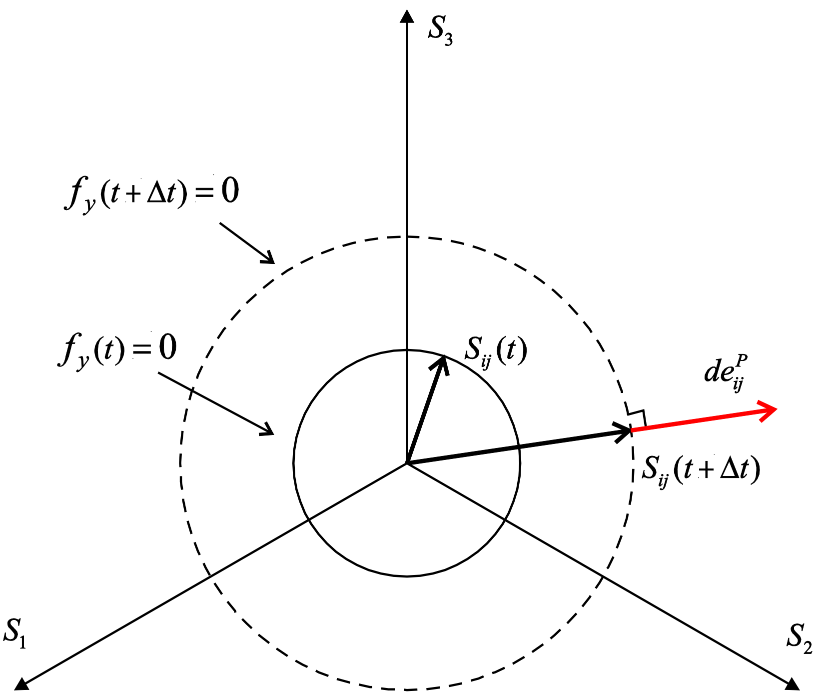

Figure 4.2. A geometric interpretation of the von Mises plastic model.

4.1.3 Hydrodynamic Pressures in the Time Domain

The hydrodynamic analysis of floating plate structures in the time domain has been less well-studied than that in the frequency domain. However, several investigators have used the connection between the time-domain and frequency-domain solution for time-dependent problems. Two approaches have been mainly applied for the time-domain analysis. One is based on a direct time integration and the other is based on a memory effect kernel and is known as the Cummins method [60].

As a direct time integration approach, time-domain analysis on hydroelastic responses of a floating structure in waves was performed by Liu and Sakai [56] using time-stepping computation with a predictor-corrector scheme of the boundary element description for the fluid motions and the finite element model for the structure. Kyoung et al. [57] developed a finite element method with fully nonlinear free-surface conditions considering horizontal motion effect of VLFS in time domain. Qiu [58] employed finite element method to discretize both fluid and structure for analysis the transient hydroelastic responses of an elastic floating beam subjected to dynamic loads.

Cheng et al. [59] proposed a direct time domain modal expansion method that uses a superposition of modal functions with time-dependent unknown modal amplitudes and solves hydrodynamic diffraction and radiation problems by applying the time-dependent free surface Green's functions.

Cummins derives time-dependent equations of rigid body motions for floating bodies, which involve so-called "impulse response functions (IRF)," such as memory functions and added mass at infinite frequency [60]. The Cummins method is by far the more popular because there are some disadvantages in the direct time integration approaches, such as satisfaction of the radiation condition on the outside boundary, necessity of discretizing the entire structure and fluid domain and the relative high computational cost and time. Moreover, the IRF can be related to the corresponding terms in the frequency-domain analysis by Fourier transformation. Kashiwagi [84] developed a numerical method for the time-dependent elastic motion of a plate structure by utilizing a superposition of mathematical modal functions for impulsive motions. Lee and Choi [85] proposed a hybrid method to analyze the transient hydroelastic response of a plate structure by the Fourier inverse transform of harmonic equations, which formulated by boundary element method for fluid domain and FEM for plate domain. To formulate the time-dependent hydrodynamic pressures acting on floating plate structures in the incremental equilibrium equation (4.7), IRFs in Cummins method are constructed.

The velocity potential $\phi(\mathbf{x};t)$ at time t governed by

$$\nabla^2\phi = 0 \quad \text{in} \quad V_F \quad \text{at} \quad t = 0\,, \tag{4.13a}$$

$$\ddot{\phi} + g\frac{\partial\phi}{\partial x_3} = 0 \quad \text{for} \quad x_3 = 0 \quad \text{on} \quad S_F\,, \tag{4.13b}$$

$$\frac{\partial\phi}{\partial x_3} = 0 \quad \text{on} \quad S_G\,, \tag{4.13c}$$

$$\frac{\partial\phi}{\partial n} = \dot{u}_i(\mathbf{x};t)n_i \quad \text{on} \quad S_B \quad \text{at} \quad t = 0\,, \tag{4.13d}$$

with the initial conditions at $t = 0$

$$\phi(\mathbf{x};t) = f_1(\mathbf{x}) \quad \text{for} \quad x_3 = 0 \quad \text{on} \quad S_F\,, \tag{4.14a}$$

$$\dot{\phi}(\mathbf{x};t) = f_2(\mathbf{x}) \quad \text{for} \quad x_3 = 0 \quad \text{on} \quad S_F\,, \tag{4.14b}$$

and ϕ, $\dot{\phi}$, $\nabla\phi$ and $\nabla\dot{\phi}$ are all uniformly bounded as $R \to \infty$ [86, 87], where f_1 and f_2 are functions to represent the initial free surface. The initial conditions prescribe the initial values of the velocity potential on the free surface.

The incremental displacement Δu_i of the floating plate structure can be represented as

$$\Delta\mathbf{u}(\mathbf{x},t) \approx g_k(t)\boldsymbol{\mu}_k(\mathbf{x}) = g_1(t)\boldsymbol{\mu}_1(\mathbf{x}) + g_2(t)\boldsymbol{\mu}_2(\mathbf{x}) + \cdots\cdots, \tag{4.15}$$

where g_k is the generalized coordinates and $\boldsymbol{\mu}_k$ denotes the corresponding basis functions.

Since the fluid motion is assumed to be linear, the velocity potential can be described as the convolution integral of the arbitrary time-dependent motions with the radiation (ϕ^R) and diffraction (ϕ^D) potentials corresponding to the impulsive velocity of the plate and impulsive wave elevation, respectively [6, 88]

$$\phi(\mathbf{x};t) = \int_{-\infty}^{\infty} \phi_k^R(\mathbf{x};t-\tau)\dot{g}_k(\tau)d\tau + \int_{-\infty}^{\infty} \phi^D(\mathbf{x};t-\tau)\eta(\tau)d\tau\,, \tag{4.16}$$

in which ϕ_k^R is the radiation potential for the impulsive velocity corresponding to $\boldsymbol{\mu}_K$, and η is an incident wave elevation.

From both computational and accuracy points of view, it is effective to use dominant dry modes of the plate for the basis functions $\boldsymbol{\mu}_K$. However, in elastoplastic analysis, this approach encounters major difficulty due to the dominant dry modes continuously varying due to the change of tangential stiffness during plastic deformation. In order to overcome such difficulty, a set of piecewise linear (hat) functions defined at nodes for the basis functions is employed. The piecewise linear function has unit value at a node and zero at other nodes (see **Figure 4.3**). The function can be constructed using standard 2D shape functions of finite elements sharing the node.

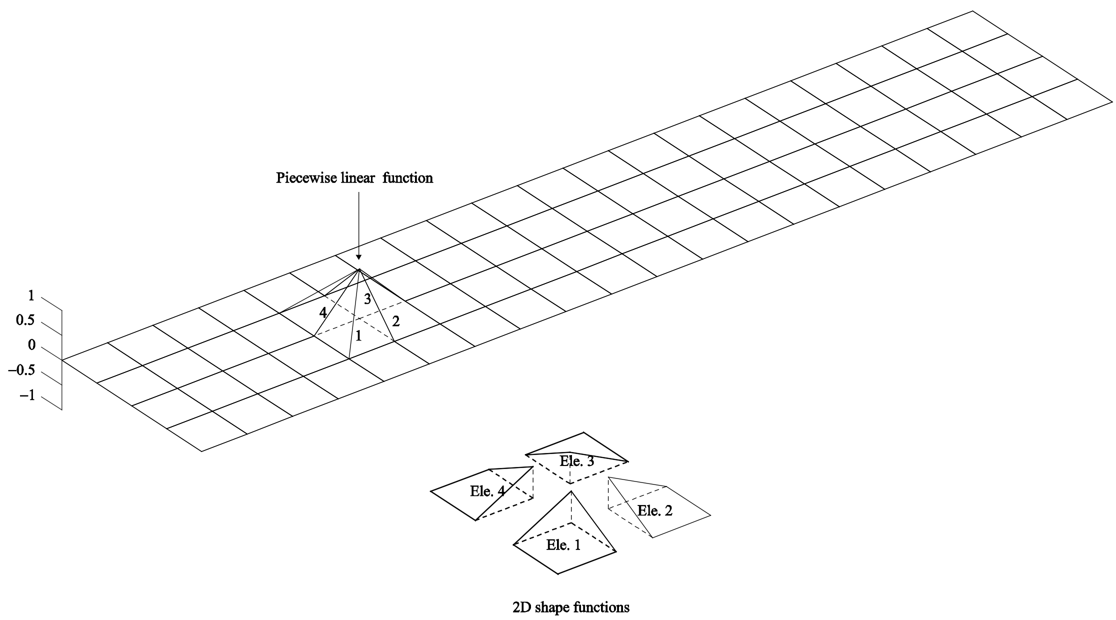

Figure 4.3. Piecewise linear function at a node and 2D shape functions in finite elements.

The radiation potential ϕ_k^R in Equation (4.16) can be decomposed as

$$\phi_k^R(\mathbf{x};t) = \psi_k(\mathbf{x})\delta(t) + \varphi_k(\mathbf{x};t)H(t)\,, \tag{4.17}$$

in which H is the Heaviside function, and ψ_k is the radiation potential at infinite frequency, satisfying the boundary value problem with following conditions:

$$\nabla^2\psi_k = 0 \quad \text{in} \quad V_F \quad \text{at} \quad t=0\,, \tag{4.18a}$$

$$\psi_k = 0 \quad \text{for} \quad x_3 = 0 \quad \text{on} \quad S_F\,, \tag{4.18b}$$

$$\frac{\partial \psi_k}{\partial x_3} = 0 \quad \text{on} \quad S_G\,, \tag{4.18c}$$

$$\frac{\partial \psi_k}{\partial x_3} = \boldsymbol{\mu}_k \cdot \mathbf{n} \quad \text{on} \quad S_B \quad \text{at} \quad t=0\,. \tag{4.18d}$$

In addition, φ_k in Equation (4.17) is the radiation potential representing the fluid motion subsequent to the impulsive velocity satisfying the initial-boundary value problem with the boundary and initial conditions:

$$\nabla^2\varphi_k = 0 \quad \text{in} \quad V_F \quad \text{at} \quad t=0\,, \tag{4.19a}$$

$$\ddot{\varphi}_k + g\frac{\partial \varphi_k}{\partial x_3} = 0 \quad \text{for} \quad x_3 = 0 \quad \text{on} \quad S_F\,, \tag{4.19b}$$

$$\frac{\partial \varphi_k}{\partial x_3} = 0 \quad \text{on} \quad S_G\,, \tag{4.19c}$$

$$\frac{\partial \varphi_k}{\partial x_3} = 0 \quad \text{on} \quad S_B \quad \text{at} \quad t=0\,, \tag{4.19d}$$

with the initial conditions at $t=0$

$$\varphi_k(\mathbf{x};t) = 0 \quad \text{for} \quad x_3 = 0 \quad \text{on} \quad S_F\,. \tag{4.20a}$$

$$\dot{\varphi}_k(\mathbf{x};t) = 0 \quad \text{for} \quad x_3 = 0 \quad \text{on} \quad S_F\,. \tag{4.20b}$$

The diffraction potential ϕ^D in Equation (4.16) is the sum of the transient incident ϕ^I and scattered ϕ^S potentials which satisfies the initial-boundary value problem with the conditions [6].

$$\nabla^2\phi^D = 0 \quad \text{in} \quad V_F \quad \text{at} \quad t=0\,, \tag{4.21a}$$

$$\ddot{\phi}^D + g\frac{\partial \phi^D}{\partial x_3} = 0 \quad \text{for} \quad x_3 = 0 \quad \text{on} \quad S_F\,, \tag{4.21b}$$

$$\frac{\partial \phi^D}{\partial x_3} = 0 \quad \text{on} \quad S_G\,, \tag{4.21c}$$

$$\frac{\partial \phi^D}{\partial n} = \frac{\partial \phi^I}{\partial n} + \frac{\partial \phi^S}{\partial n} = 0 \quad \text{on} \quad S_B \quad \text{at} \quad t=0\,, \tag{4.21d}$$

with the initial conditions at $t = 0$

$$\phi^D(\mathbf{x};t) = 0 \quad \text{for} \quad x_3 = 0 \quad \text{on} \quad S_F \,. \tag{4.22a}$$

$$\dot{\phi}^D(\mathbf{x};t) = 0 \quad \text{for} \quad x_3 = 0 \quad \text{on} \quad S_F \,. \tag{4.22b}$$

Using the linearized Bernoulli equation, the hydrodynamic pressure p_d can be expressed as follows:

$$p_d(\mathbf{x};t) = -\rho_w \left[\psi_k(\mathbf{x})\ddot{g}_k(t) + \int_{-\infty}^{t} \dot{\varphi}_k(\mathbf{x};t-\tau)\dot{g}_k(\tau)d\tau + \int_{-\infty}^{\infty} \dot{\phi}^D(\mathbf{x};t-\tau)\eta(\tau)d\tau \right], \tag{4.23}$$

where $\ddot{g}_k$ and $\dot{g}_k$ means the acceleration and velocity with respect to the basis functions $\boldsymbol{\mu}_K$.

Then, by substituting the aforementioned equation into the hydrodynamic pressure p_d in Equation (4.6), the time-domain incremental coupled equations of motion at time $t + \Delta t$ is finally obtained:

$$\begin{aligned}
&\int_{V_S} \rho_s \ddot{u}_i(\mathbf{x};t+\Delta t)\delta u_i dV - \int_{S_B} \rho_w \psi_k \ddot{g}_k(t+\Delta t) n_i \delta u_i dS \\
&- \int_{-\infty}^{t+\Delta t} \int_{S_B} \rho_w \dot{\varphi}_k(\mathbf{x};t+\Delta t-\tau)\, \dot{g}_k(\tau) n_i \delta u_i dS d\tau + \int_{V_S} C_{ijkl}^{EP}\, {}_0e_{kl}\delta_0 e_{ij} dV - \int_{S_B} \rho_w g \Delta u_3 n_i \delta u_i dS \\
&= \int_{S_L} f_i^{S_L}(\mathbf{x};t+\Delta t) n_i \delta u_i dS - \int_{-\infty}^{\infty} \int_{S_B} \rho_w \phi^D(\mathbf{x};t+\Delta t-\tau)\eta(\tau) n_i \delta u_i dS d\tau + \int_{S_B} \rho_w g u_3(\mathbf{x};t) n_i \delta u_i dS \\
&- \int_{V_S} \sigma_{ij}(\mathbf{x};t)\delta_0 e_{ij} dV \;\; .
\end{aligned} \tag{4.24}$$

4.2 Numerical Procedure

The formulation in Equation (4.24) can be transformed into matrix form using the finite element discretization as

$$\begin{aligned}
&(\mathbf{M}+\mathbf{A})\ddot{\mathbf{U}}(t+\Delta t) + \int_{-\infty}^{t+\Delta t} \mathbf{B}(t+\Delta t-\tau)\dot{\mathbf{U}}(\tau)d\tau + \left(\mathbf{K}(t)+\mathbf{C}\right)\Delta\mathbf{U} \\
&= \mathbf{R}_{S_L}(t+\Delta t) + \int_{-\infty}^{\infty} \mathbf{D}(t+\Delta t-\tau)\eta(\tau)d\tau - \mathbf{C}\mathbf{U}(t) - \mathbf{F}(t) \,,
\end{aligned} \tag{4.25}$$

in which $\ddot{\mathbf{U}}$, $\dot{\mathbf{U}}$, $\mathbf{U}$, and $\Delta\mathbf{U}$ are the acceleration, velocity, displacement and incremental displacement vectors, respectively, and the submatrices and subvectors are defined as follows:

$$\int_{V_S} \rho_s \ddot{u}_i(\mathbf{x};t+\Delta t)\delta u_i dV = \delta\mathbf{U}^T \mathbf{M}\ddot{\mathbf{U}}(t+\Delta t) \,, \tag{4.26a}$$

$$-\int_{S_B} \rho_w \psi_k \ddot{g}_k(t+\Delta t) n_i \delta u_i dS = \delta\mathbf{U}^T \mathbf{A}\ddot{\mathbf{U}}(t+\Delta t) \,, \tag{4.26b}$$

$$-\int_{-\infty}^{t+\Delta t}\int_{S_B}\rho_w\dot{\varphi}_k(\mathbf{x};t+\Delta t-\tau)\,\dot{g}_k(\tau)n_i\delta u_i dSd\tau=\delta\mathbf{U}^T\int_{-\infty}^{t+\Delta t}\mathbf{B}(t+\Delta t-\tau)\mathbf{U}(\tau)\,, \tag{4.26c}$$

$$\int_{V_S}C_{ijkl}^{EP}\,{}_0e_{kl}\delta\,{}_0e_{ij}dV=\delta\mathbf{U}^T\mathbf{K}(t)\Delta\mathbf{U}\,, \tag{4.26d}$$

$$-\int_{S_B}\rho_w g\Delta u_3 n_i\delta u_i dS=\delta\mathbf{U}^T\mathbf{C}\Delta\mathbf{U}\,, \tag{4.26e}$$

$$\int_{S_L}f_i^{S_L}(\mathbf{x};t+\Delta t)n_i\delta u_i dS=\delta\mathbf{U}^T\mathbf{R}_{S_L}(t+\Delta t)\,, \tag{4.26f}$$

$$-\int_{-\infty}^{\infty}\int_{S_B}\rho_w\phi^D(\mathbf{x};t+\Delta t-\tau)\,\eta(\tau)n_i\delta u_i dSd\tau=\delta\mathbf{U}^T\int_{-\infty}^{\infty}\mathbf{D}(t+\Delta t-\tau)\eta(\tau)d\tau\,, \tag{4.26g}$$

$$\int_{S_B}\rho_w g u_3(\mathbf{x};t)n_i\delta u_i dS=\delta\mathbf{U}^T\mathbf{C}\mathbf{U}(t)\,, \tag{4.26h}$$

$$\int_{V_S}\sigma_{ij}(\mathbf{x};t)\delta\,{}_0e_{ij}dV=\delta\mathbf{U}^T\mathbf{F}(t)\,, \tag{4.26i}$$

in which $\mathbf{M}$ and $\mathbf{K}$ are the structural mass and tangential stiffness matrices, respectively, $\mathbf{R}_{S_L}$ is the surface load vector and $\mathbf{F}$ is the internal force vector, and $\mathbf{A}$, $\mathbf{B}$, and $\mathbf{D}$ denote the impulse response functions corresponding to the added mass at infinite frequency, the memory function and the diffraction impulse-function, respectively, and is the hydrostatic stiffness matrix.

Figure 4.4 presents a numerical solution procedure developed for the present formulation, in which the following three important parts are involved

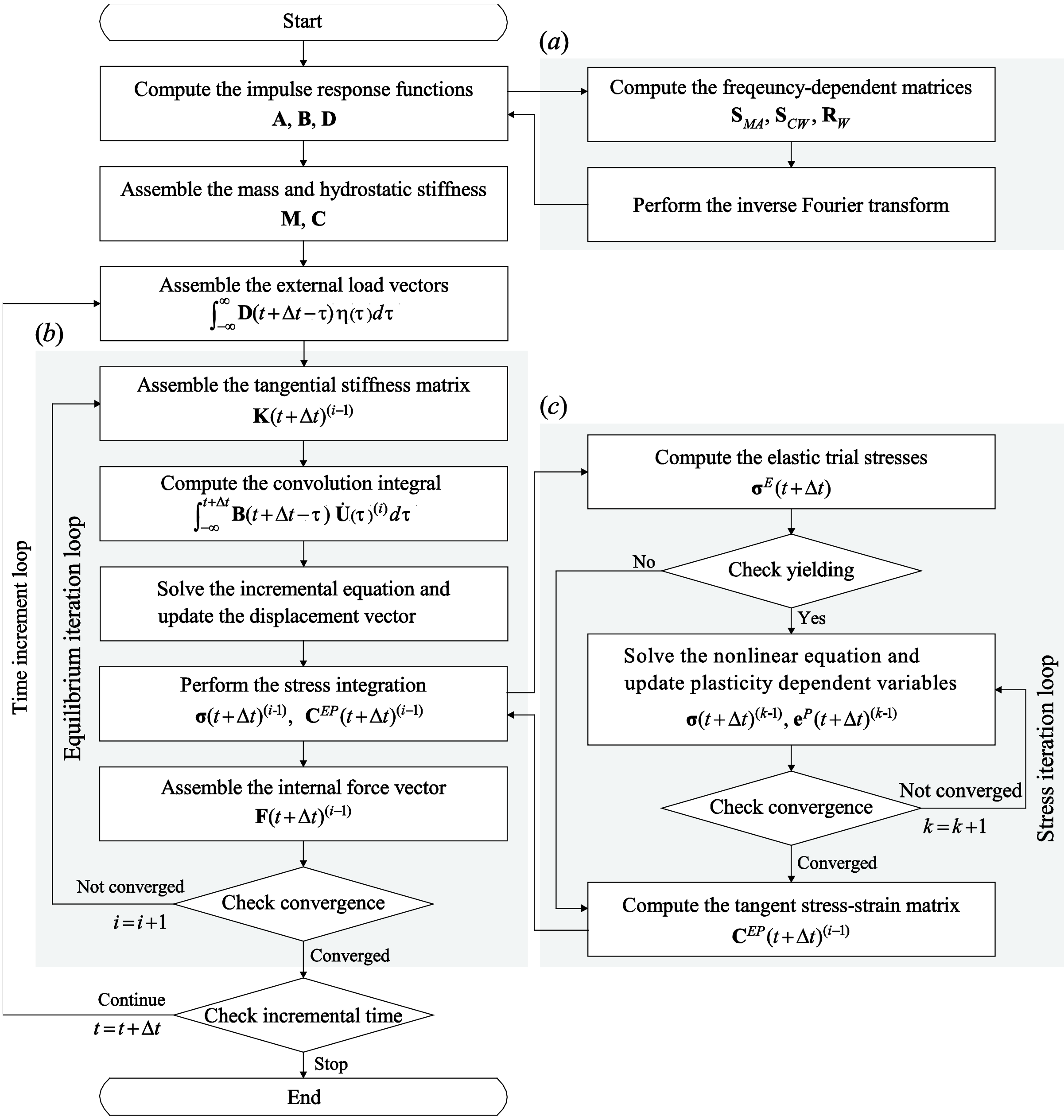

Figure 4.4. Numerical procedure for hydro-elastoplastic analysis: (a) evaluation of impulse response functions, (b) equilibrium iteration loop and (c) stress integration.

(a) Evaluation of the impulse response functions

The impulse response functions are evaluated in the beginning of the procedure, where the piecewise linear function at each node is used for the body boundary condition of the radiation potential as

$$\frac{\partial \phi_k^R}{\partial x_3} = h_k(x_1, x_2)\delta(t) \quad \text{on} \quad S_B \quad \text{at} \quad t = 0\,, \tag{4.27}$$

where ϕ_k^R indicates the radiation potential associated with the unit impulsive velocity at node k, and h_k is the piecewise linear function at node k.

(b) Equilibrium iteration loop

Within each time step, the following iterative procedure is carried out to solve the incremental coupled equations of motion:

$$\begin{aligned}&(\mathbf{M}+\mathbf{A})\ddot{\mathbf{U}}(t+\Delta t)^{(i)} + \int_{-\infty}^{t+\Delta t} \mathbf{B}(t+\Delta t-\tau)\dot{\mathbf{U}}(\tau)^{(i)}d\tau + \left(\mathbf{K}(t+\Delta t)^{(i-1)} + \mathbf{C}\right)\Delta\mathbf{U}^{(i)} \\ &= \mathbf{R}_{S_L}(t+\Delta t) + \int_{-\infty}^{\infty} \mathbf{D}(t+\Delta t-\tau)\eta(\tau)d\tau - \mathbf{C}\mathbf{U}(t+\Delta t)^{(i-1)} - \mathbf{F}(t+\Delta t)^{(i-1)}\,,\end{aligned} \tag{4.28}$$

where the superscript i denotes the iteration number.

After obtaining an incremental solution, the total displacement is updated as follows:

$$\mathbf{U}(t+\Delta t)^{(i)} = \mathbf{U}(t+\Delta t)^{(i-1)} + \Delta\mathbf{U}^{(i)}\,, \quad \mathbf{U}(t+\Delta t)^{(0)} = \mathbf{U}(t)\,. \tag{4.29}$$

The update in the iteration is continued until the convergence within the preset energy tolerance (ε_E) is achieved:

$$\frac{\Delta\mathbf{U}^{(i)^T}\left(\mathbf{R}(t+\Delta t) - \mathbf{F}(t+\Delta t)^{(i-1)} - \mathbf{Q}(t+\Delta t)^{(i-1)}\right)}{\Delta\mathbf{U}^{(1)^T}\left(\mathbf{R}(t+\Delta t) - \mathbf{F}(t) - \mathbf{Q}(t)\right)} \le \varepsilon_E\,, \tag{4.30}$$

where

$$\mathbf{R}(t+\Delta t) = \mathbf{R}_{S_L}(t+\Delta t) + \int_{-\infty}^{\infty} \mathbf{D}(t+\Delta t-\tau)\eta(\tau)d\tau\,, \tag{4.31a}$$

$$\mathbf{Q}(t+\Delta t)^{(i)} = (\mathbf{M}+\mathbf{A})\ddot{\mathbf{U}}(t+\Delta t)^{(i)} + \int_{-\infty}^{t+\Delta t} \mathbf{B}(t+\Delta t-\tau)\dot{\mathbf{U}}(\tau)^{(i)}d\tau + \mathbf{C}\mathbf{U}(t+\Delta t)^{(i)}\,. \tag{4.31b}$$

In addition, the full Newton-Raphson iterative scheme, the composite trapezoidal rule for the convolution integral, and Newmark method for the time integrations [67] are employed and Equation (4.29) is transformed as

$$
\begin{aligned}
&\left\{\frac{1}{\beta\Delta t^2}(\mathbf{M}+\mathbf{A})+\frac{\gamma}{2\beta}\mathbf{B}(0)+\left(\mathbf{K}(t+\Delta t)^{(i-1)}+\mathbf{C}\right)\right\}\Delta\mathbf{U}^{(i)} \\
&=\mathbf{R}_{S_L}(t+\Delta t)-\int_{-\infty}^{\infty}\mathbf{D}(t+\Delta t-\tau)\eta(\tau)d\tau-\mathbf{F}(t+\Delta t)^{(i-1)} \\
&-\int_{-\infty}^{t}\mathbf{B}(t+\Delta t-\tau)\dot{\mathbf{U}}(\tau)d\tau-\frac{\Delta t}{2}\mathbf{B}(\Delta t)\dot{\mathbf{U}}(t)-\mathbf{C}\mathbf{U}(t+\Delta t)^{(i-1)} \\
&-(\mathbf{M}+\mathbf{A})\left\{\frac{1}{\beta\Delta t^2}\left(\mathbf{U}(t+\Delta t)^{(i-1)}-\mathbf{U}(t)\right)-\frac{1}{\beta\Delta t}\dot{\mathbf{U}}(t)-\left(\frac{1}{2\beta}-1\right)\ddot{\mathbf{U}}(t)\right\} \\
&-\frac{\Delta t}{2}\mathbf{B}(0)\left\{\frac{\gamma}{\beta\Delta t^2}\left(\mathbf{U}(t+\Delta t)^{(i-1)}-\mathbf{U}(t)\right)-\left(\frac{\gamma}{\beta}-1\right)\dot{\mathbf{U}}(t)-\frac{\Delta t}{2}\left(\frac{\gamma}{2}-2\right)\ddot{\mathbf{U}}(t)\right\},
\end{aligned}
\tag{4.32}
$$

in which β and γ parameters in the Newmark method, which can be determined to obtain integration accuracy and stability.

(c) Stress integration

In equilibrium iterations, the element stress $\boldsymbol{\sigma}(t+\Delta t)^{(i-1)}$ for the calculation of the nodal point force vector $\mathbf{F}(t+\Delta t)^{(i-1)}$ and the elastoplastic stress-strain matrix $\mathbf{C}^{EP}(t+\Delta t)^{(i-1)}$ to calculate the tangential stiffness matrix $\mathbf{K}(t+\Delta t)^{(i-1)}$ are evaluated using the total strains $\mathbf{e}(t+\Delta t)^{(i-1)}$ with known stress and strain at time t.

In the following subsections, the numerical solution procedure to calculate the impulse response functions and to integrate stress are described in detail.

4.2.1 Impulse Response Functions

Using the Fourier transform, the impulse response functions are obtained from the following relations:

$$\mathbf{A}(\infty)-\mathbf{S}_{MA}(\omega)=\frac{1}{\omega}\int_0^{\infty}\mathbf{B}(\tau)\sin(\omega\tau)d\tau, \tag{4.33a}$$

$$\mathbf{S}_{CW}(\omega)=\int_0^{\infty}\mathbf{B}(\tau)\cos(\omega\tau)d\tau, \tag{4.33b}$$

$$\mathbf{B}(t)=\frac{2}{\pi}\int_0^{\infty}\omega\left[\mathbf{A}(\infty)-\mathbf{S}_{MA}(\omega)\right]\sin(\omega t)d\omega, \tag{4.33c}$$

$$\mathbf{B}(t) = \frac{2}{\pi}\int_0^\infty \mathbf{S}_{CW}(\omega)\cos(\omega t)d\omega\,, \tag{4.33d}$$

$$\mathbf{D}(t) = \frac{1}{\pi}\int_0^\infty \left[\mathrm{Re}\left(\mathbf{R}_W(\omega)\right)\cos(\omega t) - \mathrm{Im}\left(\mathbf{R}_W(\omega)\right)\sin(\omega t))\right]d\omega\,, \tag{4.33e}$$

where $\mathbf{S}_{MA}$, $\mathbf{S}_{CW}$, and $\mathbf{R}_W$ are the added mass and radiated wave damping matrices and the wave excitation force vector at a frequency ω. The three frequency-dependent matrices are obtained adopting the direct coupling method for hydroelastic analysis of plate structures, see Section 2.2. Note that the Filon quadrature [89] is employed to perform the numerical integrations in Equation (4.33), in which higher frequency terms are neglected after convergence tests [90].

The added mass at infinite frequency $\mathbf{A}(\infty)$ can be computed by solving the boundary value problem for the velocity potential ψ_k. The boundary integral equations for the infinite depth case are given by

$$\int_{S_B} \psi_k(\boldsymbol{\xi}) \frac{\partial^2}{\partial x_3 \partial \xi_3}\left(\frac{1}{\sqrt{r^2 + (x_3 - \xi_3)^2}}\right) dS_\xi = 2\pi h_k(x_1, x_2) \quad \text{for } \mathbf{x} \text{ on } S_B \text{ at } t = 0\,. \tag{4.34}$$

For the boundary element approximations, Equation (4.34) is multiplied by a test function $\delta\psi$, and integrated over the wet surface S_B. Then, the following equation are obtained:

$$\int_{S_B}\int_{S_B} \psi_k(\boldsymbol{\xi}) \frac{\partial^2}{\partial x_3 \partial \xi_3}\left(\frac{1}{\sqrt{r^2 + (x_3 - \xi_3)^2}}\right) dS_\xi \delta\psi dS_x = 2\pi \int_{S_B} h_k \delta\psi dS_x\,. \tag{4.35}$$

If ψ_k is calculated by using the boundary element method, and then substituted into the Equation (4.26b), the added mass at infinite frequency $\mathbf{A}(\infty)$ can be computed.

4.2.2 Stress Integration

For a given current strain state, we update the stress, plastic strain and other internal variables related to the plastic behavior by adopting the implicit return mapping algorithm [82, 83, 91]. In this procedure, the elastic trial stress state, which is obtained under the assumption of only elastic deformation having occurred in the time step, returns to the yield surface by solving a nonlinear equation derived from the plate state-projected von Mises model. The Newton-Raphson method is employed to solve the nonlinear equation. Then, the elastoplastic stress-strain tensor is consistent with the return mapping procedure.

In order to obtain the internal force vector and tangential stiffness matrix, the evaluations of the stress and the elastoplastic stress-strain tensors are performed at all integration points of the plate finite element. For better accuracy in hydro-elastoplastic analysis, higher order integrations are required, in particular, through thickness direction.

4.3 Numerical Examples

In this section, to investigate the capability of the proposed numerical procedure, numerical examples are solved and the solutions are compared with available experimental results and numerical results obtained with commercial software. In all the numerical examples, the water depth is assumed to be infinite, the density of water ρ_w is $1000kg/m^3$ and the acceleration of gravity g is $9.8m/s^2$. The convergence tolerance for the equilibrium iteration in each time step is assigned to $\varepsilon_E = 10^{-6}$ in Equation (4.30).

Since there are no available previous numerical and experimental results for the elastoplastic behavior of floating plate structures, the numerical results with those obtained using LS-DYNA 971 R7.1.1, a well-known commercial software useful for nonlinear dynamic problems, are compared. First, to validate the proposed numerical procedure and the modeling procedure of LS-DYNA for hydroelastic analysis in time domain, a hydroelastic experiment conducted by Endo and Yago [16] is considered. This experiment has been dealt with many times before (see e.g. Reference [84, 85]).

As shown in **Figure 4.5(a),** a floating plate structure is subjected to an impact load induced by a weight of 196N dropped on a hit point. **Table 4.1** presents the details of the floating plate structures used for the experiments. **Figure 4.5(b)** shows the impact load curve during the weight drop.

Table 4.1. Details of the floating plate model for the weight drop test.

Parameter	Value
Length (L)	$9.75m$
Width (B)	$1.95m$
Thickness(H)	$0.0545m$
Draft (d)	$0.0163m$
Water depth(h)	$1.9m$
Bending stiffness per unit width (EI/B)	$8985.62Nm$
Dimensionless bending stiffness (S)	2.029×10^{-5}

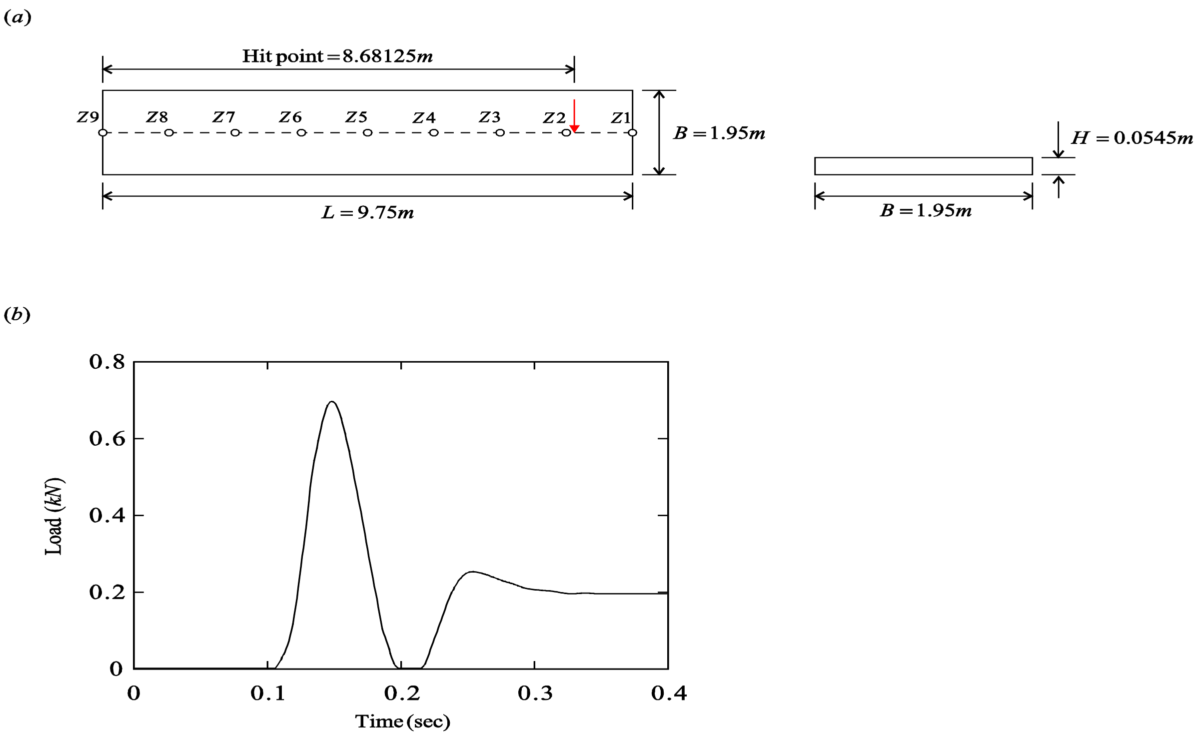

Figure 4.5. Floating plate structure subjected to a weight drop impact: (a) problem description and (b) impact load curve.

The plate structure shown in **Figure 4.6(a)** is modeled by a 24 (in length) × 4 (in breadth) mesh of plate finite elements, and the same mesh is used for the fluid boundary elements on the interface boundary surface calculating frequency-dependent matrices. The time step size is chosen as $\Delta t = 0.001$ for a duration of 2.5s.

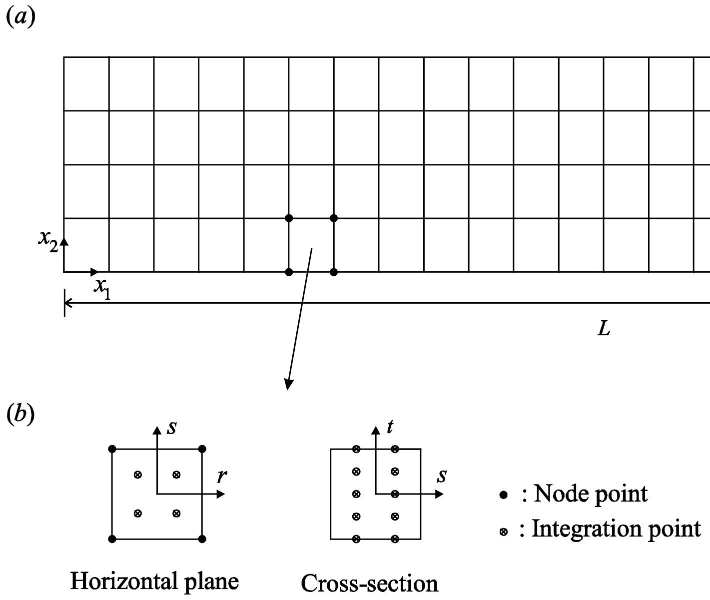

Figure 4.6. Discretization and integration points of the floating plate structure: (a) finite and boundary element meshes and (b) integration points in an element.

In LS-DYNA, shell elements (48×8) and 3D solid elements ($480 \times 80 \times 72$) are used for modeling the plate structure and surrounding fluid, respectively, for which the multi-material arbitrary Lagrangian-Eulerian (MMALE) method is applied. The fluid - structure interaction is treated via a constraint formulation referred to as the "Constrained Lagrange in Solid," and an explicit time integration is used. **Figure 4.8** illustrates the numerical model used in LS-DYNA.

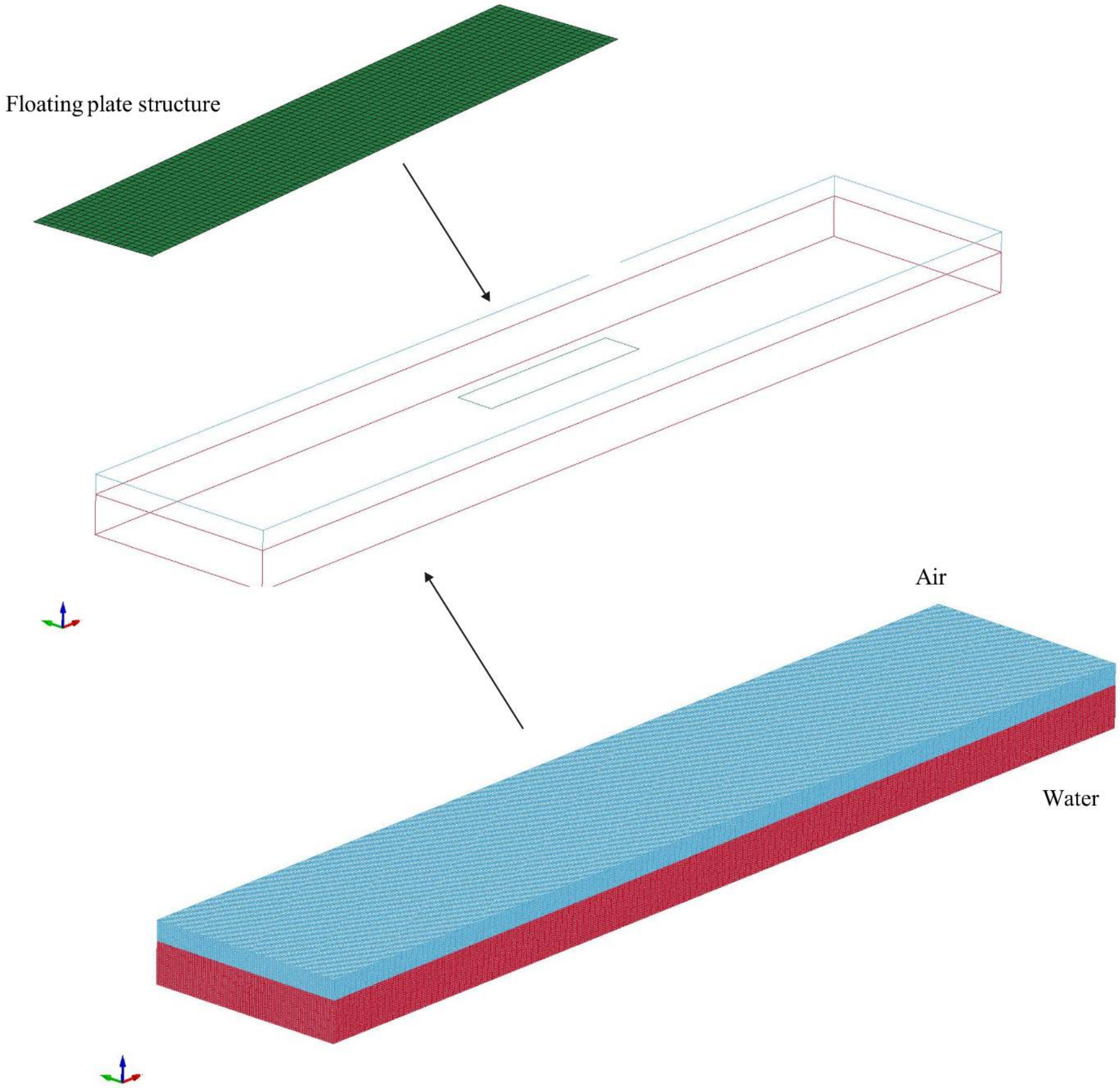

Figure 4.7. Numerical model of a plate structure floating on water in LS-DYNA.

Figure 4.8 shows the deflections obtained using the present numerical procedure and LS-DYNA, and the results are compared with the measurements of the experiment at points Z1– Z9 indicated in **Figure 4.5(a)**. The numerical results are in good agreement with the measurements.

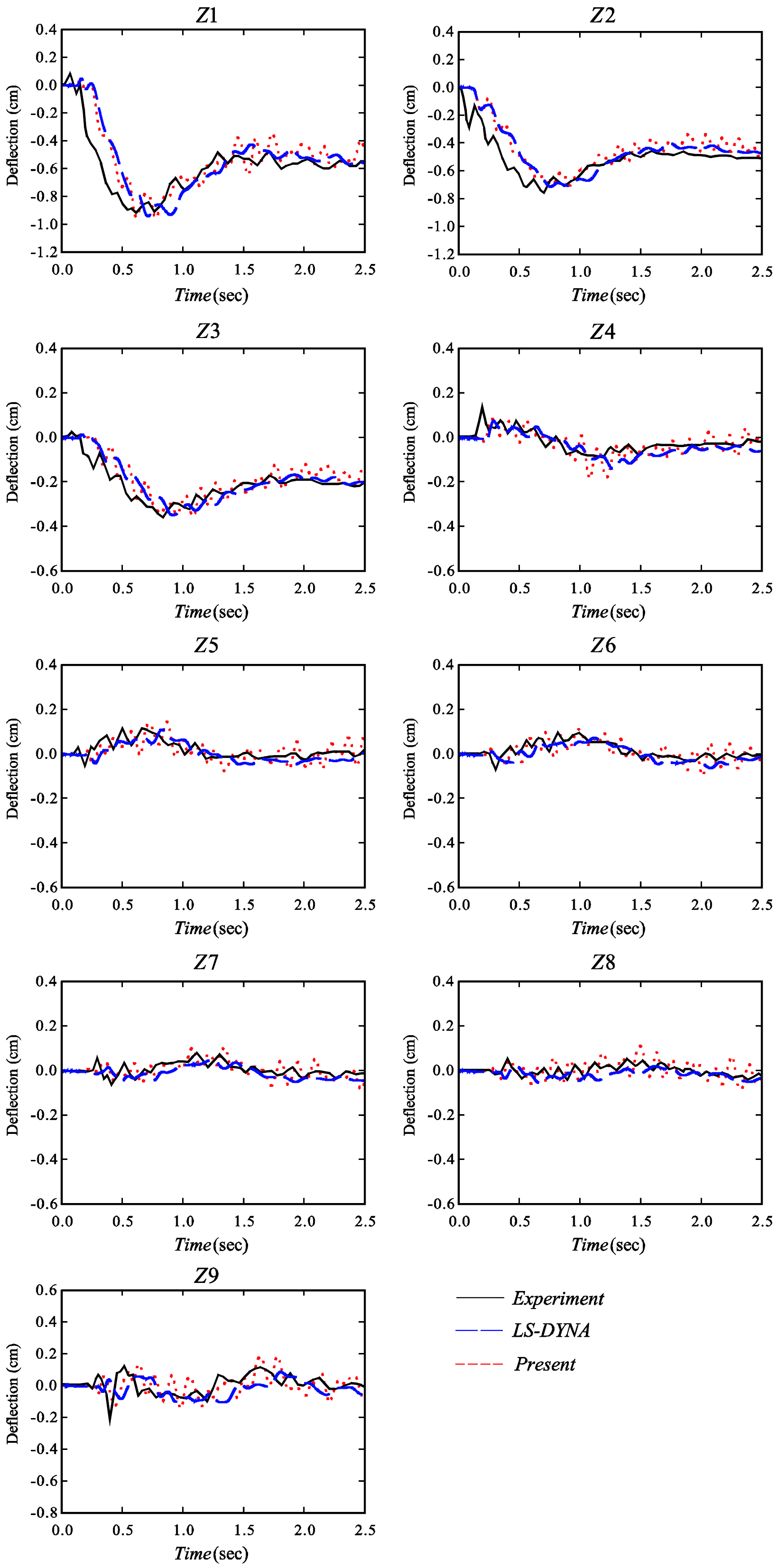

Figure 4.8. The time histories of deflections at points Z1-Z9 in the hydroelastic problem

Then, the hydro-elastoplastic analysis of the floating plate structure is conducted. In order to obtain the reference solutions for the hydro-elastoplastic problem, an elastic-perfectly-plastic material of yield stress $\sigma_y = 30kN/m^2$ is considered. In the present numerical procedure, a 48×8 mesh of plate finite elements is used. In each plate element, a 2×2 Gauss integration is employed in the element plane (*r*-*s* plane) and a 5-point Newton-Cotes integration is used in the thickness direction (*t*-direction), as shown in **Figure 4.6(b)**. In LS-DYNA, the same numerical integration is used in the element plane, but the 5-point Lobatto integration is used in the thickness direction. **Figure 4.9** illustrates the deflections calculated at points Z1–Z9 using the present numerical procedure and LS-DYNA.

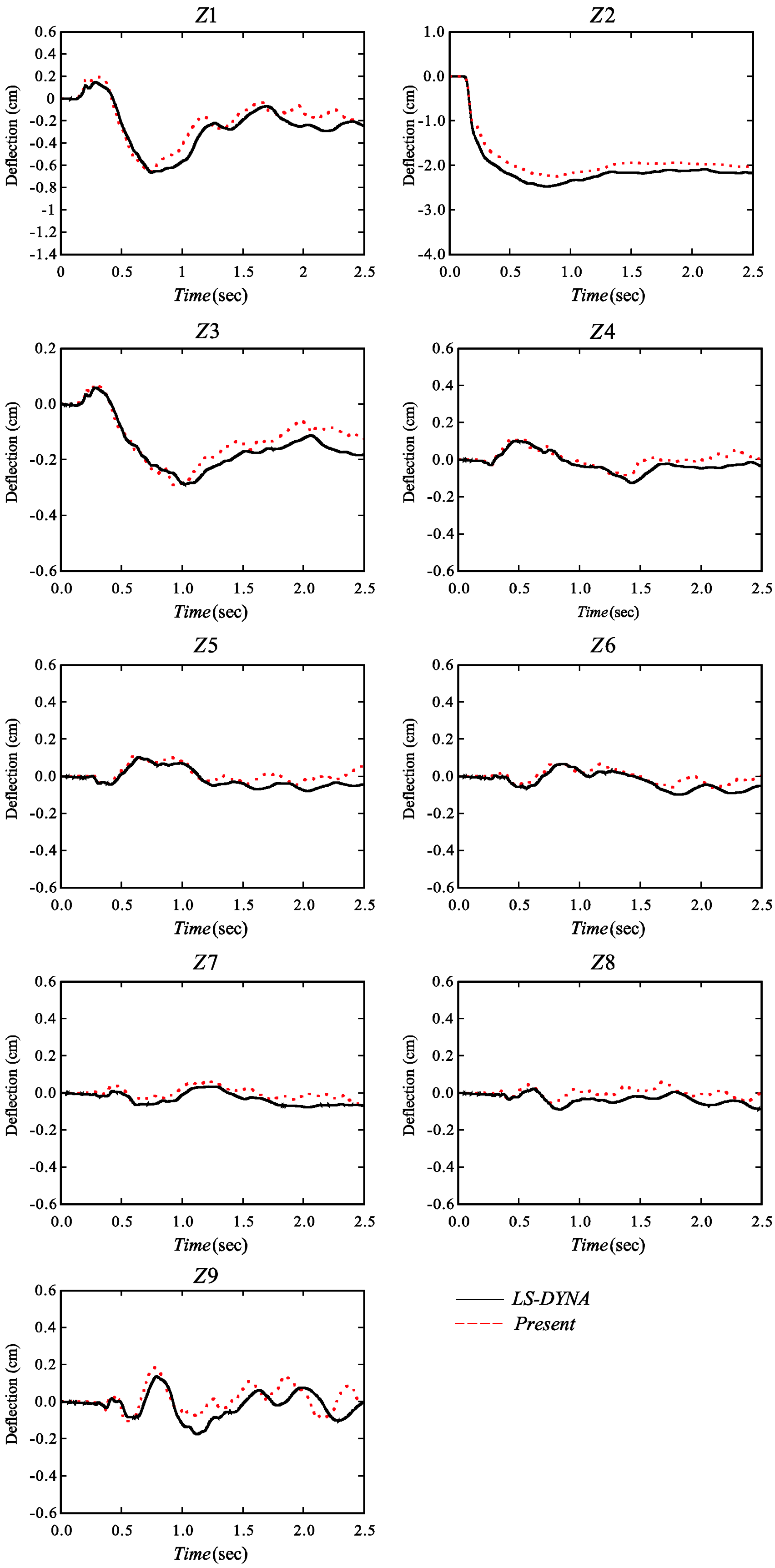

Figure 4.9. The time histories of deflections at points Z1-Z9 in the hydro-elastoplastic problem.

Figure 4.10 depicts the distributions of the effective plastic strain at the top surface of the floating plate structure. The results of the present numerical procedure are in good agreement with the reference solutions obtained using LS-DYNA.

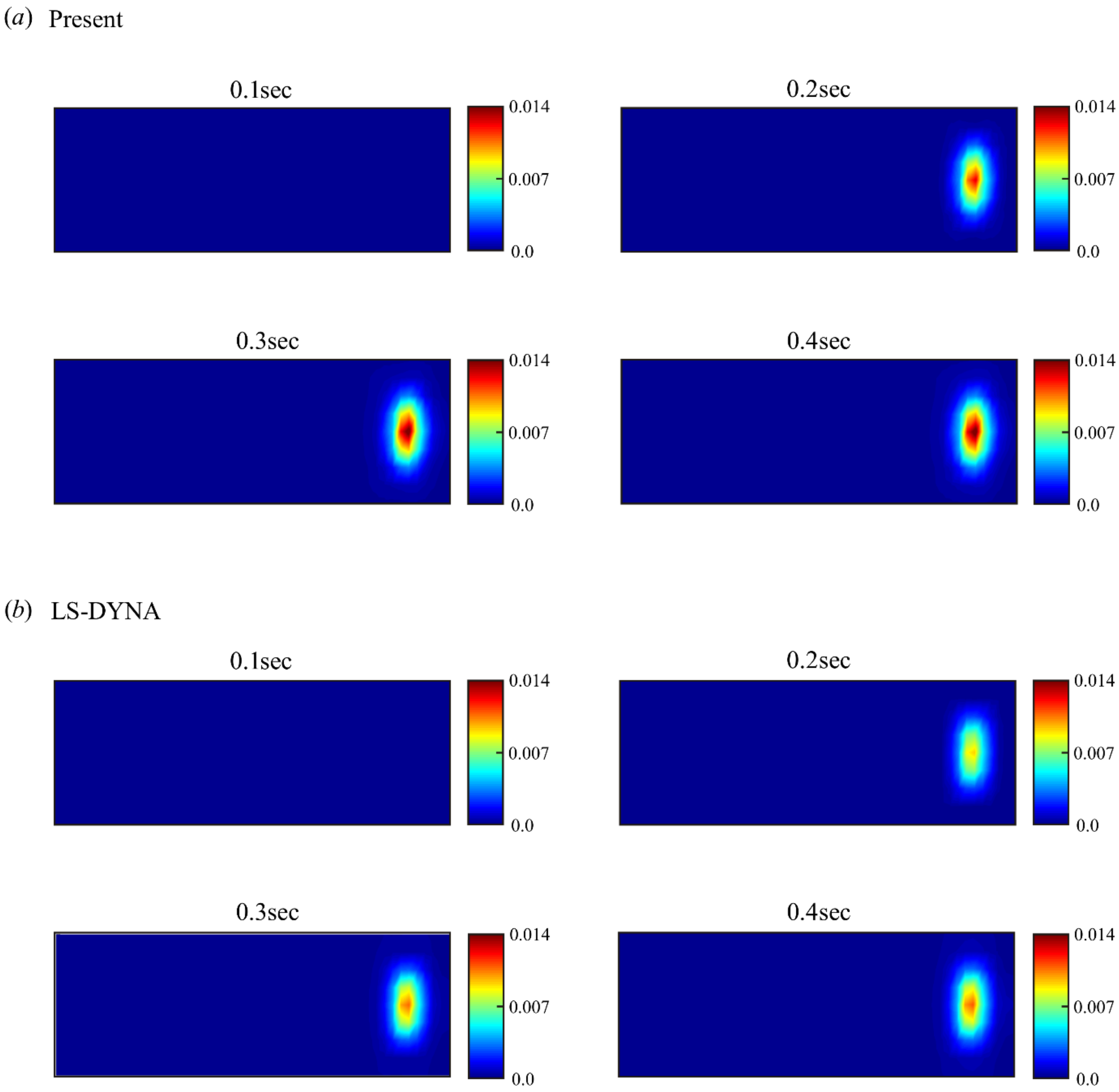

Figure 4.10. Distributions of effective plastic strain at the top surface of the floating plate structure: for (a) the proposed numerical method and (b) LS-DYNA.

Table 4.2 lists the computation times required using a personal computer (Intel(R) core(TM) i7-2600 3.40GHz CPU, 16 GB RAM) for the present numerical procedure and a high performance computer (5.3TFLOPS, 248 CPUs - Intel Xeon 2.60GHz, 2TB RAM) of Korea National Institute of Supercomputing and Networks for LS-DYNA. The Massively Parallel Processing (MPP) with 16 CPUs is employed in LS-DYNA. The computational efficiency of the present numerical procedure is presented in **Table 4.2**.

Table 4.2. Computational times for the hydro-elastoplastic problem in Figure 4.5.

	Items	[hr]	Ratio [%]
Present (performed in PC)	Evaluation of impulse response functions	1.252	43.685
	Performance of the time increment loop	1.614	56.315
	Total	2.866	100.000
LS-DYNA (performed in a high performance computer)	Element processing	2.581	90.056
	ALE Advection	11.86	413.817
	Other	0.934	32.589
	Total	15.375	536.462

4.4 Closure

In this chapter, a nonlinear formulation for the hydro-elastoplastic analysis of floating plate structures is presented, in which the convolution integral was employed to couple elastoplastic deformation and water waves in the time domain. The present formulation can describe the interactions between fluids and structures with material nonlinearity. The fluid is discretized using the boundary element method, and the impulse response functions are obtained from the corresponding frequency-dependent metrics using the Fourier transformation. The plastic behavior of the floating plates is simulated using an implicit return mapping algorithm based on the finite element method. The capability of the proposed numerical procedure was investigated through comparisons with the numerical results of LS-DYNA.

Chapter 5. Performance of the Numerical Method for Hydro-elastoplastic Analysis

5.1 Hydrodynamic Problems for Floating Plate Structures in Two Dimensions

Figure 5.1 illustrate a plate structure, which is assumed to be infinite in the x_2 direction, floating on water of constant finite depth h subjected to external loads (impact and wave). To solve the problem, the time-domain incremental coupled equations (4.24) is discretized by using the 2-node Hermitian beam element based on the Euler-Bernoulli beam theory. On the other hand, the impulse response functions for hydrodynamic forces is obtained from the corresponding frequency-dependent metrics in the direct coupling method in two dimensions, in which the fluid is discretized by using 2-node boundary element.

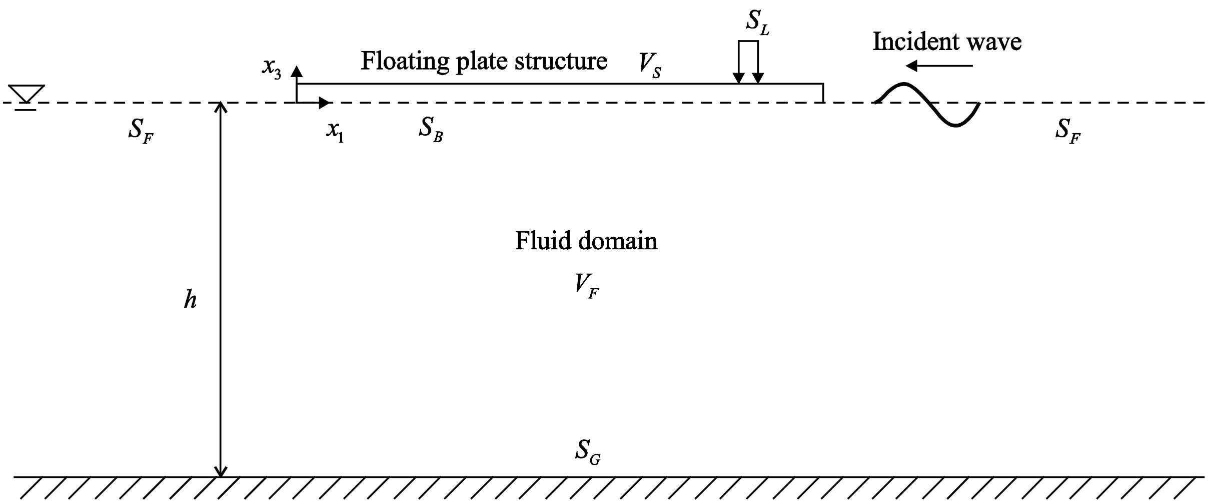

Figure 5.1. A floating plate structure in two dimensional fluid domain.

The plastic behavior of the floating plate structures is simulated by using an implicit return mapping algorithm, which is summarized in **Table 5.1**.

Table 5.1. Implicit return mapping algorithm for the von Mises model with isotropic hardening

1. Calculate elastic trial stress state. Given total strain tensor $e_{ij}(t+\Delta t)$ and state variables at time t.

$$S_{ij}^{E}(t+\Delta t) = 2G\left[e_{ij}(t+\Delta t) - \frac{1}{3}e_{kk}(t+\Delta t)\delta_{ij} - e_{ij}^{P}(t)\right]$$

$$\overline{\sigma}^{E}(t+\Delta t) = \sqrt{\frac{3}{2}S_{ij}^{E}(t+\Delta t)S_{ij}^{E}(t+\Delta t)}$$

$$f_{y}^{E}(t+\Delta t) = \overline{\sigma}^{E}(t+\Delta t) - \sigma_{y}\left[\overline{e}^{P}(t)\right]$$

2. Check for yielding

If $f_{y}^{E}(t+\Delta t) \le 0$ then $S_{ij}^{E}(t+\Delta t) = S_{ij}(t+\Delta t)$, $\Delta\overline{e}^{P} = 0$, and exit.

Else then $\Delta\overline{e}^{P} > 0$, and next

3. Solve the nonlinear equation f_n using iterative method - Return mapping

$$f_{n}(\Delta\overline{e}^{P}) = \frac{\overline{\sigma}^{E}(t+\Delta t)}{\left[\sigma_{y}(t+\Delta t) + E\Delta\overline{e}^{P}\right]} - 1 = 0$$

4. Update state variables

$$\Delta\chi = \frac{3}{2}\frac{\Delta\overline{e}^{P}}{\sigma_{y}\left[\overline{e}^{P}(t+\Delta t)\right]}$$

$$S_{ij}(t+\Delta t) = \frac{S_{ij}^{E}(t+\Delta t)}{1+2G\Delta\chi}$$

$$\sigma_{ij}(t+\Delta t) = S_{ij}(t+\Delta t) + \frac{1}{3}\sigma_{kk}(t+\Delta t)\delta_{ij}$$

$$e_{ij}^{P}(t+\Delta t) = e_{ij}^{P}(t) + \Delta\chi S_{ij}(t+\Delta t)$$

5. Calculate elastoplastic stress-strain tensor

$$C_{ijkl}^{EP}(t+\Delta t) = \frac{\partial\sigma_{ij}(t+\Delta t)}{\partial e_{kl}(t+\Delta t)}$$

In this section, several numerical examples for investigating the performance and capability of the proposed numerical procedure for hydro-elastoplastic analysis of a floating plate structure in two dimension. First, the previous numerical studies for the time-dependent motion of a floating elastic plate structure is considered. And then, second problem is the hydrodynamic responses of an elastoplastic beam subjected to two load cases: (I) an impact load and (II) an incident wave load. In all the numerical examples, convergence tolerance for the equilibrium iteration in each time step is assigned to $\varepsilon_E = 10^{-6}$.

5.1.1 Benchmark Problems for Transient Hydroelastic Responses

A series of benchmark calculations for the time-dependent motion of a floating elastic plate structure released from rest is solved and compare the results with those obtained by Meylan and Sturova[[92]. **Table 5.2** presents a numerical model of the plate structure, which is considered by them.

Table 5.2. Details of the floating plate model of benchmark problems for the time-dependent motion of a floating elastic plate structure released from rest

Parameter	Value
Length (L)	$1m$
Width (B)	$1m$
Structural density (ρ_s)	$12.25 kg/m^3$
Dimensionless bending stiffness (S)	0.005

Two different initial condition and several water depth cases are considered. First, a symmetric displacement is given by

$$u_3(\mathbf{x};0) = \frac{1}{2}\left[1+\cos(2\pi(x-L/2)/L)\right], \tag{5.1}$$

and second, a non-symmetric displacement is given by

$$u_3(\mathbf{x};0) = \begin{cases} 0 & 0<x<L/2 \\ \frac{1}{2}\left[1+\cos(2\pi(2(x-L/2)/L-1/2))\right] & L/2<x<L \end{cases}. \tag{5.2}$$

There are the six different benchmark problems for the motion of floating plate structures as five water depth cases ($h/L = 0.02$, 0.04, 2.0, 4.0, and 8.0) with symmetric initial displacement and one water depth ($h/L = 0.02$) non-symmetric initial displacement. Solutions of the proposed numerical procedure were in good agreement with the reference solutions as shown **Figures 5.2 ~ 5.7**.

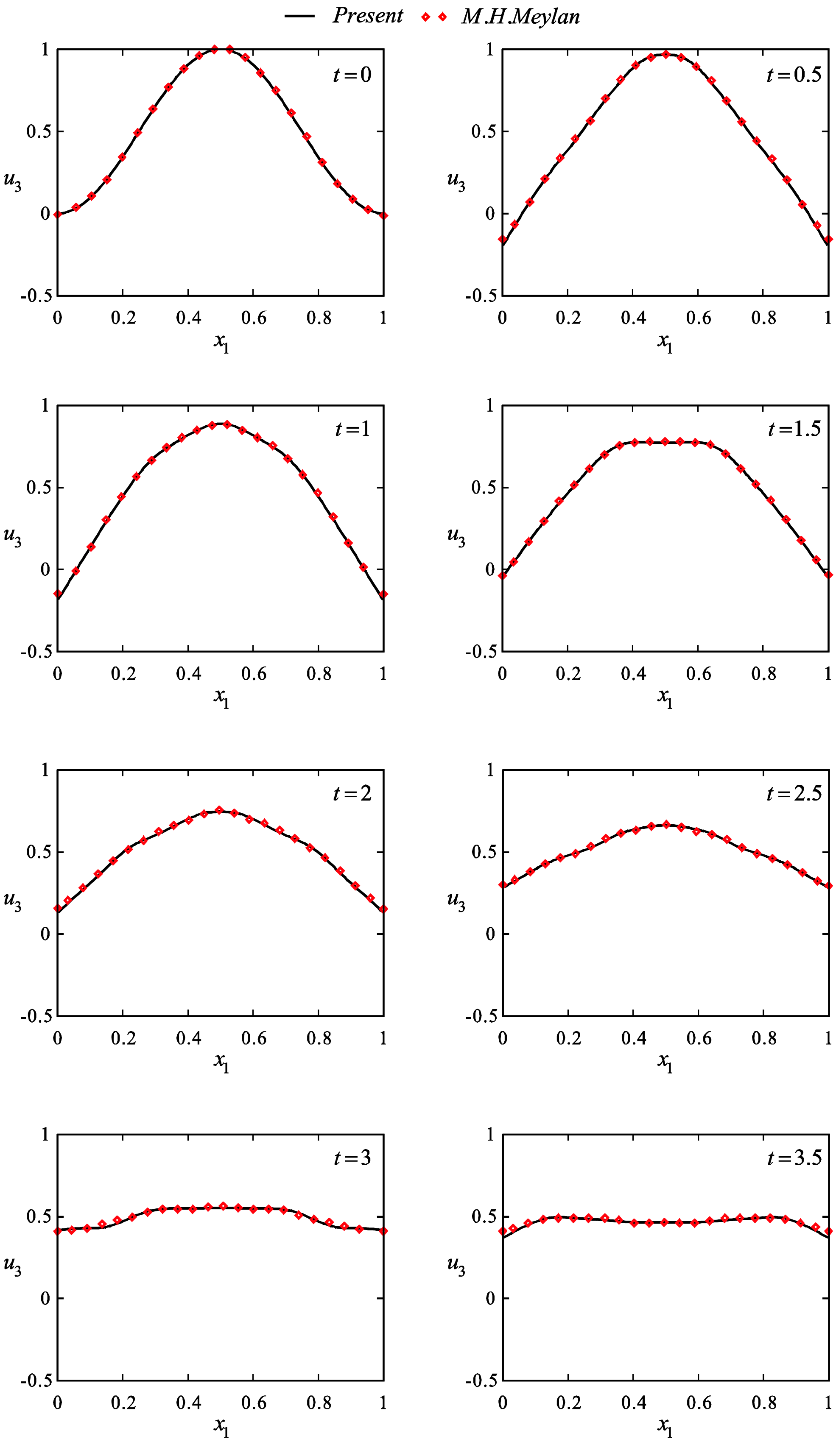

Figure 5.2. Time history of deflections over the floating elastic plate structure with symmetric initial displacement for $h/L = 0.02$.

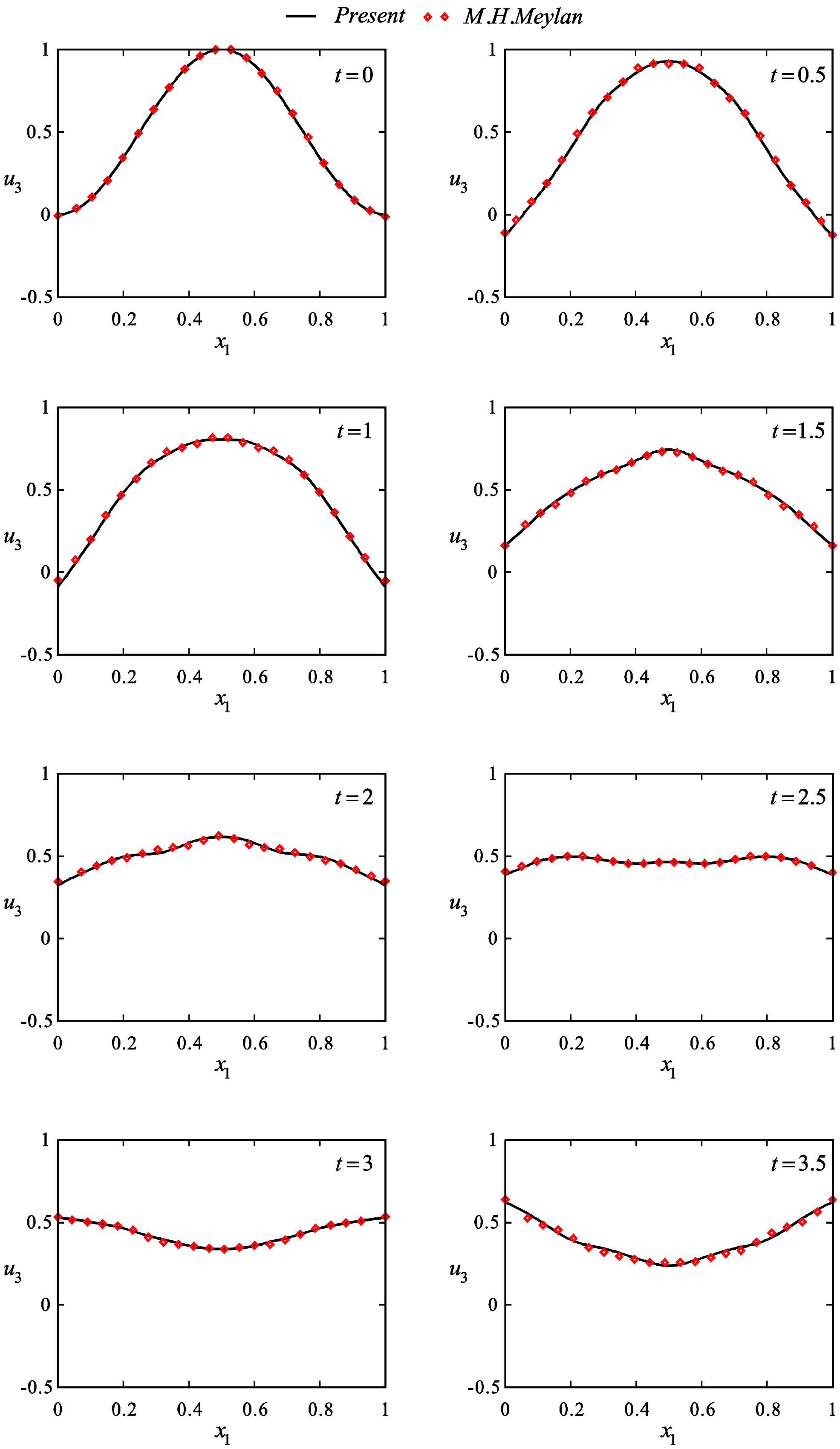

Figure 5.3. Time history of deflections over the floating elastic plate structure with symmetric initial displacement for $h/L = 0.04$.

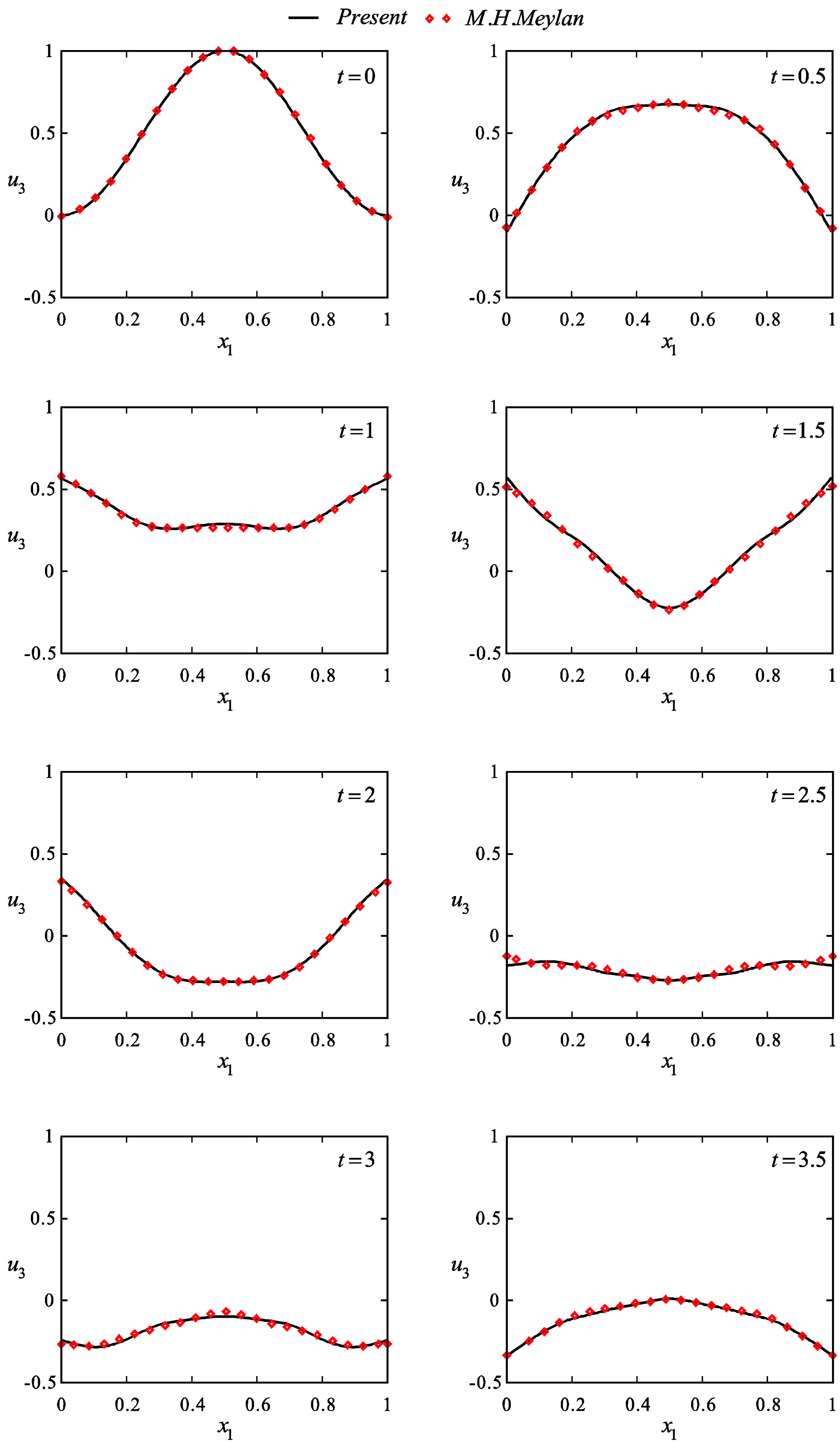

Figure 5.4. Time history of deflections over the floating elastic plate structure with symmetric initial displacement for $h/L=2$.

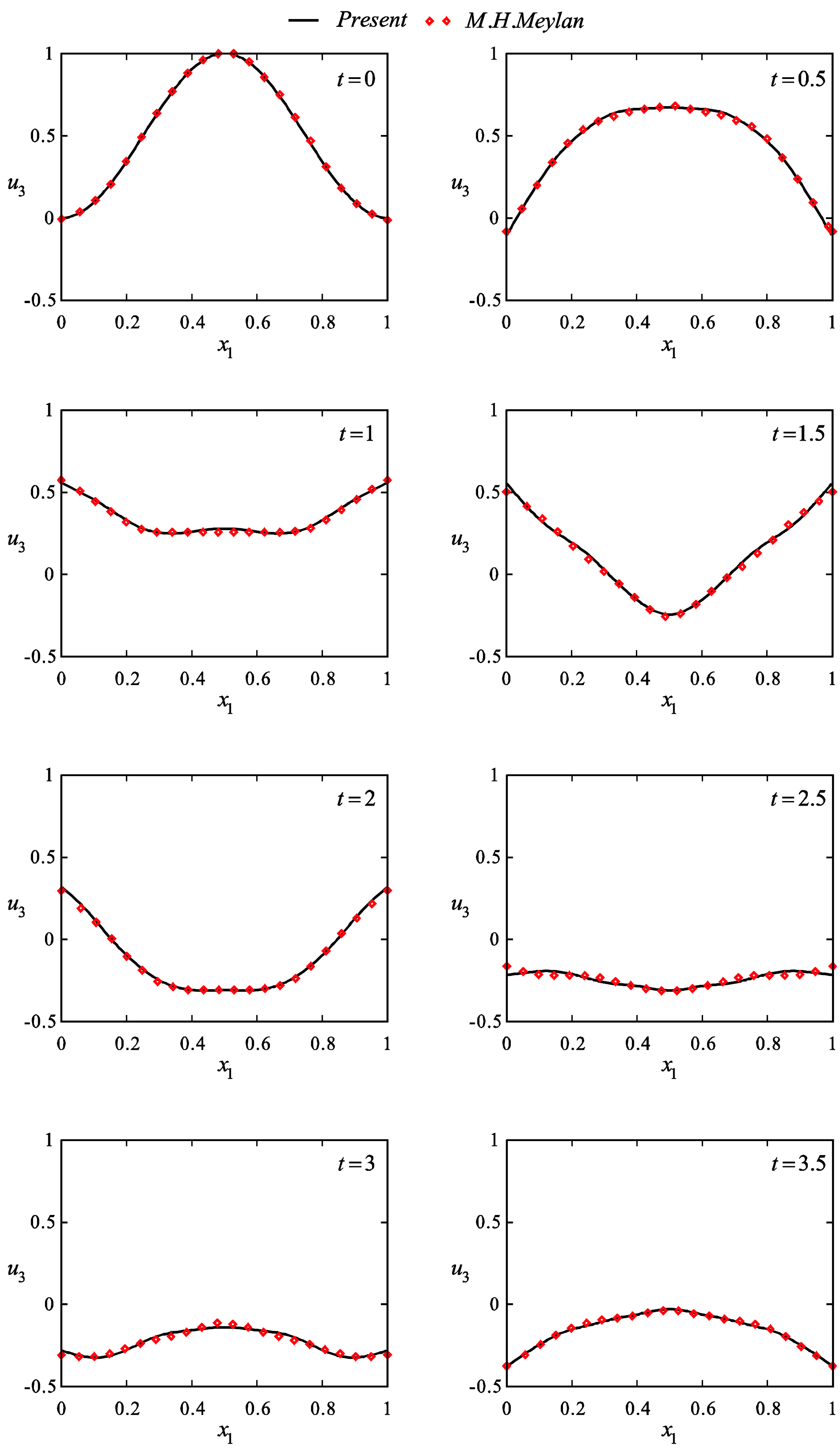

Figure 5.5. Time history of deflections over the floating elastic plate structure with symmetric initial displacement for $h/L=4$.

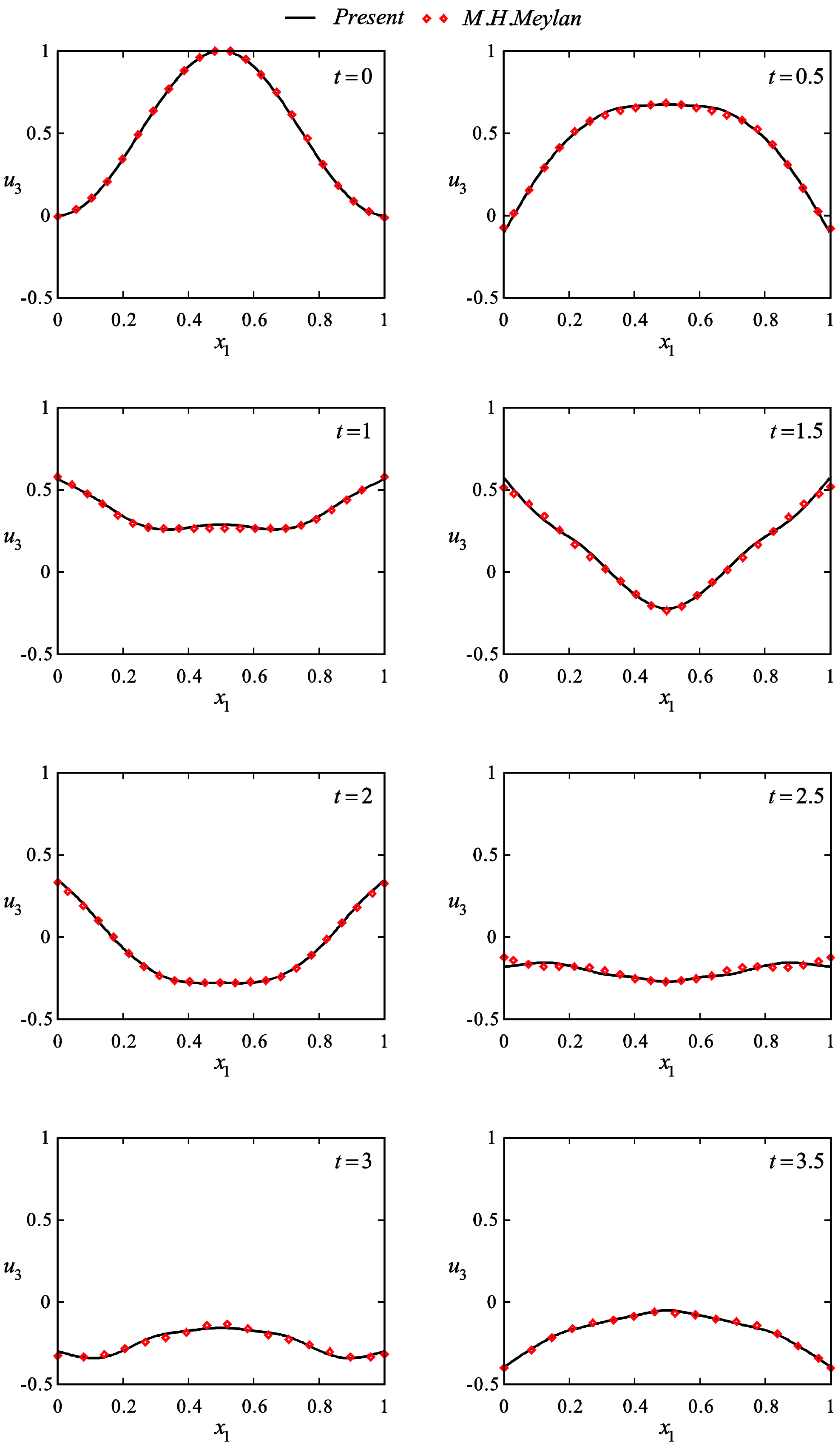

Figure 5.6. Time history of deflections over the floating elastic plate structure with symmetric initial displacement for $h/L = 8$.

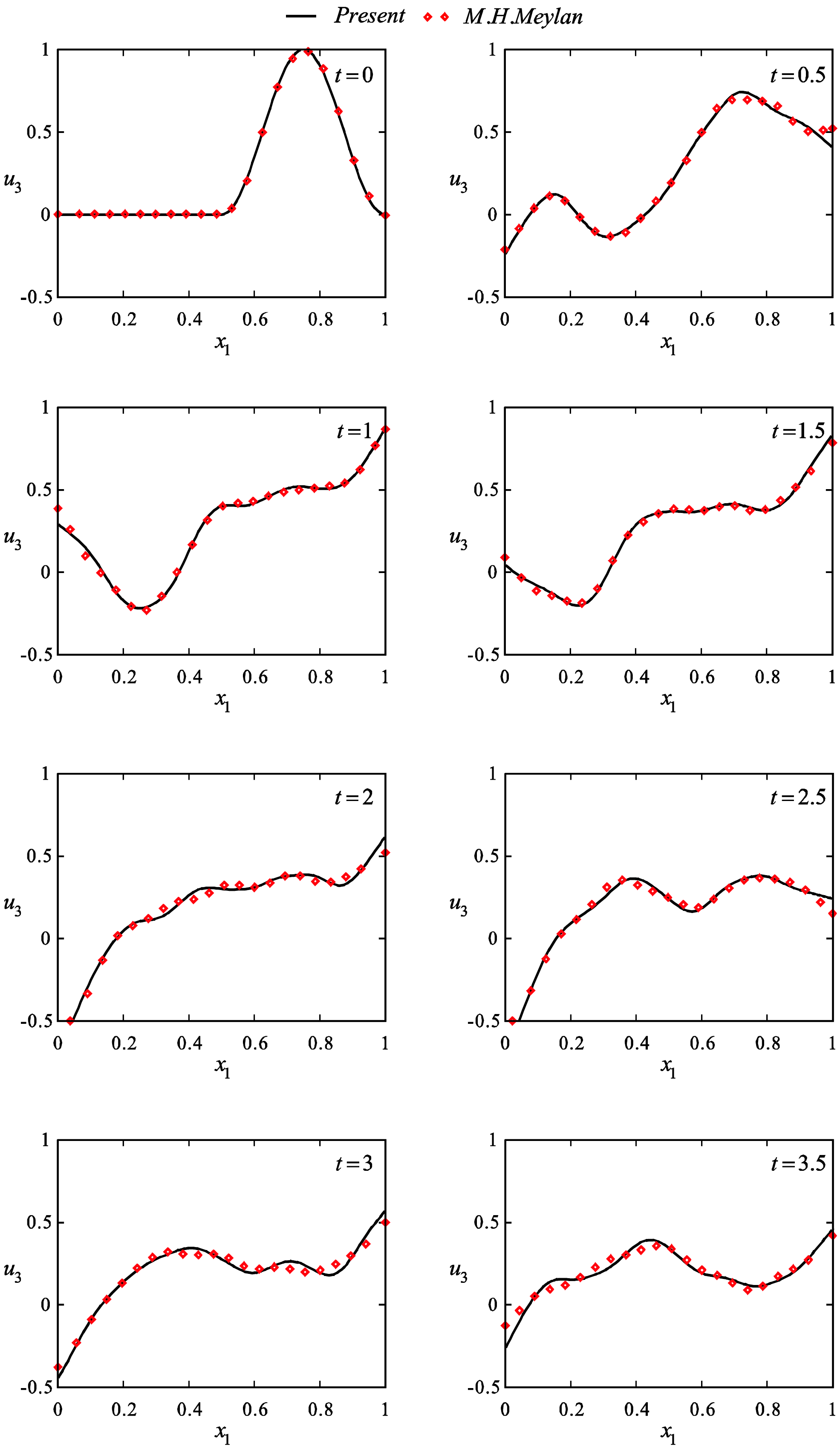

Figure 5.7. Time history of deflections over the floating elastic plate structure with non-symmetric initial displacement for $h/L = 0.02$.

Then, the hydro-elastoplastic analysis for the benchmark problems is performed. In order to obtain the reference solutions for the hydro-elastoplastic problem, the bilinear isotropic hardening model (yield stress $\sigma_y = 10kpa$ and plastic hardening modulus $E_P = 0.1E$) is adopted. The deflections over the floating elastic plate structure calculated at 0.5 sec intervals by using hydroelastic and hydro-elastoplastic analyses are depicted in following **Figures 5.8 ~ 5.13**.

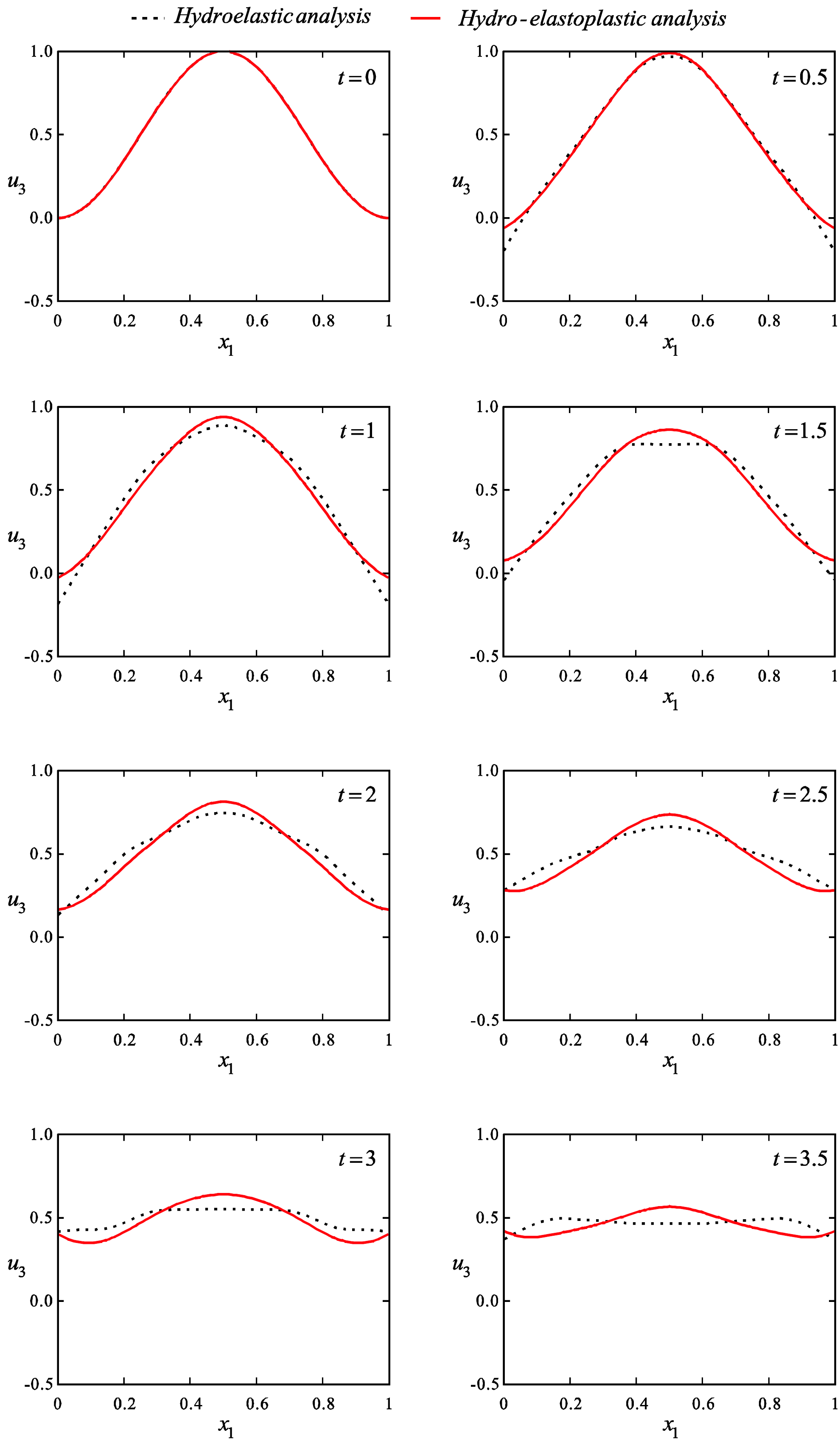

Figure 5.8. Time histories of deflections over the floating elastoplastic plate structure with symmetric initial displacement for $h/L = 0.02$.

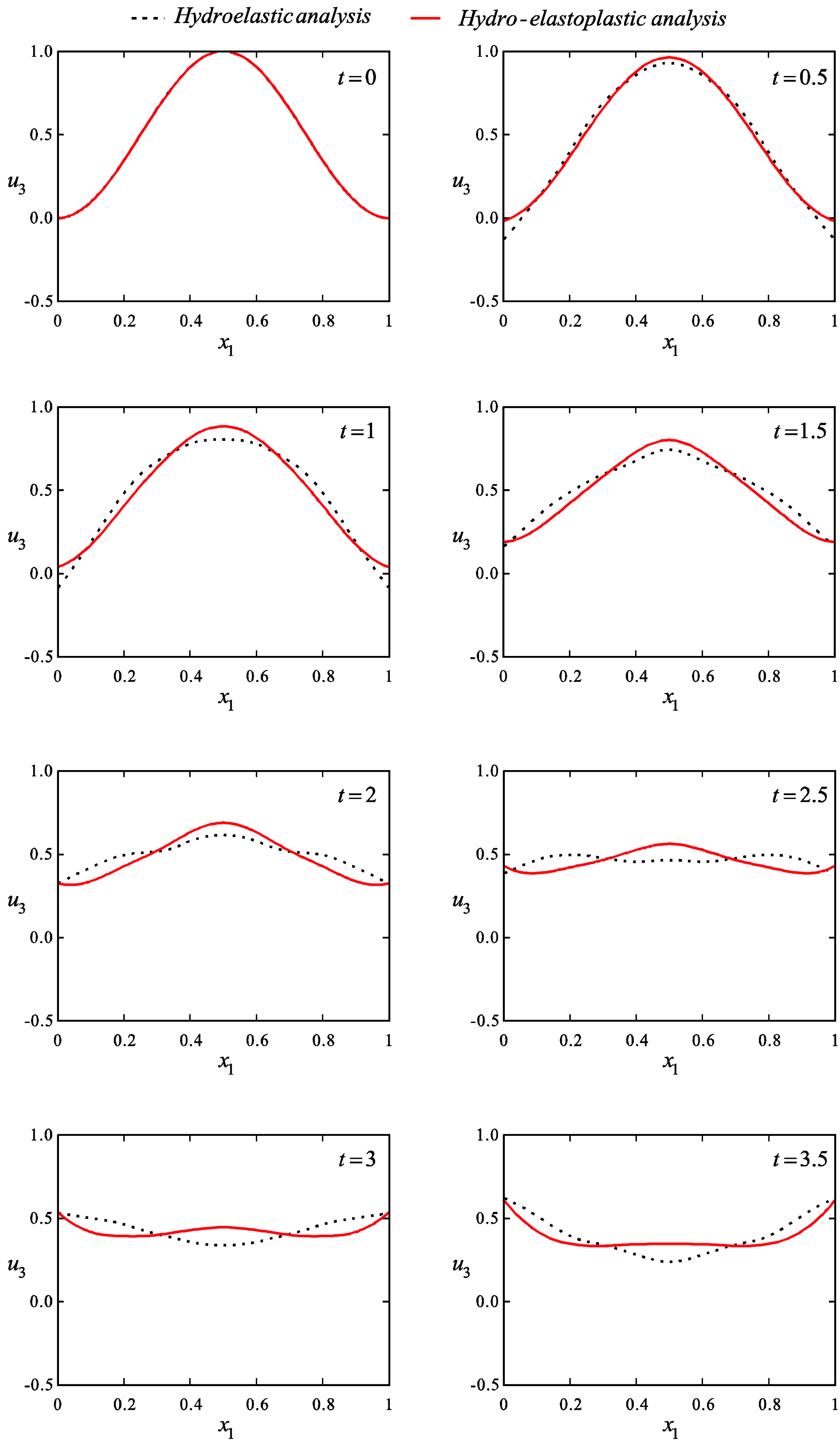

Figure 5.9. Time histories of deflections over the floating elastoplastic plate structure with symmetric initial displacement for $h/L = 0.04$.

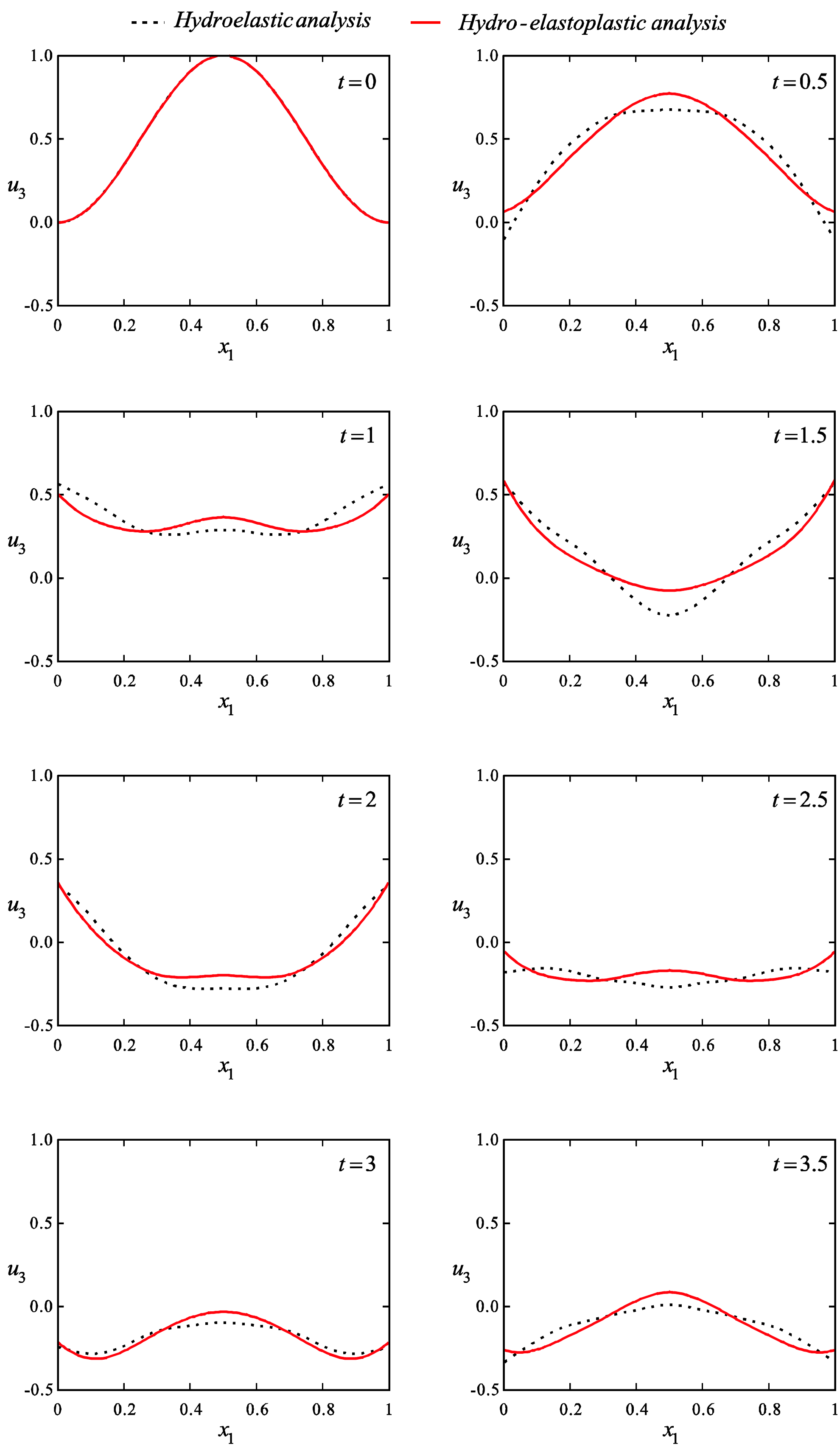

Figure 5.10. Time histories of deflections over the floating elastoplastic plate structure with symmetric initial displacement for $h/L = 2$.

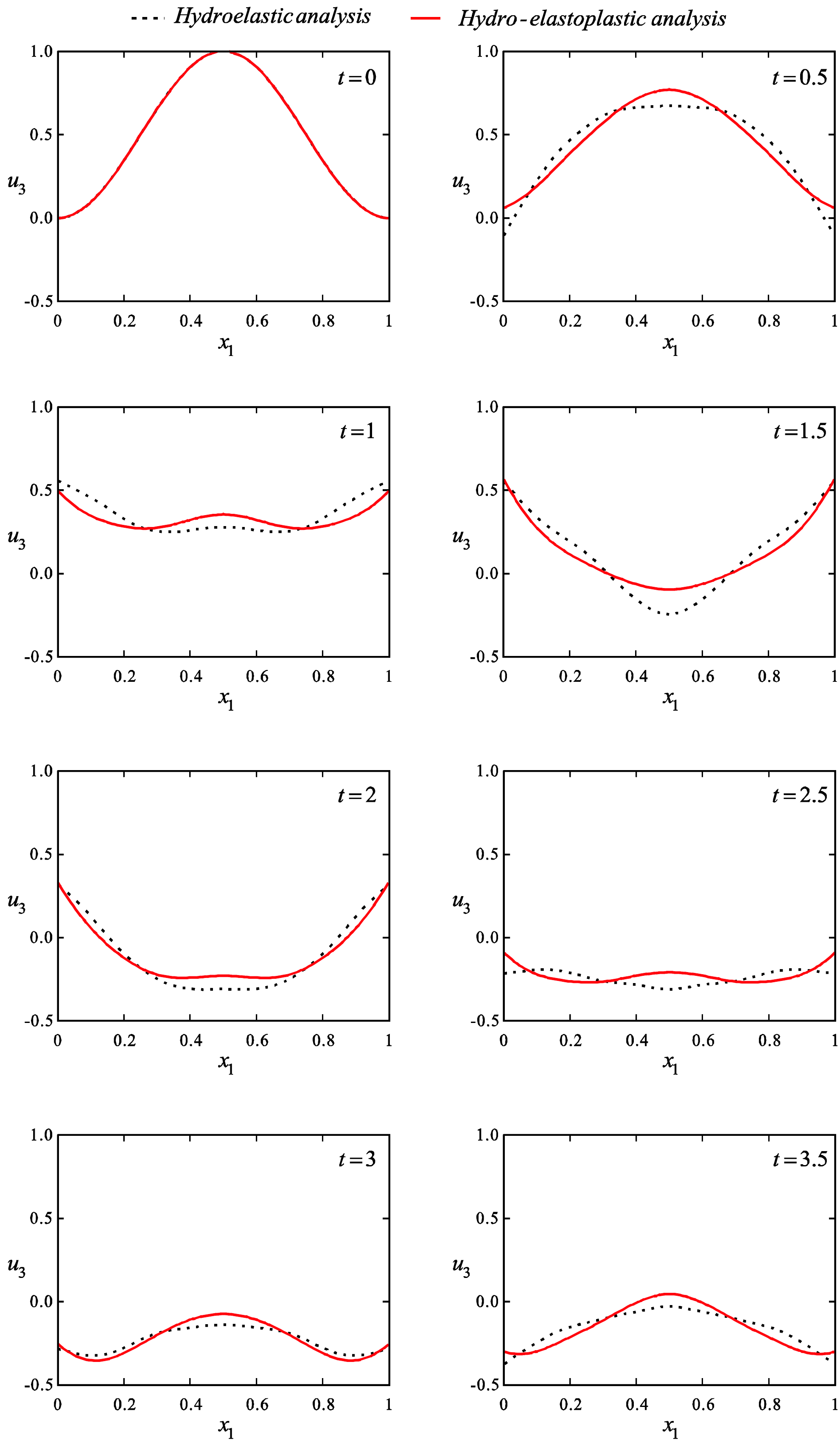

Figure 5.11. Time histories of deflections over the floating elastoplastic plate structure with symmetric initial displacement for $h/L=4$.

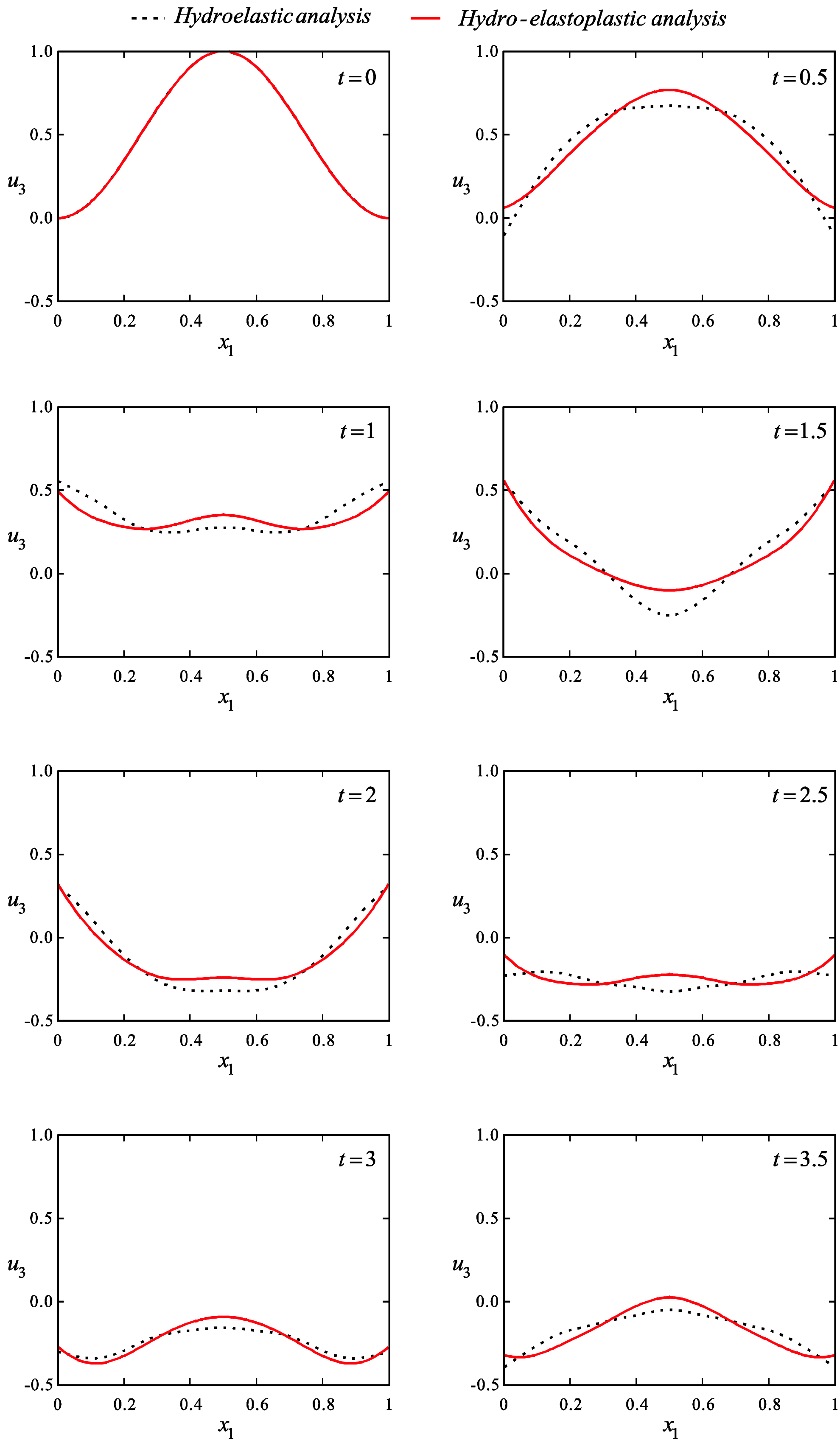

Figure 5.12. Time histories of deflections over the floating elastoplastic plate structure with symmetric initial displacement for $h/L=8$.

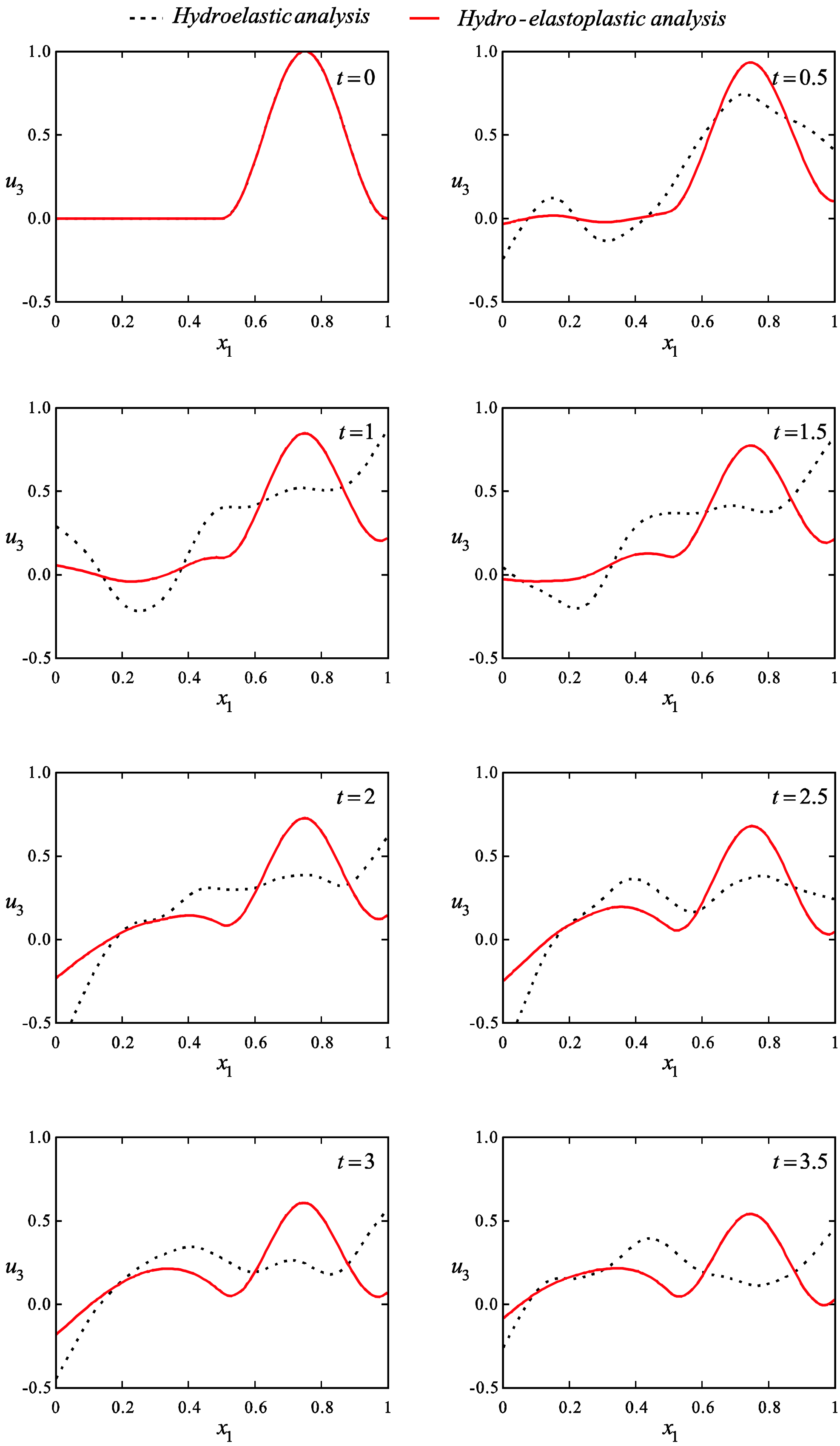

Figure 5.13. Time histories of deflections over the floating elastoplastic plate structure with non-symmetric initial displacement for $h/L = 0.02$.

5.1.2 Floating Plate Model for the Weight Drop Test

Let us consider hydro-elastoplastic responses of the experimental model used by Endo and Yago [16]. **Table 4.1** present details of the plate model. Here, an elastic-perfectly-plastic material ($E = 0.6661 Gpa$, and $\sigma_y = 0.1 Mpa$) is employed. Hydroelastic and hydro-elastoplastic analysis of the floating plate structure subjected to an impact load, which is induced by a weight of $196N$ and dropped on a hit point in **Figure 5.14**.

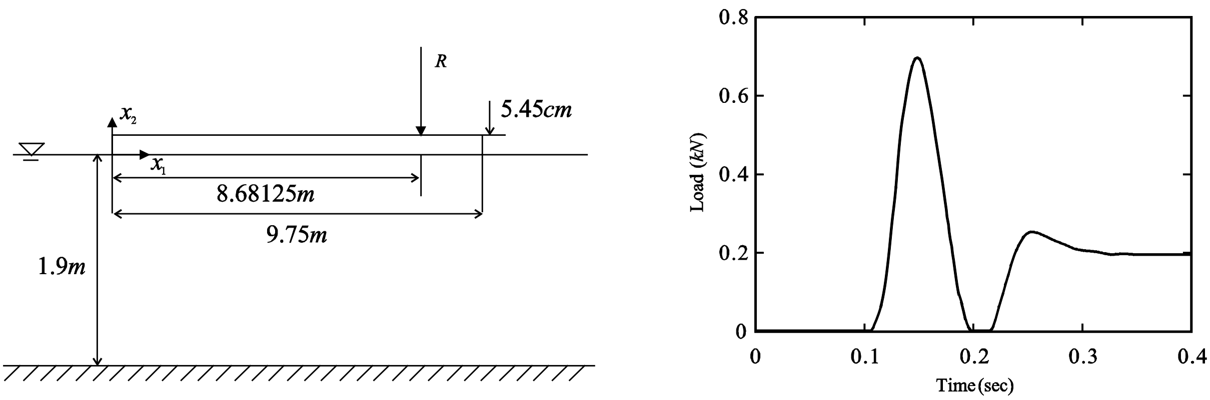

Figure 5.14. Floating plate structure subjected to a weight drop impact.

Figure 5.15 and 5.16 show the deflections and the distributions of the effective plastic strain over the floating elastic plate structure at 0.5 sec, respectively.

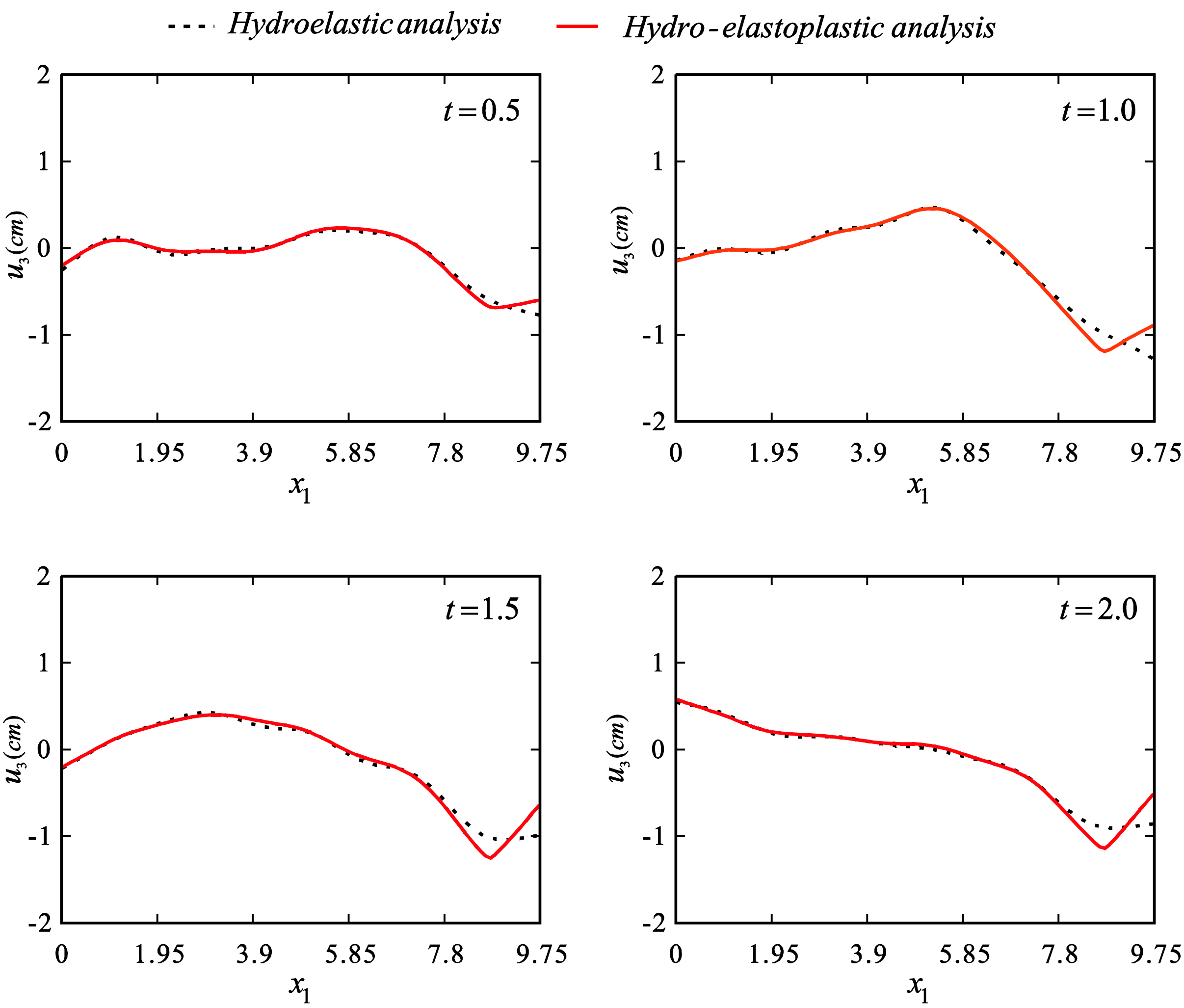

Figure 5.15. Time histories of deflections over the floating elastoplastic plate structure subjected to a weight drop impact.

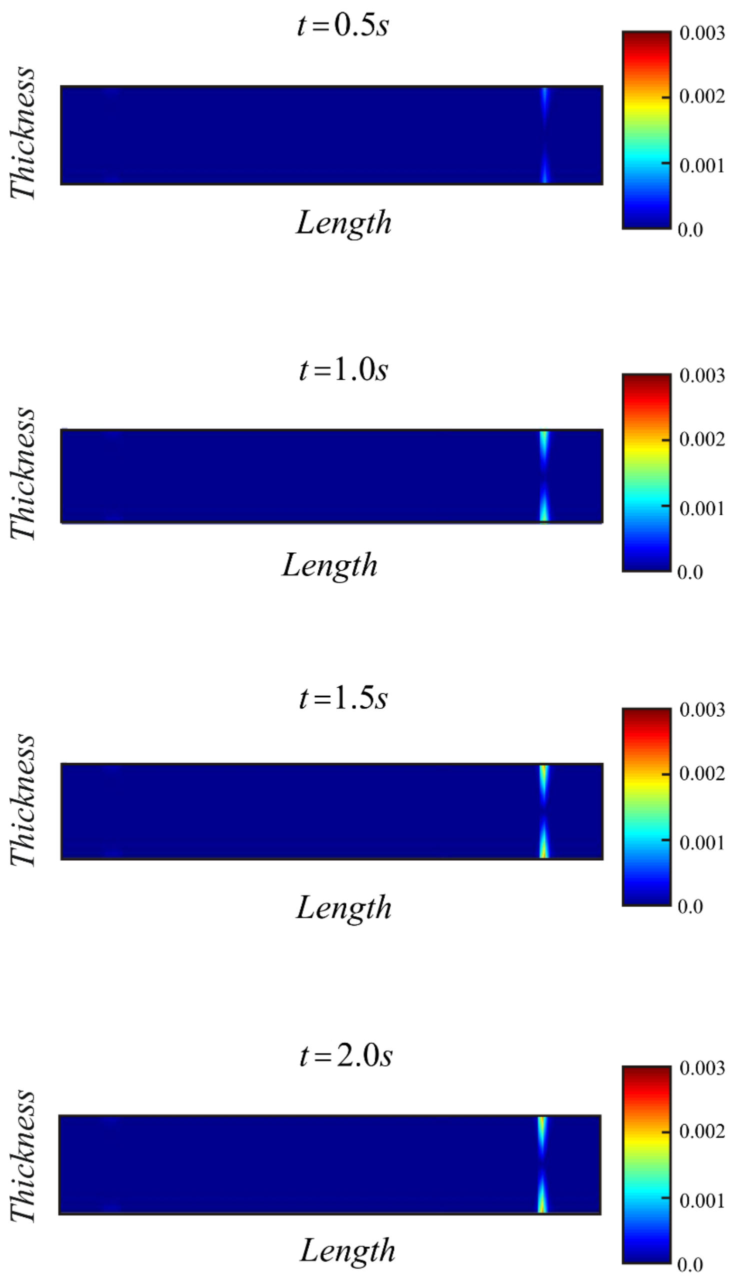

Figure 5.16. Distributions of effective plastic strain over the floating elastoplastic plate structure subjected to a weight drop impact.

5.2 Hydrodynamic Problems for Floating Plate Structures in Three Dimensions

This section present the hydro-elastoplastic responses of floating plate structures subjected to external loads as shown in **Figure 4.1**. In the discretized coupled equation (4.25), the MITC4 plate and a 4-node quadrilateral boundary elements are employed. To simulate the elastoplastic behavior of the floating plate structures, the implicit return mapping algorithm in **Table 5.1** is adopted, in which a nonlinear equation f_n derived from the plate state-projected von Mises model [83] is solved:

$$f_n(\Delta\chi) = \frac{1}{4}\left\{\frac{\left(\sigma_{11}^E + \sigma_{22}^E\right)^2}{\left[1 + E\Delta\chi / 3(1-\nu)\right]^2} + \frac{3\left(\sigma_{22}^E - \sigma_{11}^E\right)^2 + 12\left[\left(\sigma_{12}^E\right)^2 + \left(\sigma_{13}^E\right)^2 + \left(\sigma_{23}^E\right)^2\right]}{\left(1 + 2G_s\Delta\chi\right)^2}\right\} - \left[\sigma_y(\bar{e}^P)\right]^2 = 0\,, \tag{5.3}$$

where ν is Poisson's ratio and G_s is shear modulus.

Figure 5.17 gives a double plate model for numerical examples. The dimensions and material of the model are based on the phase - I Megafloat model in the Reference [11, 15]. The details are listed in **Table 5.3**. The following two load cases are considered:

- Load Case I: An impact load is applied.
- Load Case II: Dead weight and an incident wave-induced loads are applied together.

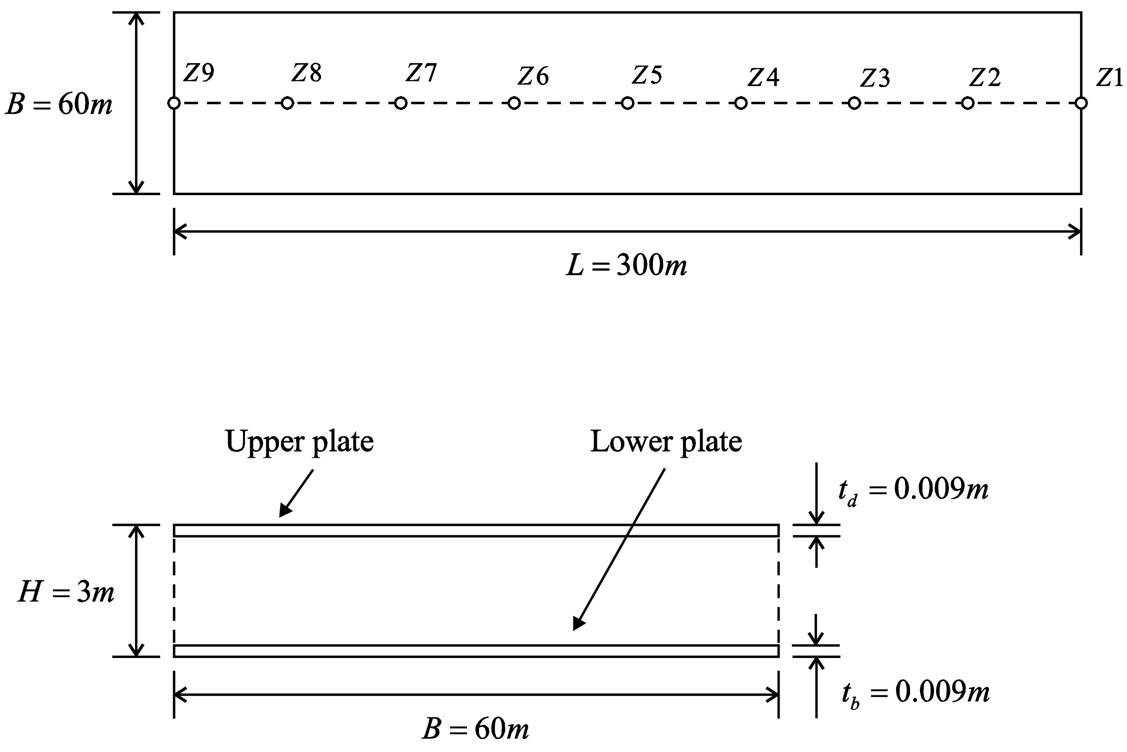

Figure 5.17. Description of the floating double plate structure with a rectangular cross-section.

Table 5.3. Details of the double plate model.

Parameter	Value
Length (L)	$300m$
Width (B)	$60m$
Thickness (H)	$3m$
Structural density (ρ_s)	$7800kg/m^3$
Young's modulus (E)	$206Gpa$
Yield stress (σ_y)	$238Mpa$
Dimensionless bending stiffness (S)	2.089×10^{-5}

The double plate structure is discretized using a 48×8 mesh of plate finite elements. The upper and lower plates and the empty space between both plates are modeled by employing 3 layers in the thickness direction of plate finite elements. The 5-point Newton-Cotes integration is used only for the upper and lower layers in the thickness direction as shown in Figure 5.18. Note that no numerical integration is performed for the middle layer of the empty space. The bilinear isotropic hardening model (plastic hardening modulus $E_P = 0.01E$) is used.

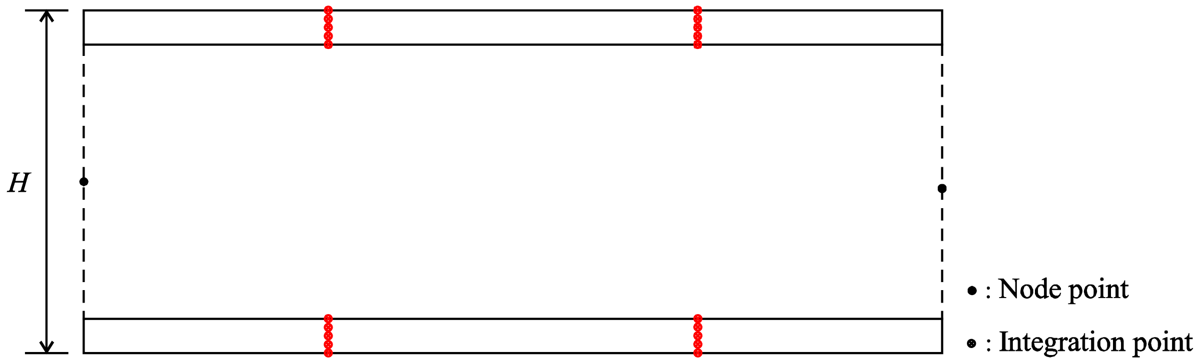

Figure 5.18. Newton-cotes integration points in plate cross-sections.

5.2.1 Impact Load Cases

An impact load with the history curve in **Figure 5.19** is applied at point Z2, which refers to a load time function for the crash of a Phantom RF-4E (see Reference [93]).

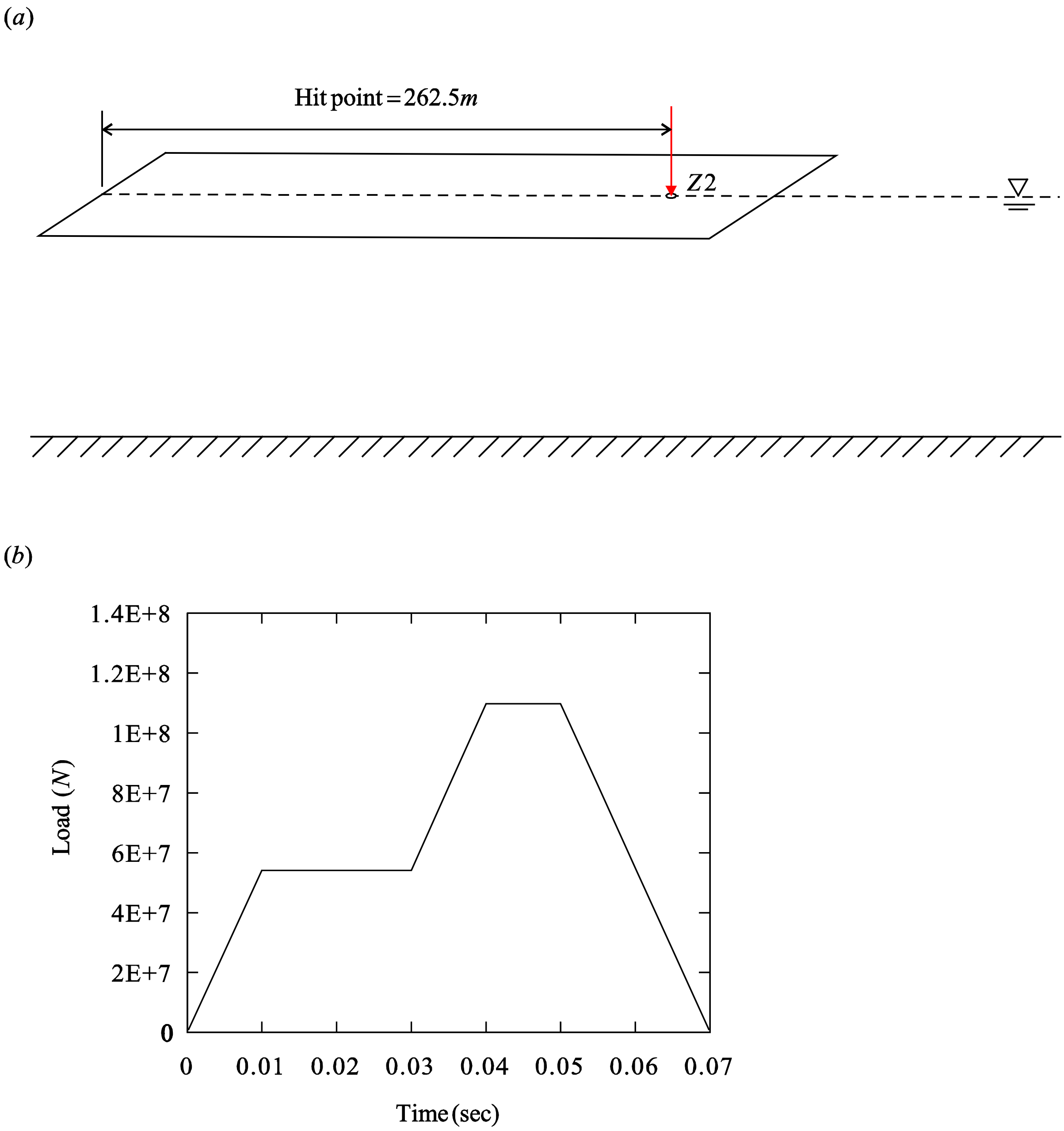

Figure 5.19. Description of hydrodynamic problems of the floating double plate structure subject to impact loads: (a) at a hit point with (b) a load curve.

Figure 5.20 shows the deflections at points calculated by using the hydroelastic and hydro-elastoplastic analyses with a time step size $\Delta t = 0.001$ of for a duration of 3s. In the results of both analyses, a large difference in deflection at loading point Z2 appears.

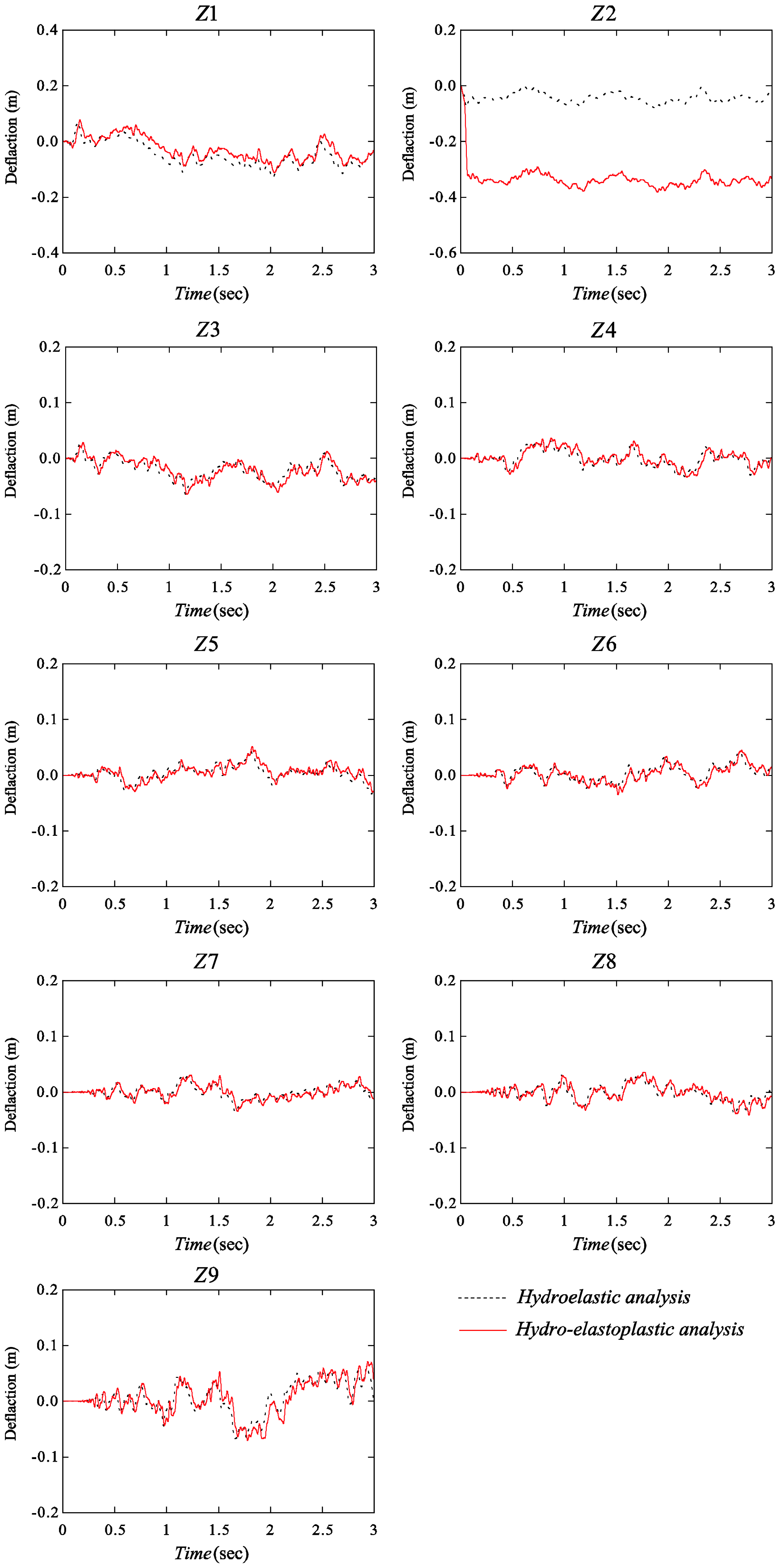

Figure 5.20. Time histories of deflections at points Z1-Z9 for an impact loading at point Z2.

Figure 5.21 depicts the distributions of the effective plastic strain at the top surface of the upper plate at sec intervals. The yield region occurs near the loading point. It is observed that the structural wave is propagated in the longitudinal direction after the impact loading.

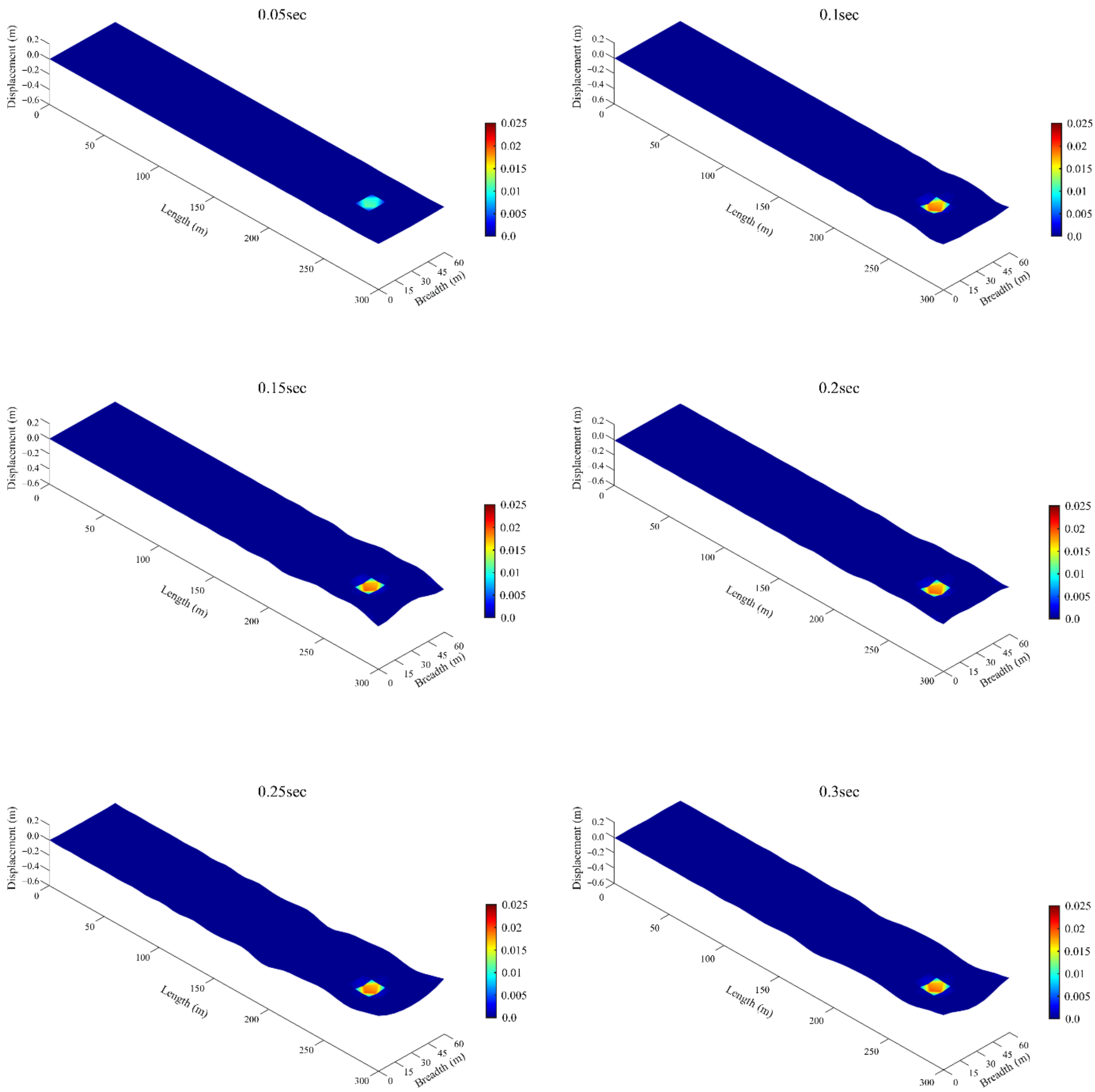

Figure 5.21. Distributions of effective plastic strain at the top surface of the upper plate in the hydro-elastoplastic problem of an impact loading at point Z2.

5.2.2 Dead Weight and an Incident Wave-induced Loads Cases

To solve the hydro-elastoplastic problems of the floating double plate structures subjected to the external loads as shown in **Figure 5.22(a)**, the hydrostatic responses to the dead weight loads are firstly evaluated though the following equation:

$$\begin{aligned} &\int_{V_S} C_{ijkl}^{EP}\, {}_0e_{ij}\delta\, {}_0e_{ij}\, dV - \int_{S_B} \rho_w g u_3(\mathbf{x};\tau+\Delta\tau) n_i \delta u_i\, dS \\ &= \int_{S_L} f_i^{S_L}(\mathbf{x};\tau+\Delta\tau) n_i \delta u_i\, dS - \int_{V_S} \rho_s g \delta u_i\, dV - \int_{V_S} \sigma_{ij}(\mathbf{x};\tau)\delta e_{ij}\, dV\ , \end{aligned} \tag{5.4}$$

where τ denotes only the intensity level of dead loads. Subsequently, the hydrodynamic responses with a time step size of $\Delta t = 0.02$ for a duration of 60s are calculated through hydroelastic and hydro-elastoplastic analyses, in which the static equilibrium state in Equation (5.4) and additional inertia forces applied by the dead weight loads are included.

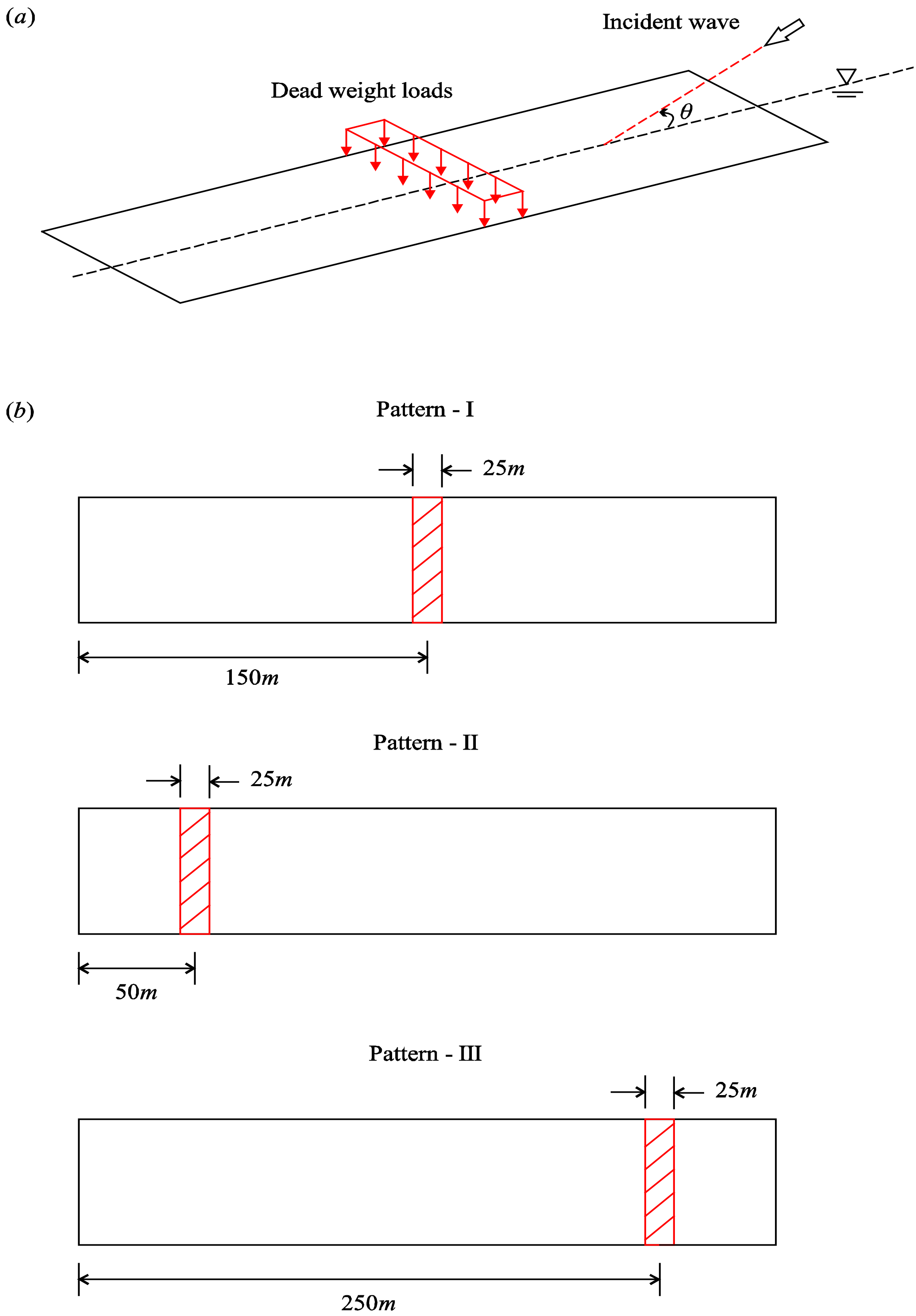

Figure 5.22. Hydrodynamic problems for the floating double plate structure subject to dead weight and incident wave–induced loads: (a) problem description and (b) distribution patterns of dead weight loads.

Figure 5.23 ~ 5.25 illustrate the deflections at points Z1–Z9 depending on the distribution patterns, in which an incident regular wave has $\alpha = 0.8$ and $A = 0.8$). And he distributions of effective plastic strain at the top surface of the upper plate at 5 sec intervals are depicted in **Figure 5.26 ~ 5.28**. As passing the incident wave to the plate, the effective plastic strain near the place of dead loading (Z5) increases in the early stage. A yield line is observed along the middle of the plate structure. **Figure 5.29 ~ 5.30** show the deflections at points Z1–Z9 according to wavelengths (i.e. $\alpha = 0.6$ and 0.8), in which the hydrodynamic problems of floating plate structures subjected to dead weight loads with distribution pattern I. It is important to note that the effect of plasticity on the hydrodynamic responses depends on the distribution of dead weight loads as well as amplitude and length of incident waves.

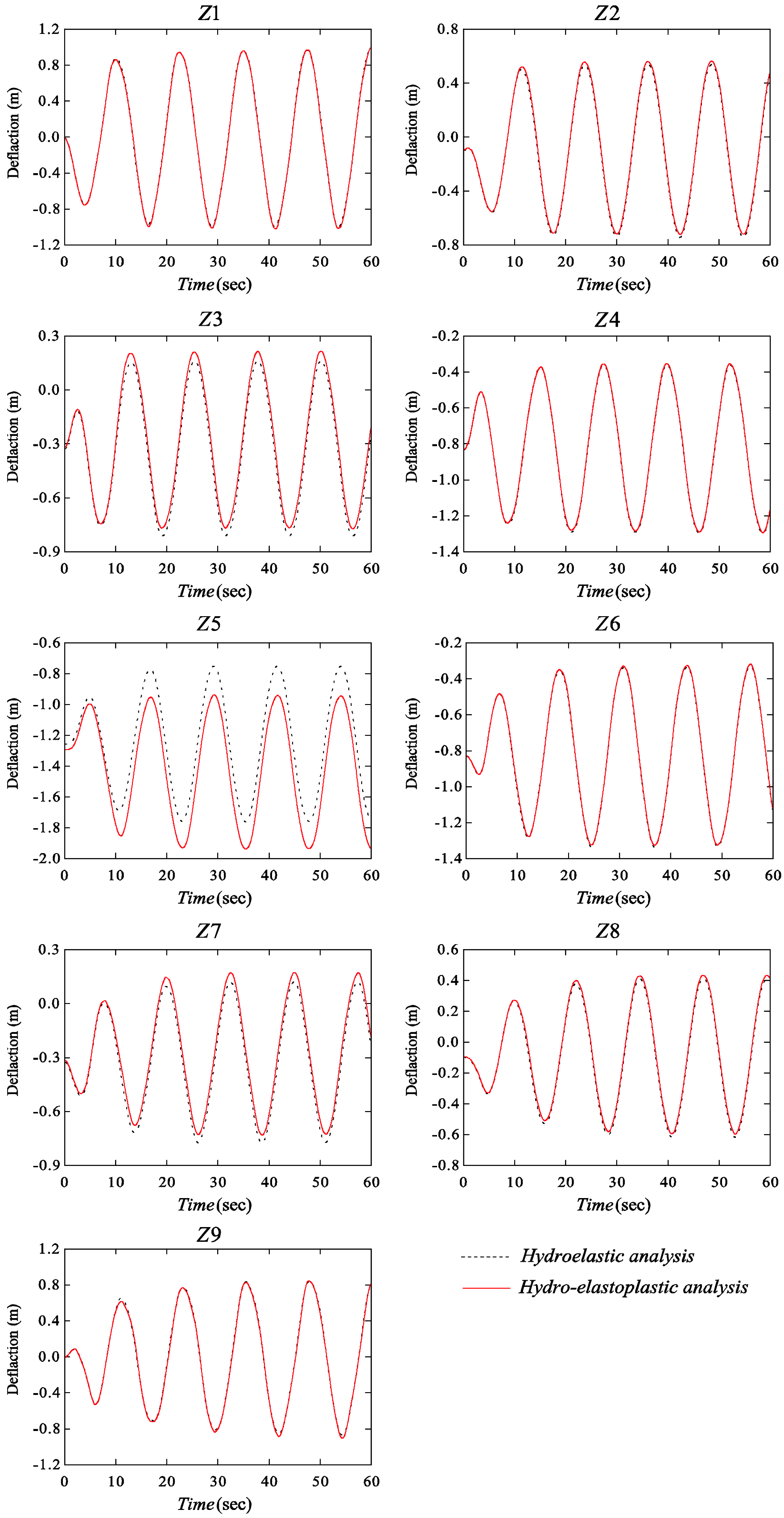

Figure 5.23. Time histories of deflections of floating plate structures subjected to dead weight load with distribution pattern I and an incident regular wave ($\alpha = 0.8$ and $A = 0.8m$) at points Z1-Z9.

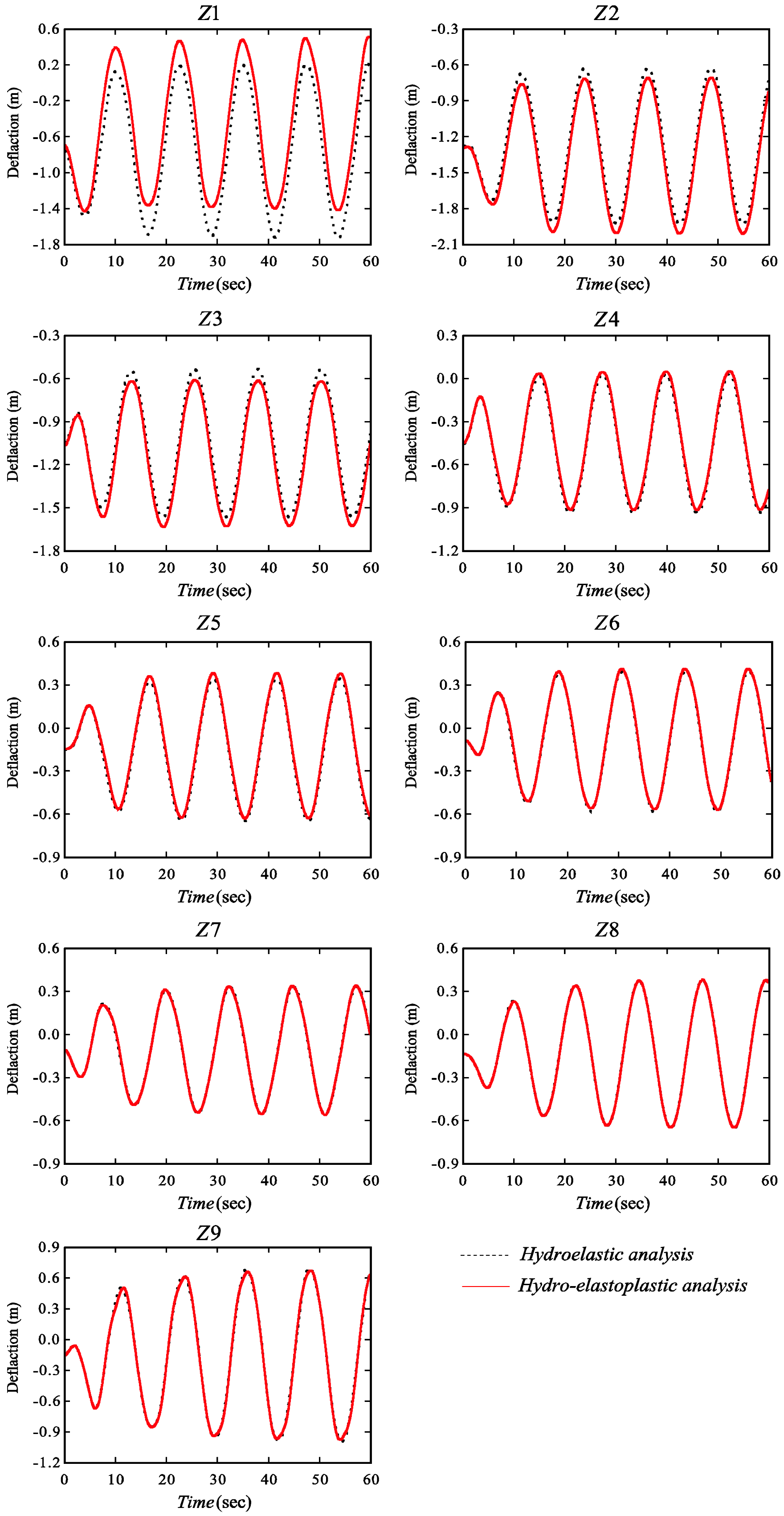

Figure 5.24. Time histories of deflections of floating plate structures subjected to dead weight load with distribution pattern II and an incident regular wave ($\alpha = 0.8$ and $A = 0.8m$) at points Z1-Z9.

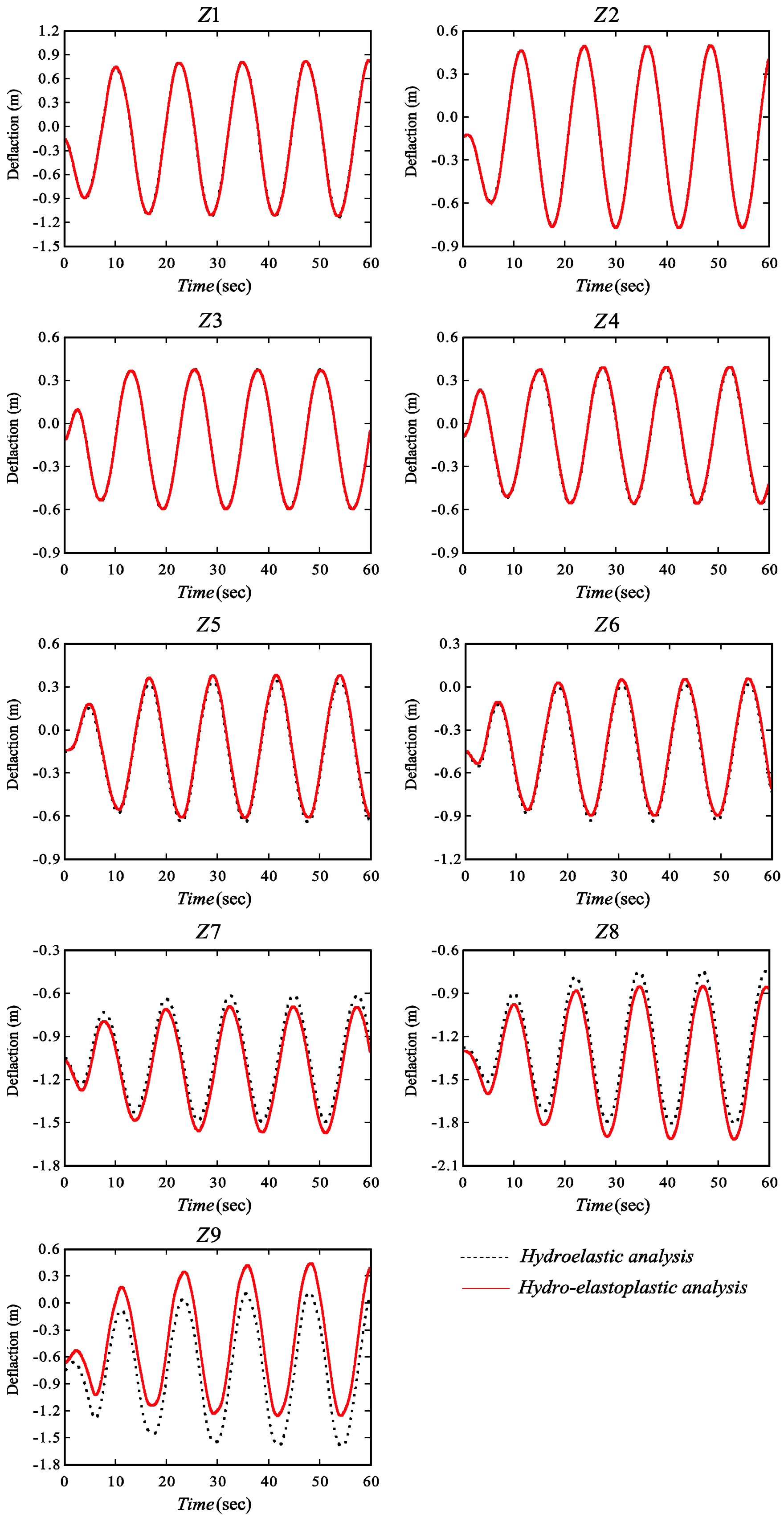

Figure 5.25. Time histories of deflections of floating plate structures subjected to dead weight load with distribution pattern III and an incident regular wave ($\alpha = 0.8$ and $A = 0.8m$) at points Z1-Z9.

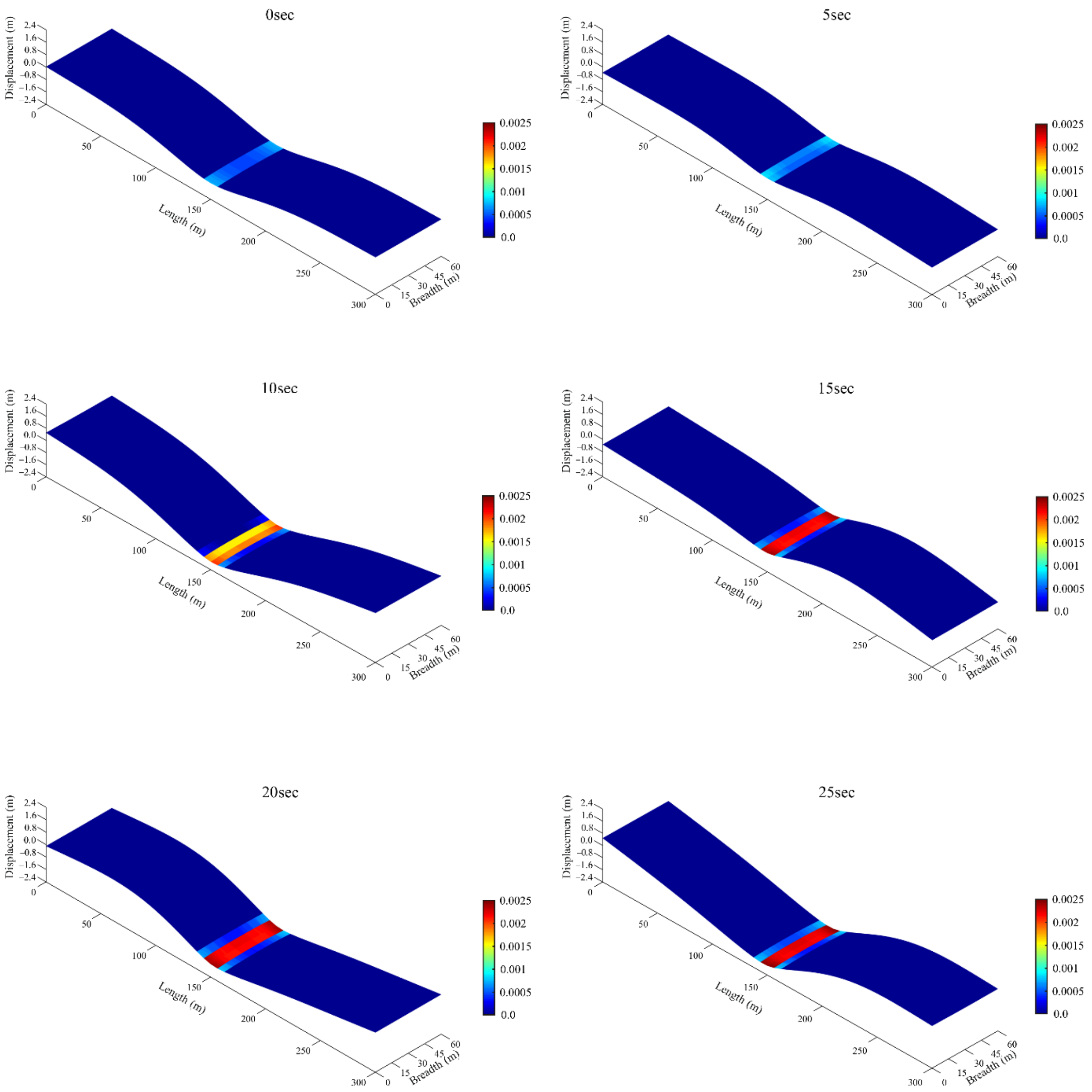

Figure 5.26. Distributions of effective plastic strain at the top surface of the upper plate in the hydro-elastoplastic problem for floating plate structures subjected to dead weight load with distribution pattern I and an incident regular wave ($\alpha = 0.8$ and $A = 0.8m$).

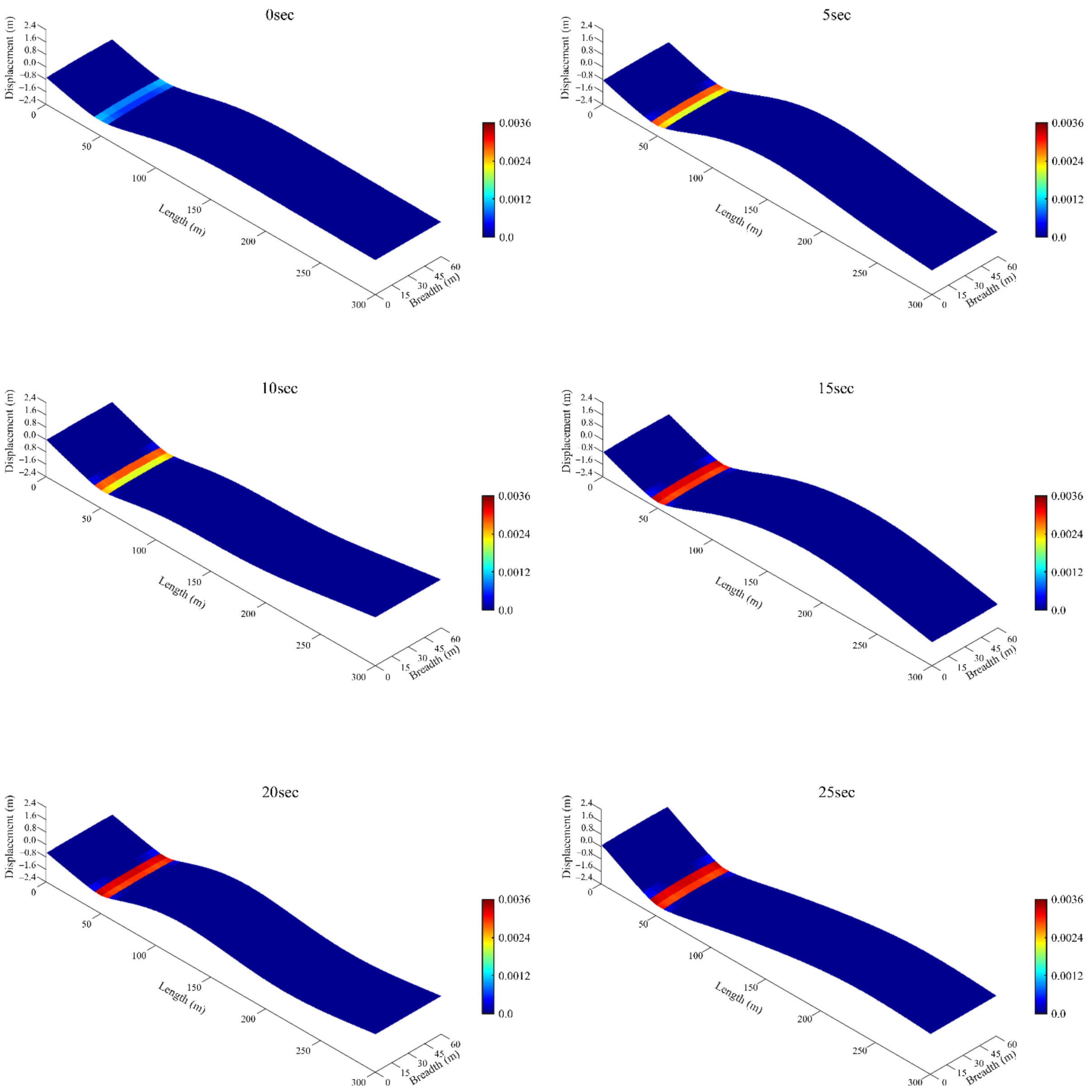

Figure 5.27. Distributions of effective plastic strain at the top surface of the upper plate in the hydro-elastoplastic problem for floating plate structures subjected to dead weight load with distribution pattern II and an incident regular wave ($\alpha = 0.8$ and $A = 0.8m$).

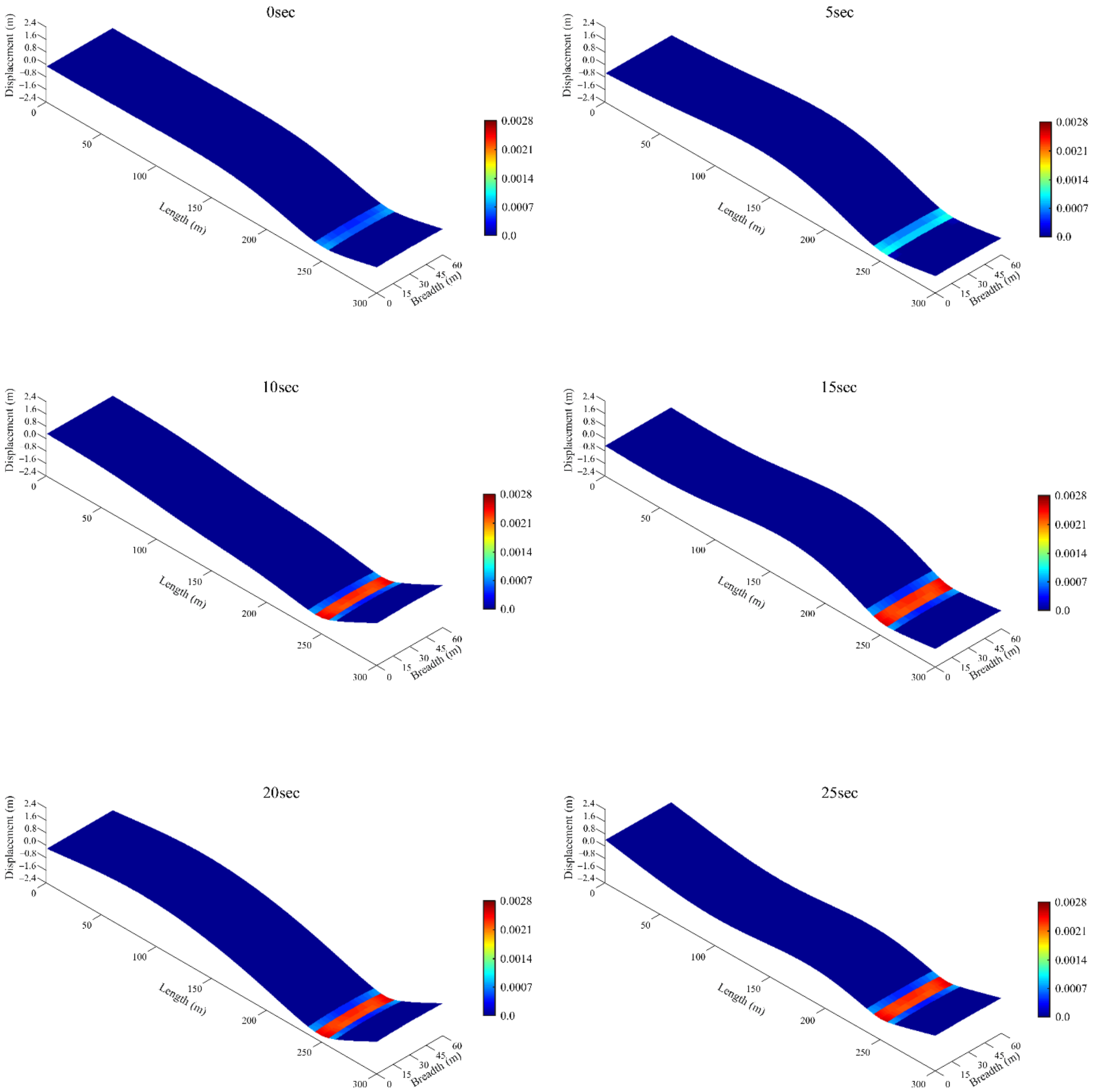

Figure 5.28. Distributions of effective plastic strain at the top surface of the upper plate in the hydro-elastoplastic problem for floating plate structures subjected to dead weight load with distribution pattern III and an incident regular wave ($\alpha = 0.8$ and $A = 0.8m$).

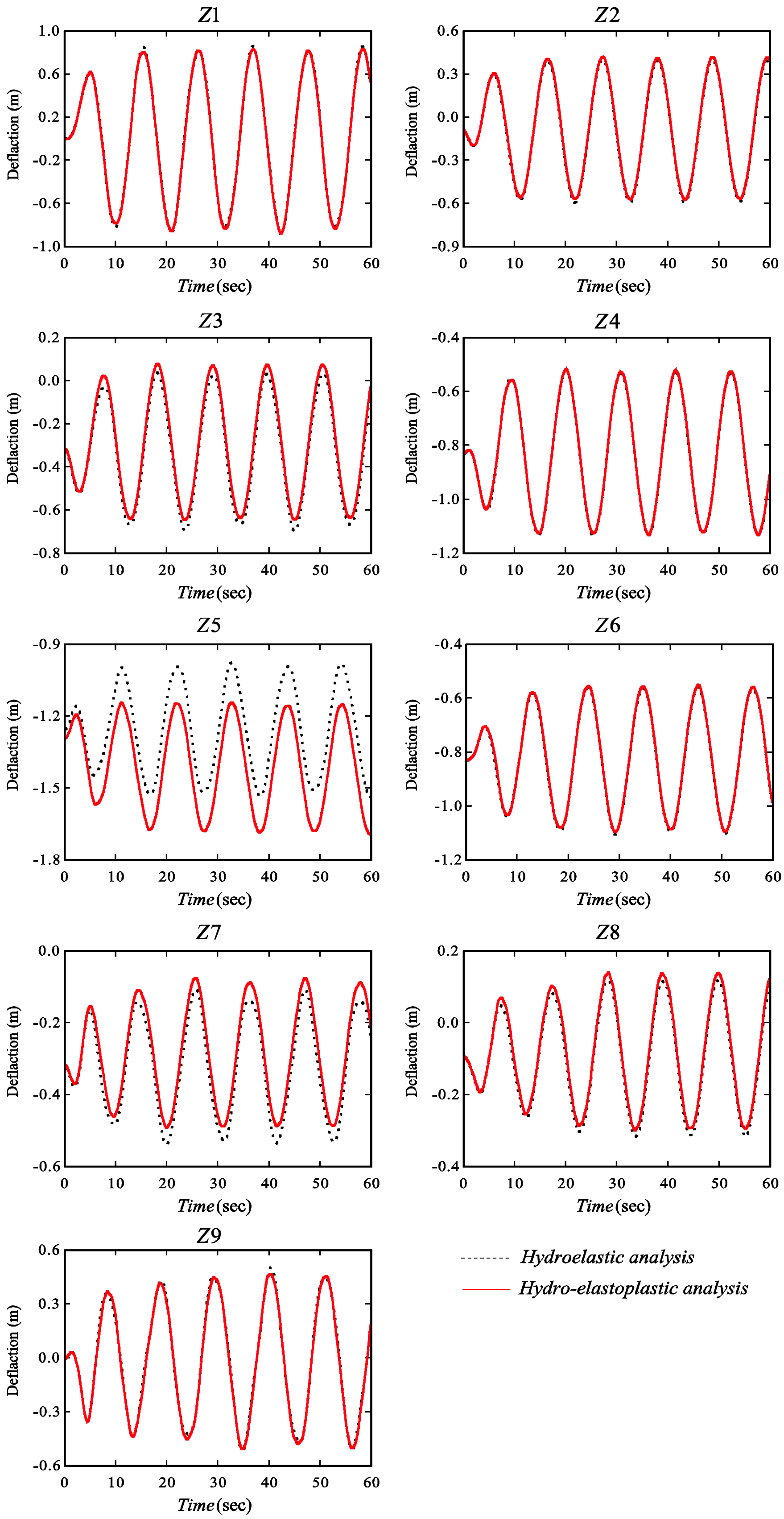

Figure 5.29. Time histories of deflections of floating plate structures subjected to dead weight load with distribution pattern I and an incident regular wave ($\alpha = 0.6$ and $A = 0.8m$) at points Z1-Z9.

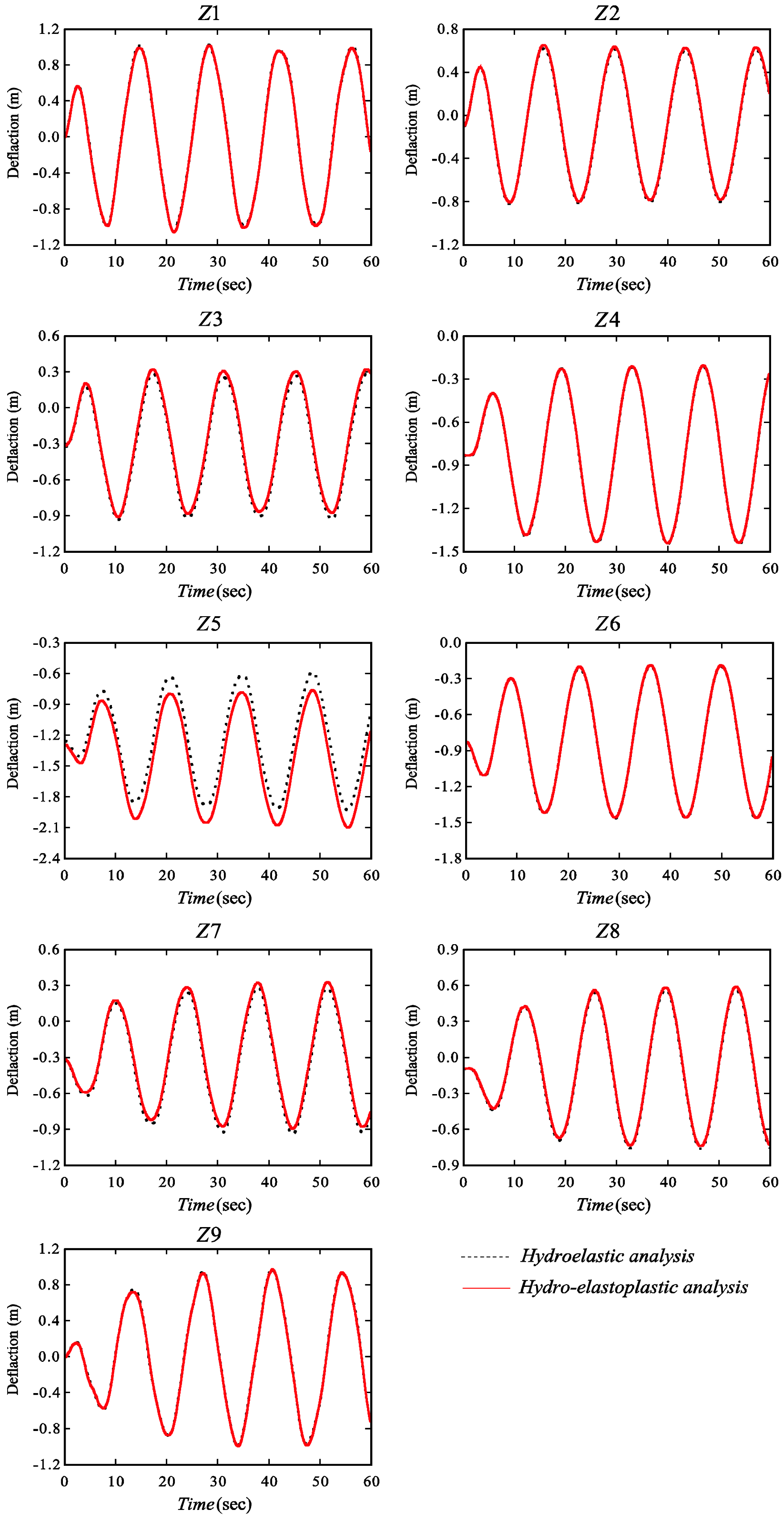

Figure 5.30. Time histories of deflections of floating plate structures subjected to dead weight load with distribution pattern I and an incident regular wave ($\alpha = 1.0$ and $A = 0.8m$) at points Z1-Z9.

5.3 Closure

This chapter presents hydroelastic and hydro-elastoplastic responses of plate structures floating on the surface of water in two and three dimensions. First, a series of benchmark problems for the time-dependent motion of a floating elastic plate structure released from rest and weight drop tests for transient elastic responses of a pontoon type VLFS are considered. And then, hydrodynamic problems of a floating double plate structure subjected to two load cases (i.e. impact load or dead weight and an incident wave-induced loads) are solved.

Chapter 6. Conclusions

In this thesis, significant efforts were paid for predicting hydrodynamic responses of floating plate structures in surface gravity waves. In particular, numerical procedures were developed to solve the problems of the interactions between floating plate structures and water wave in the frequency domain and in the time domain. It has been demonstrated that these procedures provide reasonable numerical solution by comparing to experimental and numerical results, and are effective in hydroelastic and hydro-elastoplastic analyses.

First, hydroelastic analysis of floating plate structures interacting with surface regular waves was performed. A formulation for the analysis based on a direct coupling method was derived. The directly coupled equations of motion are discretized by the finite element method for plate structures and the boundary element method for fluid. Through comparisons with experimental results of a pontoon type VLFS, the validity of the proposed procedure was confirmed.

Second, hydroelastic responses of floating plate structures with multiple hinge connections in regular waves are presented. To effectively model hinge connections on the above numerical procedure, a complete condensation method was derived, in which, the structural mass and stiffness and fluid-structure interaction terms corresponding to rotational DOFs are completely condensed. The proposed method has the advantage of the capability to easily model multiple hinge connections arbitrarily positioned. Through various numerical analyses, the modeling capability and the effects of multiple hinge connections was demonstrated.

Third, a nonlinear formulation for the hydro-elastoplastic analysis of floating plate structure was proposed, in which the convolution integral was employed to couple elastoplastic deformation and linear surface gravity waves in the time domain. The present formulation can describe the interactions between structures with material nonlinearity and the surrounding fluid. An implicit return mapping algorithm was implemented to simulate the plastic behaviors of the floating plates according to von Mises plastic model. The fluid is discretized by the boundary element method, and the IRFs are constructed by using the corresponding frequency-dependent metrics in the direct coupling method.

The capability of the proposed numerical procedure was investigated through comparisons with the numerical results of LS-DYNA for hydroelastic and hydro-elastoplastic problems. Further experimental studies are required for verification of the present numerical procedure and for comprehensive understanding of hydro-elastoplastic behaviors of floating plate structures. It also would be valuable to extend the proposed method for hydro-elastoplastic analysis of three dimensional ships or offshore platforms.

Finally, through hydrodynamic problems of floating plate structures subjected to external forces in two or three dimensions, the performance of the numerical method for hydro-elastoplastic analysis is demonstrated. For two dimensional problems, hydroelastic and hydro-elastoplastic responses for a series of benchmark calculations and weight drop tests are studied. Three dimensional hydrodynamic problems for a floating double plate structure subjected to two load cases (i.e. impact load or dead weight and an incident wave-induced loads) are solved. The proposed numerical method for hydro-elastoplastic analysis is applicable to hydroelastic as well as hydro-elastoplastic problems for floating beam or plate structures subjected to time-dependent external loads such as impact, incident regular and irregular waves, and so on.

Appendix A. The Free Surface Green's Functions

This Appendix briefly describes the free surface Green's functions. The detailed explanations of these functions are given in Reference [2, 69, 87, 88]. They are a velocity potential generated by a source potential and is used to efficiently formulate the fluid by the boundary integral equation.

A.1 Time-dependent Free Surface Green's Functions

The Green's function $G(\mathbf{x}, \boldsymbol{\xi}; t, \tau)$ satisfies the following conditions:

$$\nabla^2 G = -4\pi\delta(x_1 - \xi_1)\delta(x_2 - \xi_2)\delta(x_1 - \xi_3) \quad \text{for} \quad -h < x_3 < 0 \,, \tag{A.1a}$$

$$\ddot{G} + g\frac{\partial G}{\partial x_3} = 0 \quad \text{for} \quad x_3 = 0 \,, \tag{A.1b}$$

$$\frac{\partial G}{\partial x_3} = 0 \quad \text{for} \quad x_3 = -h \,, \tag{A.1c}$$

$$G = 0 \quad \text{for} \quad x_3 = 0 \quad \text{at} \quad t = \tau \,, \tag{A.1d}$$

$$\dot{G} = 0 \quad \text{for} \quad x_3 = 0 \quad \text{at} \quad t = \tau \,, \tag{A.1e}$$

and G and $\dot{G}$ are to be $O(e^{(\pi/2h-\varepsilon)\sqrt{x_1^2+x_2^2}})$ at any given time t as $\sqrt{x_1^2 + x_2^2} \to \infty$, in which ε is any positive number [87, 88], and δ is the Dirac' delta function..

The time-dependent Green's functions for finite and infinite depth are given by

$$\begin{aligned} G(\mathbf{x}, \boldsymbol{\xi}; t, \tau) = {} & \frac{1}{\sqrt{r^2 + (x_3 - \xi_3)^2}} - \frac{1}{\sqrt{r^2 + (x_3 + \xi_3)^2}} + 2\int_0^\infty \frac{e^{-kh} \sinh kx_3 \sinh k\xi_3}{\cosh kh} J_0(kr)dk \\ & + 2\int_0^\infty \frac{\cosh k(x_3 + h)\cosh(\xi_3 + h)}{\cosh^2 kh \tanh kh} \left\{1 - \cos\left[\sqrt{gk \tanh kh}(t - \tau)\right]\right\} J_0(kr)dk \,, \end{aligned} \tag{A.2}$$

and

$$G(\mathbf{x}, \boldsymbol{\xi}; t, \tau) = \frac{1}{\sqrt{r^2 + (x_3 - \xi_3)^2}} - \frac{1}{\sqrt{r^2 + (x_3 + \xi_3)^2}} + 2\int_0^\infty e^{k(x_3+h)} \left\{1 - \cos\left[\sqrt{gk}(t - \tau)\right]\right\} J\ (kr)dk \,, \tag{A.3}$$

respectively, where J_0 is the Bessel function of the first kind of order 0, and $r = \sqrt{(x_1 - \xi_1)^2 + (x_2 - \xi_2)^2}$.

A.2 Frequency-dependent Free Surface Green's Functions

The Green's function $\tilde{G}(\mathbf{x},\boldsymbol{\xi})$ satisfies the following conditions:

$$G(x,\xi;t,\tau) = \mathrm{Re}\left\{\tilde{G}(x,\xi)e^{j\omega t}\right\}, \tag{A.4a}$$

$$\nabla^2\tilde{G} = -4\pi\delta(x_1-\xi_1)\delta(x_2-\xi_2)\delta(x_1-\xi_3) \quad \text{for} \quad -h < x_3 < 0\,, \tag{A.4b}$$

$$\frac{\partial\tilde{G}}{\partial x_3} = \frac{\omega^2}{g}\tilde{G} \quad \text{for} \quad x_3 = 0 \quad \text{and} \quad x_i \neq \xi_i\,, \tag{A.4c}$$

$$\frac{\partial\tilde{G}}{\partial x_3} = 0 \quad \text{for} \quad x_3 = -h \quad \text{and} \quad x_i \neq \xi_i\,, \tag{A.4d}$$

$$\sqrt{r}\left[\frac{\partial}{\partial r} + jk\right]\tilde{G} = 0 \quad \text{as} \quad r \to \infty\,. \tag{A.4e}$$

The frequency-dependent Green's functions for finite and infinite depth are given by (see, e.g., Reference [2, 69])

$$\begin{aligned}\tilde{G}(x,\xi) &= \frac{1}{\sqrt{r^2+(x_3-\xi_3)^2}} + \frac{1}{\sqrt{r^2+(2h+x_3+\xi_3)^2}} \\ &+ \int_L \frac{2(z+\omega^2/g)\cosh z(x_3+h)\cosh z(\xi_3+h)}{z\sinh zh - \omega^2/g\cosh zh}e^{-zh}J_0(zr)dz\,,\end{aligned} \tag{A.5}$$

and

$$\tilde{G}(x,\xi) = \frac{1}{\sqrt{r^2+(x_3-\xi_3)^2}} + \int_L \frac{z+\omega^2/g}{z-\omega^2/g}e^{-z|x_3+\xi_3|}J_0(zr)dz\,, \tag{A.6}$$

respectively, where z means complex numbers, and L is the contour of an integration indented above the pole c_0 in the complex plane as shown in **Figure A.1**. The pole c_0 is the positive real root of the equations:

$$\begin{aligned}& z\tanh zh - \frac{\omega^2}{g} = 0 \quad \text{for the finite depth and} \\ & z - \frac{\omega^2}{g} = 0 \quad \text{for the infinite depth.}\end{aligned} \tag{A.7}$$

Figure A.1. Contour of integration in the Green's function.

A.3 Free Surface Green's Functions in two dimensional fluid

The time-dependent Green's functions with strength 2π are defined by

$$G(x_1,x_3,\xi_1,\xi_3;t,\tau)=\ln\sqrt{(x_1-\xi_1)^2+(x_3-\xi_3)^2}$$
$$-\ln\sqrt{(x_1-\xi_1)^2+(x_3+\xi_3)^2}+4\pi\int_0^\infty e^{-hk}\frac{\sinh k\xi_3\sinh kx_3}{k\cosh kh}\cos k|x_1-\xi_1|dk \tag{A.8}$$
$$-2\int_0^\infty\frac{\cosh k(x_3+h)\cosh k(\xi_3+h)}{\cosh^2 kh}\frac{1-\cos\sqrt{gk\tanh kh}(t-\tau)}{k\tanh kh}\cos k|x_1-\xi_1|dk\,,$$

for the finite depth, and

$$G(x_1,x_3,\xi_1,\xi_3;t,\tau)=\ln\sqrt{(x_1-\xi_1)^2+(x_3-\xi_3)^2}-\ln\sqrt{(x_1-\xi_1)^2+(x_3+\xi_3)^2}$$
$$-2\int_0^\infty\frac{1-\cos\sqrt{gk}(t-\tau)}{k}\cos k|x_1-\xi_1|dk\,, \tag{A.9}$$

for the infinite depth.

The frequency-dependent Green's functions with strength 2π are defined by

$$\tilde{G}(x_1,x_3,\xi_1,\xi_3)=\ln\sqrt{(x_1-\xi_1)^2+(x_3-\xi_3)^2}+\ln\sqrt{(x_1-\xi_1)^2+(2h+x_3+\xi_3)^2}-2\ln h$$
$$-2\int_L\left\{\frac{(\omega^2/g+k)e^{-kh}\cosh k(x_3+h)\cosh k(\xi_3+h)}{k(k\sinh kh-\omega^2/g\cosh kh)}\cos k|x_1-\xi_1|+\frac{e^{-kh}}{k}\right\}dk\,, \tag{A.10a}$$

or

$$\tilde{G}(x_1,x_3,\xi_1,\xi_3)=-2\pi\sum_{i=0}^{\infty}\frac{je^{jc_i|x_1-\xi_1|}}{c_i}\frac{c_i^2-(\omega^2/g)^2\cosh c_i(x_3+h)\cosh c_i(\xi_3+h)}{\left[c_i^2h-(\omega^2/g)^2h+(\omega^2/g)\right]}\,, \tag{A.10b}$$

for the finite depth, and

$$\tilde{G}(x_1,x_3,\xi_1,\xi_3)=\ln\sqrt{(x_1-\xi_1)^2+(x_3-\xi_3)^2}$$
$$+\int_L\left\{\frac{(\omega^2/g+k)}{k(\omega^2/g-k)}e^{-k(x_3+\xi_3)}\cos k|x_1-\xi_1|-\frac{e^{-k}}{k}\right\}dk \tag{A.11}$$

the infinite depth, where c_i is the positive pure imaginary roots of Equation (A.7).

Bibliography

[1] H. Lamb. Hydrodynamics. Dover Publications. New York 1945.

[2] F. John. On the motion of floating bodies I. Commun Pur Appl 1949;2;13-57.

[3] F. John. On the motion of floating bodies II. Simple harmonic motions. Commun Pur Appl 1950;3;45-101.

[4] J.N. Newman. Marine Hydrodynamics. Cambridge, Massachusetts; The MIT Press. 1977.

[5] R.E.D. Bishop, W.G. Price. Hydroelasticity of ships. Cambridge. Cambridge University Press. 1979.

[6] C.C. Mei. Theory and applications of ocean surface waves, Part I: Linear Aspects. World Scientific. 2005.

[7] C.C. Mei. Theory and applications of ocean surface waves, Part II: Nonlinear Aspects. World Scientific. 2005.

[8] O.M. Faltinsen. Hydrodynamics of marine and offshore structures. J Hydrodyn Ser B. 2014;26;835-47.

[9] J.M.J. Journée, W.W. Massie. Offshore Hydrodynamics. Delft University of Technology. 2001.

[10] E. Watanabe, T. Utsunomiya, C.M. Wang. Hydroelastic analysis of pontoon-type VLFS: a literature survey. Eng Struct. 2004;26;245-56.

[11] H. Suzuki. Overview of Megafloat: Concept, design criteria, analysis, and design. Mar Struct. 2005;18;111-32.

[12] M. Fujikubo. Structural analysis for the design of VLFS. Mar Struct. 2005;18;201-226.

[13] S.Y. Hong. Design manual for very large floating structures. KIOST. 2007.

[14] ISSC. Report of Special Committee VI.2 "Very Large Floating Structures". Proc of 16th ISOPE. Southampton. United Kingdom. 2006.

[15] K. Yago, H. Endo. On the hydroelastic response of box-shaped floating structure with shallow draft. J Soc Nav Archit Jpn. 1996;180;341-52.

[16] H. Endo, K. Yago. Time history response of a large floating structure subjected to dynamic load. J Soc Nav Archit Jpn. 1999:186:36-76.

[17] H. Endo. The behavior of a VLFS and an airplane during takeoff/landing run in wave condition. Mar Struct 2000;13;477-91.

[18] E. Watanabe, T. Utsunomiya, C.M. Wang. Very Large Floating Structures. Taylor & Francis, London and New York 2008.

[19] M. Lamas-Pardo, G. Iglesias, L. Carral. A review of very large floating structures (VLFS) for coastal and offshore uses. Ocean Eng. 2015:109:677-90.

[20] A.I. Andrianov. Hydroelastic Analysis of Very Large Floating Structures. Delft University of Technology. Delft. 2005.

[21] H. Suzuki. Safety target of very large floating structure used as a floating airport. Mar Struc. 2001;14;103-13.

[22] M. Kashiwag. Research on Hydroelastic Responses of VLFS: Recent Progress and Future Work. ISOPE. 2000;10;81-90.

[23] K. Takagi. Hydroelastic Response of a Very Large Floating Structure in Waves - a Simple Representation by the Parabolic Approximation. Appl Ocean Res. 2002;24;175-83.

[24] A. Girard, D. Empey, J. Borges de Sousa, S. Spry, J. Hedrick. An Experimental Testbed for Mobile Offshore Base Control Concepts. University of California at Berkeley. Berkeley. 2001.

[25] M. Lamas Pardo, L. Carral. Offshore and Coastal Floating Hotels: Flotels. IJME. The Royal Institution of Naval Architects. London 2011.

[26] M. Lamas Pardo, R. Pérez Fernández. Offshore concrete structures. Ocean Eng. 2013;58;304–16.

[27] P. Palo. Mobile offshore base: hydrodynamic advancements and remaining challenges. Mar Struct 2005;18;133–47.

[28] T. Utsunomiya, E. Watanabe, R. Taylor. Wave response analysis of a box-like VLFS close to a breakwater. OMAE98-4331. 1998.

[29] C. Wang, Z. Tay. Very large floating structures: applications, research and development. Proc Eng. 2 011;14;62–72.

[30] S. Ohmatsu. Overview: Research on Wave Loading and Responses of VLFS. Mar Struct. 2015;18;149–68.

[31] M. Ohkusu, Y. Namba. Hydroelastic Analysis of a Large Floating Structure. J Fluid Struct. 2004;19;543–55.

[32] V.A. Squire. Of Ocean Waves and Sea-ice Revisited. Cold Reg Sci Tech. 2007;49;110–33.

[33] A.I. Andrianov, A.J. Hermans. Hydroelastic Analysis of Floating Plate of Finite Draft. Appl Ocean Res. 2006;28;313–25.

[34] E. Watanabe, T. Utsunomiya, C.M. Wang, L.T.T. Hang. Benchmark Hydroelastic Responses of a Circular VLFS Under Wave Action. Eng Struct. 2006;28 423–30.

[35] X.J. Chen, W.S. Wu, W.C. Cui, J. Juncher Jensen. Review of Hydroelasticity Theories for Global Response of Marine Structures. Ocean Eng. 2006;33;439–57.

[36] R.E.D. Bishop, W. G. Price, Y. Wu. A General Linear Hydroelasticity Theory of Floating Structures Moving in a Seaway. Philos T Roy Soc A. 1986;316;375–426.

[37] M. Kashiwagi. A B-spline Galerkin scheme for calculating the hydroelastic response of a very large floating structure in waves. J. Mar. Sci. Technol. 1998; 3;37-49.

[38] C. Wu, E. Watanabe, T. Utsunomiya. An eigenfunction expansion-matching method for analyzing the wave-induced responses of an elastic floating plate. Appl. Ocean. Res. 1995;17;301-10.

[39] Khabakhpasheva TI, Korobkin AA. Hydroelastic behaviour of compound floating plate in waves. J Eng Math. 2002;44;21–40.

[40] Wang CD, Meylan MH. A higer-order-coupled boundary element and finite element method for the wave forcing of a floating elastic plate. J Fluids Struct. 2004;19;557–72.

[41] R. Eatock Taylor. Hydroelastic analysis of plates and some approximations. J Eng Math. 2007; 58:267–78.

[42] K.T. Kim, P.S. Lee, K.C. Park. A direct coupling method for 3D hydroelastic analysis of floating structures. Int. J Numer Meth Eng. 2013;96;842-66.

[43] J.G. Kim, S.P. Cho, K.T. Kim, P.S. Lee. Hydroelastic design contour for the preliminary design of very large floating structures. Ocean Eng. 2014;78;112-23.

[44] J.S. Yoon, S.P. Cho, R.G. Jiwinangun, P.S. Lee. Hydroelastic analysis of floating plates with multiple hinge connections in regular waves. Mar Struct. 2014;36;65-87.

[45] C.H. Lee, J.N. Newman. An assessment of hydroelasticity for very large hinged vessels, J Fluid Struct. 2000;14;957-70.

[46] J.N. Newman. Efficient hydrodynamic analysis of very large floating structures. Mar Struct. 2005;16;169-180.

[47] T.I. Khabakhpasheva, A.A. Korobkin. Hydroelstic behaviour of compound floating plate in waves. J. Eng. Math. 2002; 44;21-40.

[48] C.M. Wang, Z.Y. Tay, K. Takagi, T. Utsunomiya. Literature review of methods for mitigating hydroelastic response of VLFS under wave action. Appl Mech Rev. 2010;63;030802-1-18.

[49] M. Riyansyah, C.M. Wang, Y.S. Choo. Connection design for two-floating beam system for minimum hydroelastic response. Mar Struct. 2010;23;67-87.

[50] S. Fu, T. Moan, X. Chen, W. Cui. Hydroelastic analysis of flexible floating interconnected structures. Ocean Eng. 2007;34;1516-31.

[51] R.P. Gao, Z.Y. Tay, C.M. Wang, C.G. Koh, Hydroelastic response of very large floating structure with a flexible line connection. Ocean. Eng. 2011;38;1957-66.

[52] B.W. Kim, J.H. Kyoung, S.Y. Hong, S.K. Cho. Investigation of the effect of stiffness distribution and structure shape on hydroelastic responses of very large floating structures, Proc of 15th ISOPE. Seoul. 2005;210-17.

[53] B.W. Kim, S.Y. Hong, J.H. Kyoung, S.K. Cho. Evaluation of bending moments and shear forces at unit connections of very large floating structures using hydroelastic and rigid body analyses. Ocean Eng. 2007;34;1668-79.

[54] E. Loukogeorgaki, C. Michailides, D.C. Angelides. Hydroelastic analysis of a flexible mat-shaped floating breakwater under oblique wave action. J Fluid Struct. 2012;31;103-124.

[55] C. Michailides, D.C. Angelides. Modeling of energy extraction and behavior of a flexible floating breakwater. Appl Ocean Res. 2012;35;77-94.

[56] X.D. Liu, S. Sakai. Time domain analysis on the dynamic response of a flexible floating structure to waves. J Engng Mechanics. 2002;128;48–56.

[57] J.H. Kyoung, S.Y. Hong, B.W. Kim. FEM for time domain analysis of hydroelastic response of VLFS with fully nonlinear free-surface conditions. ISOPE. 2006;16;168–74.

[58] L. Qiu. Numerical simulation of transient hydroelastic response of a floating beam induced by landing loads. Appl Ocean Res. 2007;29;91–8.

[59] Y. Cheng. Direct time domain numerical analysis of transient behavior of a VLFS during unsteady external loads in wave condition. Abstr Appl Anal. 2014;1 – 17.

[60] W.E. Cummins. The impulse response function and ship motions. Schiffstechnik. 1962;9;101-9.

[61] W. Liu, K. Suzaki, K. Shibanuma. Nonlinear dynamic response and structural evaluation of container ship in large freak waves. J Offshore Mech Arct. 2015;137;011601.

[62] Z. Pei, K. Iijima, M. Fujikubo, S. Tanaka, S. Okazawa, T. Yao. Simulation on progressive collapse behavior of whole ship model under extreme waves using idealized structural unit method. Mar Struct. 2015;40;104-33.

[63] K. Iijima, K. Kimura, W. Xu, M. Fujikubo. Hydroelasto-plasticity approach to predicting the post-ultimate strength behavior of a ship's hull girder in waves. J Mar Sci Technol. 2011;16;379-89.

[64] K. Iijima, Y. Suzaki, M. Fujikubo. Scaled model tests for the post-ultimate strength collapse behavior of a ship's hull girder under whipping loads. Ships Offshore Struc. 2013.

[65] W. Liu, K. Suzaki, K. Shibanuma. A two-dimensional hydroelastoplasticity method of a container ship in extreme waves. J Offshore Mech Arct. 2015;137;021101.

[66] J.S. Yoon and P.S. Lee. Hydro-elastoplastic analysis of floating plates in waves. Proc of 30th Workshop on Water Wave and Floating Bodies. Bristol. 2015.

[67] K.J Bathe. Finite element procedure, Prentice Hall. New York. 1996.

[68] R.G. Dean, R.A. Dalrymple. Water wave mechanics for engineers and scientists. Englewood Cliffs. NJ. Prentice Halll. 1984.

[69] J.V. Wehausen, E.V. Laitone. Surface waves. Encyclopedia of physics. 1960;9;446-778.

[70] K.J. Bathe, E.N. Dvorkin. A formulation of general shell elements-the use of mixed interpolation of tensorial components. Int J Numer Meth Eng. 1986;22;697-722.

[71] K.J. Bathe, P.S. Lee, J.F. Hiller. Towards improving the MITC9 shell element. Comput Struct. 2003;81;477-89.

[72] P.S. Lee, K.J. Bathe. Development of MITC isotropic triangular shell finite elements. Comput Struct. 2004;82;945-62.

[73] P.S. Lee, H.C. Noh, K.J. Bathe. Insight into 3-node triangular shell finite elements: the effects of element isotropy and mesh patterns. Comput Struct. 2007;85;404-18.

[74] P.S. Lee, K.J. Bathe. The quadratic MITC plate and MITC shell elements in plate bending. Adv Eng Softw 2010;41;712-28.

[75] K.J. Bathe, P.S. Lee. Measuring the convergence behavior of shell analysis schemes. Comput Struct. 2011;89; 285-301.

[76] Y.G. Lee, K.H. Yoon, P.S. Lee, Improving the MITC3 shell finite element by using the Hellinger-Reissner principle. Comput. Struct. 110 (2012) 93-106.

[77] Y. Lee, P.S. Lee, K.J. Bathe. The MITC3+ shell finite element and its performance. Comput Struct 2014;138;12-23.

[78] H. M. Jeon, Y. Lee, P.S. Lee, K.J. Bathe. The MITC3+ shell finite element in geometric nonlinear analysis. Comput Struct. 2015;136;91-104.

[79] L. Meirovitch. Computational methods in structural dynamics. Sijthoff & Noordhoff international publishers. Alphen aan den Rijn. 1980.

[80] S.P. Cho. Numerical and experimental studies on hydroelastic behavior of floating structures. Korea Advanced Institute of Science and Technology. Korea. 2013.

[81] P. D. Komar. Beach Processes and Sedimentation. New Jersey. Prentice-Hall. 1976.

[82] M. Kojić, K.J Bathe. Inelastic analysis of solids and structures. Finite element procedure. Springer. 2005.

[83] E.A.S. Neto, D. Perić, D.R.J Owen. Computational method for Plasticity: Theory and Applications. Wiley & Sons. 2008.

[84] M. Kashiwagi. A time-domain mode-expansion method for calculating transient elastic responses of a pontoon-type. J Mar Sci Technol. 2000;5;89-100.

[85] D.H. Lee and H.S. Choi. Transient hydroelastic response of very large floating structures FE-BE hybrid method. Proc of 13th ISOPE. Honolulu 2003; 100-5.

[86] J.J. Stoker. Water waves. Interscience Publishers. New York. 1957.

[87] A.B. Finkelstein. The initial value problem for transient water waves. Comm Pure Appl Math. 1957;10;511-22.

[88] F.T. Korsmeyer, H.B. Bingham, J.N. Newman. TiMIT – a panel method for transient wave-body interactions. Research Laboratory of Electronics. MIT. 1999.

[89] M. Abramowitz and I. Stegun. Handbook of mathematical functions with formulas, graphs, and mathematical tables. U.S. Government Printing Office. Dover. New York. 1964.

[90] C.H. Lee and J.N. Newman. Computation of wave effects using the panel method. In numerical modeling in fluid-structure interactin, ed. S. Chakrabarti. WIT press. 2004.

[91] K. Yoon, and P.S. Lee. Nonlinear performance of continuum mechanics based beam elements focusing on large twisting behaviors. Comput Methods Appl Mech Engrg 2014;281;106-30.

[92] Meylan, M.H. and Sturova, I.V. Time-dependent motion of a two-dimensional floating elastic plate. J Fluid Struct. 2009:25:445-60.

[93] F.O. Henkel, D. Klein. Variants of the load case airplane crash. Transactions SMiRT 19 Toronto. 2007; J03/2.